

Influence of vacancies introduced by RTA on the nucleation, size, morphology, and gettering efficiency of oxygen precipitates in silicon wafers

Von der Fakultät für Mathematik, Naturwissenschaften und Informatik
der Brandenburgischen Technischen Universität Cottbus

zur Erlangung des akademischen Grades

Doktor der Naturwissenschaften
(Dr. rer. nat.)

genehmigte Dissertation

vorgelegt von

Master of Science Engineer

Dawid Kot

geboren am 25. Oktober 1982 in Legnica (Polen)

Gutachter: apl. Prof. Dr. sc. nat. Martin Kittler

Gutachter: Prof. Dr. rer. nat. habil. Jürgen Reif

Gutachter: Dr. Wilfried von Ammon

Tag der mündlichen Prüfung: 21. Juni 2013

Acknowledgements

I am very grateful to Dr. Gudrun Kissinger and Prof. Dr. Martin Kittler for giving me the possibility to work at IHP GmbH and conduct my PhD studies there. My special thanks are extended to Dr. Gudrun Kissinger for supervising me during my work. Thanks for taking the time to teach me what you know about defects in silicon crystals, for professional advice, discussion, your patience, and overall friendliness.

I would like to acknowledge Siltronic AG for financial support and the staff working there. Thanks to Dr. Andreas Sattler, Dr. Timo Müller, and Dr. Wilfried von Ammon acting as advisors to me.

I wish to acknowledge the help provided by Dr. Ioan Costina in ToF-SIMS investigations and by Dr. Andreas Schubert in STEM investigations. Many thanks to Dr. Jaroslaw Dabrowski for ab-initio calculations, and Monika Huber for FTIR measurements as well as to Michael Boy for the RTA pre-treatments, and Angelika Maasch for experimental assistance.

I would like to thank my colleagues from the departments of Joint Lab and Material Research especially Dr. Grzegorz Kozłowski, Lidia Tarnawska, Dr. Grzegorz Lupina, Malgorzata Sowinska, Dr. Adam Szyszka, and Canan Baristiran Kaynak for the kind atmosphere and support.

Finally I would give my special thanks to my family, relatives, and my beloved fiancée Justyna Mazur for their love and support during my studies.

Abstract

Internal gettering based on oxygen precipitates is a technique which is used to remove occasional metal contaminations from the active region of microelectronic devices. In order to obtain efficient internal gettering, the precipitation of oxygen in silicon must be precisely controlled. This can be done by rapid thermal annealing (RTA). RTA offers the possibility to establish well defined vacancy concentrations in silicon wafers. Since vacancies are well known to enhance the precipitation of oxygen in Czochralski silicon, RTA pre-treatments can be used to control the generation of oxygen precipitates.

This work provides information about the influence of vacancies, introduced by RTA, in silicon wafers on the nucleation of oxygen precipitates during a subsequent annealing in the temperature range between 400 °C and 1000 °C. Moreover, detailed investigations show morphologies and sizes of oxygen precipitates observed in vacancy supersaturated samples subjected to an annealing in the temperature range between 700 °C and 1000 °C for different annealing times. The morphology of the oxygen precipitates was investigated by scanning transmission electron microscopy (STEM) and Fourier transform infrared (FTIR) spectroscopy. In case of FTIR spectroscopy, the absorption bands were assigned to morphologies of the oxygen precipitates observed by STEM.

The final part of investigations presented in this work is dedicated to the gettering efficiency of metal impurities. Special focus is devoted towards the gettering efficiency of Cu in vacancy supersaturated samples. In order to understand the gettering of Cu in samples contaminated with high and low concentrations of Cu, two getter tests were carried out. A haze getter test was used to investigate the getter efficiency of Cu in highly contaminated samples. In this particular case, the concentration of Cu equals the concentration of Cu at its solubility limit at 900 °C. A “7 day storage getter test”, developed in this work, was used for the investigation of the getter efficiency of Cu in samples contaminated with low concentration of Cu amounting to $1 \times 10^{13} \text{ cm}^{-2}$.

It was found that the density of oxygen precipitates increases with increasing concentration of vacancies. The nucleation curves of oxygen precipitates in the vacancy supersaturated samples consist of three maxima wherein the maximum observed at 800 °C can be found only in the vacancy rich samples. These maxima can be explained

assuming the nucleation of coherent plate-like nuclei consisting of oxygen mono-layers ((O_i)₂-p1) and oxygen double-layers ((O_i)₂-p2) for the peaks at 450 °C and at 650 °C, respectively, and VO₂ mono layers for the peak at 800 °C.

The STEM investigations have shown the change of the morphology of oxygen precipitates in samples subjected to nucleation annealing at various temperatures. It was observed, that different temperatures of the RTA pre-treatment and thus different supersaturations of vacancies did not influence the morphology of oxygen precipitates in samples annealed at 800 °C. After annealing at a temperature of 800 °C three and two dimensional dendritic precipitates were found. This kind of precipitates gave rise to an absorption band at 1040 cm⁻¹ as shown by FTIR investigations.

From the results of the getter test it was deduced that secondary defects like dislocations have a strong influence on the getter efficiency in samples contaminated with high concentrations of Cu and Ni. In case of the samples contaminated with low concentration of Cu, gettering at dislocations is less important and oxygen precipitates become the main getter sink for Cu. It was also observed, that Cu aggregates at the edge of plate-like precipitates at the site of tensile strain of the silicon lattice. Moreover, the size and density of oxygen precipitates can strongly influence the getter efficiency of metal impurities.

The results and observations presented in this work can be very useful for designing and fabrication of high performance silicon wafers. The results can be used for the development of a gettering simulator based on oxygen precipitation. The results of the analysis of the FTIR spectra can be helpful for the fast characterization of the morphologies of oxygen precipitates by means of FTIR.

Zusammenfassung

Die interne Getterung basierend auf Sauerstoffpräzipitaten ist eine Technik, die verwendet wird, um gelegentliche Metallverunreinigungen aus dem aktiven Bereich der mikroelektronischen Bauelementen zu entfernen. Um eine effiziente interne Getterung zu erhalten, muss die Präzipitation von Sauerstoff in Silizium präzise gesteuert werden. Dies kann durch schnelle thermische Behandlung (RTA) erfolgen. RTA bietet die Möglichkeit, genau definierte Vakanzenkonzentrationen in Siliziumwafern einzubauen. Weil bekannt ist, dass die Vakanzen die Präzipitation von Sauerstoff in CZ Silizium fördern, kann durch eine RTA Vorbehandlung die Bildung von Sauerstoffpräzipitaten gesteuert werden.

Diese Arbeit liefert Informationen zum Einfluß von Vakanzen, deren Konzentration durch RTA eingestellt wurde, auf die Keimbildung von Sauerstoffpräzipitaten in Siliziumwafern während einer anschließenden Temperung im Temperaturbereich zwischen 400 °C und 1000 °C. Außerdem, zeigen detaillierte Untersuchungen die Morphologien und Größen der Sauerstoffpräzipitate in vakanzenübersättigten Proben, die einer Temperung im Temperaturbereich zwischen 700 °C und 1000 °C für unterschiedliche Zeiten ausgesetzt waren. Die Morphologie der Sauerstoffpräzipitate wurde mittels STEM und FTIR-Spektroskopie untersucht. Im Fall der FTIR-Spektroskopie wurden die Absorptionsbanden bestimmten Morphologien der Sauerstoffpräzipitate, beobachtet durch STEM, zugeordnet.

Der letzte Teil der Untersuchungen in dieser Arbeit bezieht sich auf die Gettereffizienz der Sauerstoffpräzipitate für metallische Verunreinigungen. Besondere Aufmerksamkeit ist der Gettereffizienz von Cu in vakanzenübersättigten Proben gewidmet. Um die Getterung von Cu in Proben mit hoher und niedriger Konzentration von Cu zu verstehen, wurden zwei verschiedene Gettertests durchgeführt. Der „Haze Getter Test“ wurde verwendet, um die Effizienz der Cu-Getterung in stark kontaminierten Proben zu untersuchen. In diesem speziellen Fall ist die Konzentration des Cu gleich der Löslichkeit von Cu bei bei 900 ° C. Ein „Gettertest mit 7 Tage Lagerung“, der in dieser Arbeit entwickelt wurde, wurde zur Untersuchung der Gettereffizienz in Proben mit niedriger Cu-Konzentration in Höhe von $1 \times 10^{13} \text{ cm}^{-2}$ verwendet.

Es wurde festgestellt, dass die Dichte der Sauerstoffpräzipitate mit der Erhöhung der Vakanzenkonzentration steigt. Die Keimbildungskurven der Sauerstoffpräzipitate in den vakanzenübersättigten Proben besitzen drei Maxima, wobei das Maximum bei 800 °C nur in vakanzenreichen Proben gefunden wurde. Diese Maxima können auf der Grundlage der Keimbildung von kohärenten, plättchenförmigen Keimen, bestehend aus Sauerstoff-mono-Schichten ((O_i)_{2-p1}) und Sauerstoff-doppel-Schichten ((O_i)_{2-p2}) für die Peaks bei 450 °C und bei 650 °C und mit VO₂-mono-Schichten für den Peak bei 800 °C erklärt werden.

STEM Untersuchungen haben die Veränderung der Morphologie der Sauerstoffpräzipitate in Proben, die einer Keimbildungstemperatur bei verschiedenen Temperaturen unterzogen wurden, gezeigt. Es wurde beobachtet, dass unterschiedliche Temperaturen der RTA-Vorbehandlung und somit unterschiedliche Übersättigungen von Vakanzen keinen Einfluss auf die Morphologie der Sauerstoffpräzipitate in den Proben, die bei 800 °C getempert wurden, hatten. Nach Temperungen bei einer Temperatur von 800 °C wurden drei- und zweidimensionale dendritische Präzipitate gefunden. Diese Art der Präzipitate gab Anlass zu einer Absorptionsbande bei 1040 cm⁻¹, was durch FTIR-Untersuchungen gezeigt wurde.

Aus den Ergebnissen der Getter-Test wurde geschlossen, dass sekundäre Defekte, wie Versetzungen, einen großen Einfluss auf die Gettereffizienz in Proben mit hoher Konzentration von Cu und Ni Verunreinigungen haben. In Proben mit niedriger Konzentration von Cu ist die Getterung an Versetzungen weniger wichtig und die Sauerstoffpräzipitate werden die Hauptgettersenke für Cu. Die Aggregation von Cu wurde an der Kante von plättchenförmigen Präzipitaten gefunden, wo das Siliciumgitter unter Zugspannung steht. Außerdem kann die Größe und Dichte der Sauerstoffpräzipitate starken Einfluss auf die Gettereffizienz von Metallverunreinigungen haben.

Die Ergebnisse und die Beobachtungen, die in dieser Arbeit vorgestellt werden, können sehr nützlich für die Entwicklung und Herstellung von hochwertigen Siliziumwafern sein. Die Ergebnisse können auch für die Entwicklung von Gettersimulatoren für Sauerstoffpräzipitate verwendet werden. Die Ergebnisse der Analyse von FTIR Spektren können hilfreich sein für die schnelle Charakterisierung der Morphologien von Sauerstoffpräzipitaten mittels FTIR.

List of Symbols

b	Burgers vector
C_0	constant regarding to solubility of oxygen in silicon at equilibrium temperature
C_I	concentration of silicon self-interstitials
$C_{O_{2i}}$	concentration of oxygen dimers
C_I^{eq}	equilibrium concentration of silicon self-interstitials
C_{O_i}	concentration of interstitial oxygen
$C_{O_i}^{eq}$	solubility of oxygen in silicon at equilibrium temperature
C_p	concentration of oxygen in the precipitate
Cu_{In}	concentration of Cu measured on the surface of the sample after 7 day storage at room temperature
Cu_{Ref}	concentration of Cu on the surface of the sample after the contamination
C_V	concentration of vacancies
C_V^{eq}	equilibrium concentration of vacancies
D_0	oxygen diffusivity
D_{0M}	pre-factor regarding to diffusion coefficients of metals in silicon
d	atomic distance in silicon
$D_{Cu_{eff}}$	effective diffusivity of Cu in silicon
D_{eff}	effective diffusivity of oxygen
D_I	diffusion coefficient of silicon self-interstitials
D_M	diffusion coefficients of metals in silicon
$D_{O_{2i}}$	diffusivity of oxygen dimer
D_{O_i}	diffusion coefficient of oxygen
d_{Pl}	thickness of plate-like precipitates
D_V	diffusion coefficient of vacancies
d_w	thickness of the wafer
E_A	activation energy
E_D	activation energy of the diffusion process of oxygen in silicon
E_S	dissolution enthalpy of oxygen in silicon

G	temperature gradient at the growth interface of the crystal
ΔG_{Total}	total free energy of formation of a nucleus
ΔG_{ϵ}	elastic strain energy
ΔG_v	free energy of formation
ΔG_{σ}	free energy necessary to create the new interface (surface energy)
H_M	migration enthalpy of metals
H_S	solution enthalpy of the metal atoms in silicon with respect to the metal atoms in the silicide phase
I	silicon self-interstitial atom
J	stationary, time independent nucleation rate
K	equilibrium constant of the reaction
k_B	Boltzmann constant
k_{IV}	reaction constant of the Frenkel-pair mechanism
K_P	bulk modulus of SiO_x
l_{Oct}	edge length of octahedral precipitates
L_D	length of the dendritic precipitates
L_{Pl}	length of plate-like precipitates
N_0	density of nucleation sites
N_{BMD}	density of bulk micro defects
n	number of oxygen atoms formed in the process of agglomeration
N	density of oxygen precipitates
N_a	boron doping
N_{crit}	equilibrium concentration of oxide precipitate nuclei of critical size in silicon
N_{inv}	number of etch pits on the investigated sample
N_{Ref}	number of etch pits on the referential sample
N_{Si}	Si atomic volume per metal atom
O_{2i}	oxygen dimer
O_i	oxygen interstitial atom
P_n	nucleus containing n oxygen atoms
r	radius of oxygen precipitate

r_{crit}	critical radius of the nuclei
r_F	final radius
r_m	radius of the unconstrained cavity created by missing Si atoms in the matrix
r_p	radius of the growing unstrained precipitate
S_{BMD}	normalized inner surface
S_{crit}	threshold value of the normalized inner surface
S_M	solubility of meals in silicon
S_p	surface of the precipitate
S_s	solution entropy
t	time of annealing
T	absolute temperature
V	vacancy
V	pull rate
V_m	initial unconstrained volume of the matrix
Z	Zeldovich factor
x	stoichiometric factor of SiO_x
α	absorption coefficient
β	stoichiometric factor attributed to the number of ejected silicon self-interstitials
β_{pl}	aspect ratio between l_{pl} and L_{pl}
γ	stoichiometric factor attributed to the number of consumed vacancies
δ	linear misfit between SiO_x and the Si lattice
ε	strain in the precipitate
η_{7day}	getter efficiency determined by 7 day storage test
η_{Haze}	getter efficiency determined by Haze getter test
μ	shear modulus of silicon
ν	Poisson's factor
σ_M	capture cross-sections
σ	surface energy
χ	calibration factor
ω	frequency of the attachment of interstitial oxygen atoms to the nucleus
Ω	molecular volume per oxygen atom

List of Abbreviations

(O _i) ₂ -p1	oxygen mono-layers
(O _i) ₂ -p2	oxygen double-layers
2D	two dimensional
2DLFM	two-dimensional symmetry low-frequency mode
3D	three dimensional
BF	bright field,
BMD	bulk micro defect density
CG	chemical gettering
COPs	crystal originated precipitates
CPAA	charged particle activation analysis
CZ	Czochralski method
DF	dark field
DLTS	deep level transient spectroscopy
DZ	defect denuded zone
EBIC	electron beam induced current
EDX	energy-dispersive X-ray spectroscopy
EG	external gettering
EMT	effective-medium theory
FTIR	Fourier transform infrared spectroscopy
FZ	Float-Zone method
GF-AAS	graphite furnace atomic absorption spectrometry
HAADF	high angle annular dark field
IC	integrated circuits
ICP-MS	inductively coupled plasma mass spectrometry
IG	internal gettering
IR	infrared
IR-LST	infrared laser-scanning tomography
ITRS	international technology roadmap for semiconductors
LO	longitudinal mode
MCTS	minority carrier transient spectroscopy
OP	oxygen precipitates
OSFs	oxidation induced stacking faults
PG	proximity gettering

RSF	relative sensitivity factor
RT	room temperature
RTA	rapid thermal annealing
SIMS	secondary-ion-mass spectrometry
SPR	spreading resistance probe infrared
STEM	scanning transmission electron microscope
TEM	transmission electron microscopy
TO	transverse mode
ToF-SIMS	time of flight secondary ions mass spectroscopy
XRD	X-ray diffraction

Contents

1. Introduction.....	1
2. Oxygen in silicon.....	3
2.1. Czochralski silicon crystal growth.....	3
2.2. Interstitial oxygen in silicon.....	6
2.3. Nucleation of oxygen precipitates.....	15
2.4. Adjustment of vacancy concentration by RTA pre-treatments.....	26
2.5. Growth of oxygen precipitates.....	29
2.6. Morphology of oxygen precipitates.....	31
2.7. Detection of oxygen precipitates.....	33
3. Gettering of metal impurities.....	35
3.1. Metal impurities in silicon.....	35
3.2. Gettering techniques.....	40
3.3. Gettering mechanisms and gettering sinks.....	42
4. Experimental methods and techniques.....	46
4.1. Preferential etching.....	46
4.2. STEM.....	48
4.3. FTIR.....	49
4.4. Haze getter test.....	51
4.5. ToF-SIMS.....	52
5. Aim of this study.....	53
6. Results and discussion.....	54
6.1. Nucleation of oxygen precipitates in RTA pre-treated wafers.....	55
6.2. Influence of vacancies on the morphology and size of oxygen precipitates investigated by STEM.....	71
6.3. FTIR.....	94
6.4. Haze getter test.....	105
6.5. ToF-SIMS getter test.....	114
7. Summary and conclusions.....	126
8. Scientific visibility.....	129
8.1. Publications list.....	129
8.2. Own presentations at conferences.....	130
Bibliography.....	132

1. Introduction

Silicon is the most important semiconductor used in the semiconductor industry. Due to its properties and its relatively low price, silicon is commonly used as a substrate for the production of integrated circuits (IC). Each IC contains numerous active devices such as transistors or diodes and passive devices as e.g. capacitors and resistors. At the present, for most modern technology, the amount of transistors per chip exceeds $10^8/\text{cm}^2$. As the scaling in the microelectronic industry continues, the control of smaller defects and lower impurity levels become important for the device yield.

Until now, two production methods of silicon single crystals are dominant the Czochralski (CZ) method and the Float-Zone (FZ) method. Growth of FZ crystals is more difficult to control. Until now the diameter of FZ silicon is limited to 200 mm. The diameter of the wafers obtained by the CZ method has reached already 300 mm and will be increased in the near future to 450 mm. The main difference between the CZ and the FZ material resulting directly from the single-crystal growth method is the purity. In the CZ method, the molten silicon remains in contact with the quartz crucible what results in a high concentration of oxygen impurities of up to 10^{18} cm^{-3} . In the FZ technique, the molten silicon has no contact with a crucible but is situated in a gas ambient. Therefore, the concentration of oxygen impurities in the FZ material does not exceed 10^{16} cm^{-3} . From the economic point of view, the CZ wafers, on which more chips per wafer can be manufactured, are more efficient than the FZ wafers. The presence of oxygen atoms in CZ wafers is rather an advantage than a disadvantage because the oxygen precipitates can act as getter centers for metal impurities which can be introduced in the device manufacturing process. Oxygen precipitates also improve the mechanical strength of silicon wafers what is a benefit in terms of their ability to withstand thermal stress and suppress slipping, wafer bowing and warping during high-temperature processing [Lin94]. However, the precipitation of oxygen precipitates must be kept under control otherwise it can become harmful for the wafer and the devices.

Oxygen precipitation in silicon was investigated since decades but still there are lots of issues which should be investigated. According to the international technology roadmap for semiconductors (ITRS), the defect engineering of CZ wafers will be improved at least for the next 15 years. Annealed wafers are one of the development branches which are a point of interest [ITR11].

The so-called magic denuded zone process offers the possibility to establish well defined vacancy concentrations in silicon wafers by rapid thermal annealing (RTA) treatment [Fal97]. The vacancy profile within the silicon wafer can be controlled by the soak temperature, the cooling rate and the gas ambient [Pag97, Kis00, Aka02, Fu07]. As vacancies are well known to enhance the precipitation of oxygen in CZ silicon, RTA pre-treatment can be used to control the generation of oxygen precipitates [Fal97, Kis07].

This work is focused on CZ material and particular attention is given to the influence of vacancy supersaturation on the precipitation of oxygen in silicon, as well as on the features of the oxygen precipitates like size, density, morphology, and getter efficiency.

In the first chapter, the basic issues related to oxygen in silicon like the measurement techniques for the concentration of interstitial oxygen, the nucleation and growth of oxygen precipitates and the gettering of metal impurities by oxygen precipitates are introduced. This is followed by the results and their discussion.

2. Oxygen in silicon

2.1. Czochralski silicon crystal growth

The method named after the Polish chemist Jan Czochralski who discovered this method in 1916 is commonly used for the production of silicon crystals. The principle of the method is illustrated in Fig. 1. First, polycrystalline silicon is molten in a silica crucible, above which a singlecrystal seed is placed. Then, the seed is dipped in the molten silicon. This step is called seeding. The seed crystal rotates and is slowly pulled up whereas the liquid silicon crystallizes around the seed. First a small neck is grown in order to prevent the expansion of dislocation from the seed into the crystal. The process runs under an argon or helium flow and is heated by resistance heaters or radio frequency heating coils. In reality, not only the seed rotates but also the melt what improves the homogenization of the temperature and the mixing of the melt. Moreover, the melt rotation can stabilize the heat and the mass fluxes. Additionally, the growth process can be improved by mechanical vibration, electric current or magnetic fields [Rud09]. The contact of the molten silicon with the silica crucible causes oxygen to transfer from the crucible to the silicon melt. Although most of the oxygen evaporates from the melt as SiO gas, a high concentration of oxygen remains in the crystal. Properly applied magnetic fields during crystal pulling provide a conduction force in the melt resulting in a more uniform distribution of oxygen in the silicon single crystal.

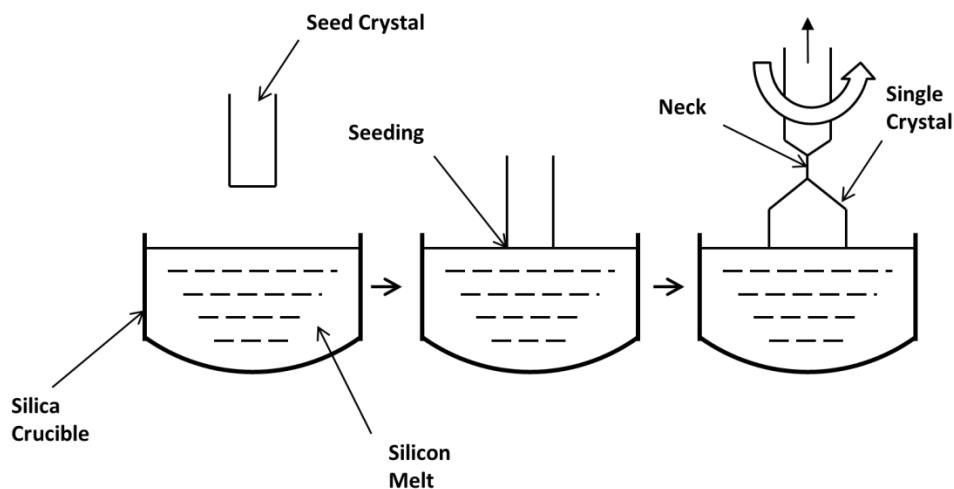


Figure 1: Principle of single crystal growth by the Czochralski method [Shi89].

As it is shown in Ref. [Shi01], the growth of 400 mm silicon crystals with high quality and without striations of impurities is possible by applying superconductive magnets generating field strengths above 0.35 T.

In spite of high quality, silicon crystals are not free of grow-in defects. Besides nuclei of oxygen precipitates, vacancy aggregates and Si self-interstitial related defects can be found. The size and defect distribution in silicon crystal is strongly influenced by pull rate. At high pull rate vacancies are supersaturated and vacancy agglomerates are formed as shown in Fig. 2. Slowing down the pull rate, vacancy supersaturation decreases. At critical point the supersaturation of vacancies is too low for the nucleation and growth of vacancy agglomerates. However, the supersaturation of vacancies in this point is enough high to facilitate the precipitation of oxygen during crystal cooling. After subsequent oxidation of this region, large grown-in oxide precipitates nuclei are prone to develop defects which are referred as oxidation induced stacking faults (OSFs). At low pull rate self-interstitials are supersaturated and self-interstitial related defects like L-pits are formed.

The defect distribution in silicon crystal can be controlled by the ratio between pull rate V and the temperature gradient at the growth interface of the crystal G . As it was found the boundary between the regions of vacancy and self-interstitial supersaturations is at $V/G = C_{crit} = 1.34 \times 10^{-3} \text{ cm}^2/\text{K min}$ [Vor82, Vor98, Von99]. For $V/G > C_{crit}$, the formation of vacancy type defects is dominant and for $V/G < C_{crit}$ self-interstitial related defects are developed. For V/G slightly higher than C_{crit} the OSFs develop.

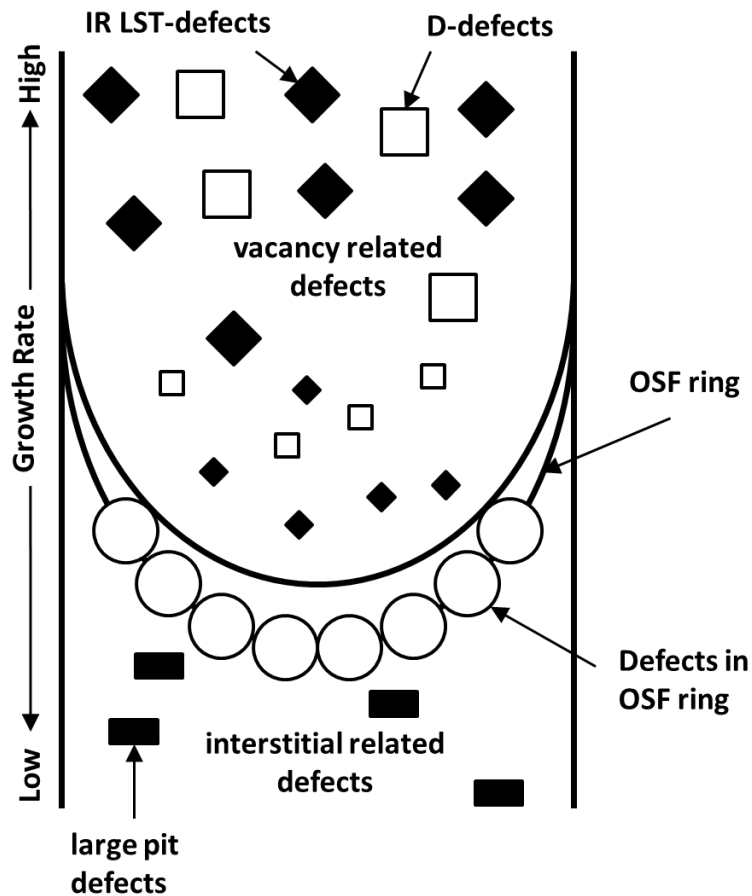


Figure 2: Distribution of defects in CZ silicon as a function of the pull rate [Von99].

Besides of the presence of the unavoidable oxygen impurities, the silicon crystal also contains intentional dopants like phosphor or boron atoms which determine the type of the semiconductor like n-type or p-type, respectively. The doping of crystal determines not only the electric properties of the wafer, it also impacts the oxygen precipitation and the getter efficiency of metal impurities [Sha96, Web02].

TABLE 1. Infrared absorption bands of interstitial oxygen and its isotopes in silicon [Hal99]

Attribution	Position (cm ⁻¹)			
	Low temperature ($\leq 40\text{K}$)		Room temperature	
	²⁸ Si ₂ ¹⁶ O	²⁸ Si ₂ ¹⁸ O	²⁸ Si ₂ ¹⁶ O	²⁸ Si ₂ ¹⁸ O
(2DLFM)	29.3	27.2		
	37.8	35.3		
	43.3			
	49			
	517.3	517.3		
(E _u)			513.5	
	596.3	596.3	560	513.9
A _{1g} (IR inactive)	648.2	645.1		560
(A _{1g} +2DLFM)	1136	1084.4	1106	
(A _{2u} or ν_3)	1127	1076.7		1058
	1122	1071		
(A _{2u} or 2DLFM)	1203	1150.8	1226.7	
	1216	1162.4		1172.6
	1748.6	1696	1720.1	
(A _{2u} + A _{1g})	1741.4	1689.3		1670
	1736	1683		

The bands in Table 1 are attributed to the normal modes and their transitions of the Si-O-Si system. In the literature, the Si-O-Si molecule is considered as a molecule with symmetry C_{2v} or D_{3d} (for Si₂O in stretched form) as shown in Figs. 4 (a) and (b), respectively [Yam90, Wag91]. According to Hrostowski and Kaiser, oxygen has three main frequencies ν_1 , ν_2 and ν_3 , which are attributed to symmetric stretching, symmetric and antisymmetric bending, respectively [Hro57]. In the assumption of D_{3d} symmetry, the frequencies of the Si-O_i-Si molecule are considered as an interaction between two systems. The first system is related to the high-energy modes of the Si-O_i-Si molecule with D_{3d} symmetry and the second one is the two-dimensional symmetry low-frequency mode (2DLFM). Simply speaking, 2DLFM corresponds to the radial motion and axial rotation of the O atom around the z axis. In this model, the A_{1g} frequency is IR inactive but the combination of A_{1g} and 2DLFM is already active.

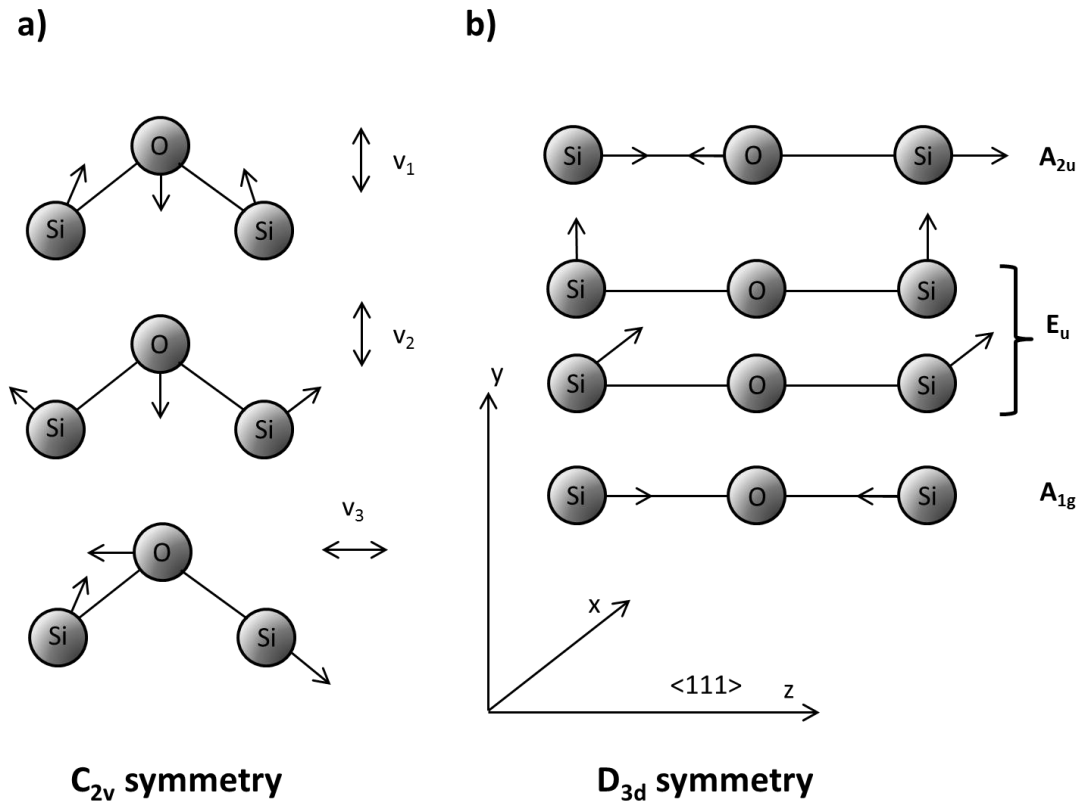


Figure 4: Vibration of the Si-O-Si molecule for the C_{2v} symmetry model (a) and the D_{3d} symmetry (b) [Hro57, Yam90].

2.2.2. Measurement of the interstitial oxygen concentration in silicon

The accurate determination of the oxygen concentration in silicon wafers is important for the investigation of the behavior of oxygen atoms in silicon, its diffusion, solubility, precipitation or the impact on the electrical and mechanical properties of silicon wafers. In order to compare the results of theoretical modeling with experimental results, the knowledge about the oxygen content in silicon is also required. Oxygen appears in the silicon matrix in the interstitial form and as precipitates. Therefore, the problem arises how to distinguish between interstitial oxygen and precipitated oxygen. Many techniques measure the total concentration of oxygen in silicon but infrared absorption is a technique which can distinguish between oxygen in precipitates and interstitial oxygen. For this reason, the infrared (IR) absorption became the most common and most convenient method for the measurement of the concentration of interstitial oxygen in silicon. All measurements of the oxygen concentrations presented in this work were carried out by this method.

The principle of this method is based on Beer's law, which says that the absorption caused by an impurity is proportional to its concentration. In order to determine the concentration of interstitial oxygen in silicon, one has to multiply the absorption coefficient of oxygen determined from the interstitial band by calibration factor according to Eq. (1),

$$C_{O_i} = \chi \cdot \alpha \quad (1)$$

where C_{O_i} is the concentration of interstitial oxygen, χ is the calibration factor and α is the absorption coefficient at the peak position. The absorption coefficient is derived from the absorption spectrum.

The most popular equipment used to obtain absorption spectra is the Fourier-transform infrared (FTIR) spectrometer. The measurement of interstitial oxygen is carried out at room temperature and the absorption coefficient of the absorption band at 1106 cm^{-1} is used for the determination of the concentration of interstitial oxygen. Depending on the standard used one can find different calibration factors. In this work the DIN standard (DIN 50438/1) was used which is the same as the new ASTM F121-83 standard. According to DIN and new ASTM the calibration factor is $\chi = 2.45 \times 10^{17} \text{ cm}^{-2}$. In case of the old ASTM F121-79 and JEIDA standards the calibration factors are $\chi = 4.81 \times 10^{17} \text{ cm}^{-2}$ and $\chi = 3.03 \times 10^{17} \text{ cm}^{-2}$, respectively. Despite of many advantages, the IR method also has limitations. The room temperature measurements are only suitable for the determination of oxygen concentrations in the range of 8×10^{15} to $3 \times 10^{18} \text{ cm}^{-3}$ which covers the usual oxygen concentrations of CZ silicon [Shk92]. In case of the samples containing oxygen precipitates, problems can be caused by the close neighborhood of the band of interstitial oxygen and the bands of oxygen precipitates which are located at 1095 cm^{-1} and at 1225 cm^{-1} [Sas99, Bor00].

2.2.3. Solubility

The solubility defines how much of solute can be dissolved in a solvent under specific conditions. In case of silicon and oxygen, silicon acts as a solvent while oxygen is the solute. The temperature dependence of the solubility of oxygen in silicon expresses Eq. (2),

$$C_{O_i}^{eq}(T) = C_0 \cdot \exp\left(-\frac{E_S}{k_B \cdot T}\right) \quad (2)$$

where C_0 is a constant, E_S is the dissolution enthalpy, k_B is Boltzmann's constant and T is the absolute temperature. Many techniques like secondary-ion-mass spectrometry (SIMS), spreading resistance probe (SPR), infrared spectroscopy (IR), charged particle activation analysis (CPAA), or X-ray diffraction (XRD) were used to determine the oxygen solubility in silicon. Some values of C_0 and E_S available in the literature are included in Table 2. One can also find the method by which these values were obtained and the temperature range for which the solubility was determined in Table 2. The most frequently referred values of the oxygen solubility are the values obtained by Mikkelsen [Mik86]. Fig. 5 shows the curve of the oxygen solubility obtained from the data of Mikkelsen.

TABLE 2. Literature data for the constant C_0 and dissolution enthalpy E_S collected by Borghesi [Bor95].

C_0 (10^{22} atom/cm ³)	E_S (eV)	Method	Temperature (°C)	Ref.
0.14	2.53	SIMS, out-diffusion	700-1160	[Lee85]
0.13	2.50	SIMS, implanted O	700-1100	[Lee86]
1100	2.3 ± 0.3	SPR	1250-1400	[Log59]
6.3	2.3 ± 0.17	IR	1100-1200	[Bea71]
9	1.52	SIMS, CPAA, IR	800-1400	[Mik86]
3.2	1.4	IR	850-1050	[Liv86]
9.3	1.2 ± 0.13	CPAA (¹⁶ O)	1000-1375	[Ito86]
0.27	1.10	XRD	1100-1200	[Tak73]
	1.08 ± 0.02	CPAA (¹⁶ O)	1000-1280	[Gas80]
0.10	1.03	IR	950-1350	[Cra81]
0.13	0.95 ± 0.1	IR	1000-1250	[Hro59]
0.055	0.89	IR	460-900	[Wij91]

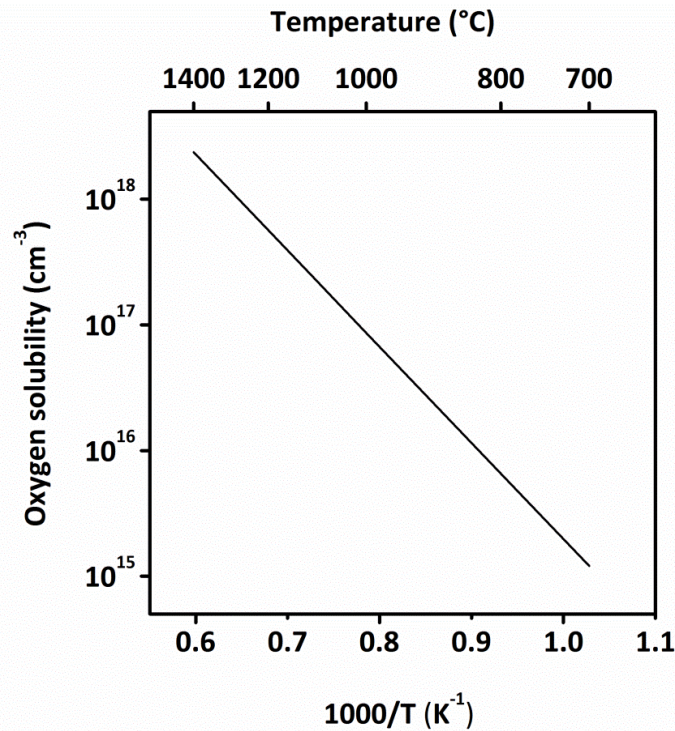


Figure 5: Oxygen solubility in silicon plotted according to the data of Mikkelsen [Mik86].

Typical concentrations of interstitial oxygen in CZ silicon wafers can be in the range of about $3 \times 10^{17} \text{ cm}^{-3}$ to $1 \times 10^{18} \text{ cm}^{-3}$. This means that oxygen remains supersaturated for common temperatures of device processing as can be deduced from Fig. 5.

2.2.4. Diffusivity

Diffusion is a process of concentration alignment of the solution created by two compounds, which do not react chemically with each other. During diffusion, the compounds are moving from the place where the concentration is higher to the place where the concentration is lower. The parameter characterizing the diffusivity is the diffusion coefficient expressed in cm^2/s . It is the amount of a component diffusing through the unitary area in the time unit at the unitary gradient of concentration causing diffusion [Tom99]. The temperature dependence of the diffusion coefficient expresses Eq. (3),

$$D_{oi}(T) = D_0 \cdot \exp\left(-\frac{E_D}{k_B \cdot T}\right), \quad (3)$$

where D_0 is diffusivity and E_D is activation energy of the diffusion process. In order to obtain the diffusion coefficients of oxygen in silicon, the same investigation techniques as for the determination of the oxygen solubility in silicon were used. The diffusion coefficients, the techniques of determination, and the temperature range of determination achieved by different authors are included in Table 3.

TABLE 3. Oxygen diffusivity D_0 and activation energy collected by Borghesi [Bor95].

D_0 (cm ² /s)	E_D (eV)	Method	Temperature (°C)	Ref.
22.6	3.15	CPAA(¹⁸ O)	1100-1280	[Gas80]
3.2	2.6	CPAA(¹⁶ O)	1150-1375	[Ito85]
0.23	2.56	stress-induced dichroism	1100-1280	[Cor64], [Wat85]
0.17	2.54	stress-induced dichroism	330-1240	[Sta83]
0.14	2.53	SIMS, O out-diff.	700-1160	[Lee86]
0.13	2.53	SIMS, CPAA, IR	330-1280	[Mik86]
0.11	2.51	IR, SANS	650-1050	[Liv84]
0.11	2.51	stress-induced dichroism	330-1200	[New90]
0.07	2.44	SIMS, O in-diff.	700-1240	[Mik82]
0.091	2.4	Lattice parameter XRD	1100-1280	[Tak73]

The diffusion of oxygen in silicon proceeds by the jump of an oxygen atom from one interstitial site to another. This diffusion is assumed to be true for temperatures above 800 °C [New94, New00]. However, for temperatures lower than 800 °C it was observed that the diffusion of oxygen can be enhanced [New83, New85]. This means that the effective diffusivity of oxygen is higher than that of interstitial oxygen. The species causing the enhancement of the diffusivity was suspected to be the oxygen dimer (O_{2i}), the oxygen dimer silicon interstitial $O_{2i}I$ or the oxygen dimer vacancy $O_{2i}V$ complex having an activation energy of 1.7 eV [Gös82, Bin96, Ram98, Cla87]. Moreover, the enhanced diffusion of oxygen was assumed to be caused by the

interaction of interstitial oxygen O_i with metallic impurities, carbon, or hydrogen [New00]. At present, the oxygen dimer is the mostly accepted species causing the enhanced diffusion.

In this work, for the calculation of radius of oxygen precipitates at temperatures higher than 700 °C, the oxygen diffusivity of Mikkelsen was used. Here, the activation energy and diffusivity are 2.53 eV and 0.13 cm²/s, respectively [Mik86]. In order to simulate nucleation peaks in nucleation curves at temperatures below 700 °C, the effective diffusivity of Takeno et al [Tak98] was used. The diffusion coefficient derived from the data of Mikkelsen and the enhanced diffusivities from Refs. [Tak98, Lee88] are shown in Fig. 6.

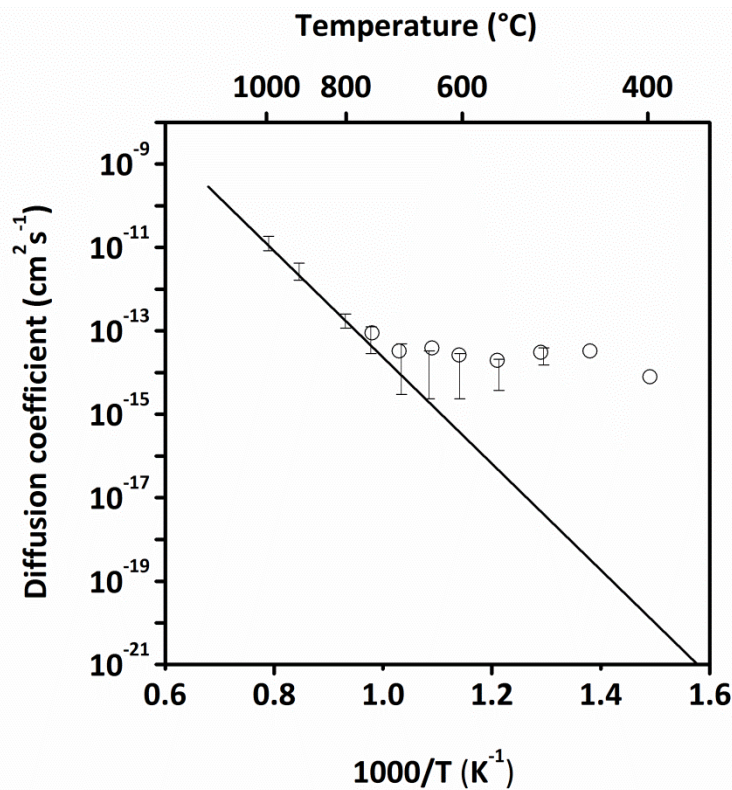


Figure 6: Oxygen diffusivity in silicon: the solid line represents the best fit according to Mikkelsen [Mik86], data of Takeno et al. (empty circles) [Tak98], and Lee et al. (bars) [Lee88].

The effective diffusivity at temperatures below 750 °C was determined from out diffusion, the precipitate growth, and dislocation unlocking experiments [Lee88, Tak98, Sen01]. If, the oxygen dimer would be the main contributor to the diffusion of oxygen in silicon, the reaction of the formation of the oxygen dimer can be written as follows $O_i + O_i \leftrightarrow O_{2i}$. Then the effective diffusivity can be expressed by the equation

$$D_{eff}(T) = \frac{D_{O_i} \cdot C_{O_i} + 2D_{O_{2i}} \cdot C_{O_{2i}}}{C_{O_i} + 2C_{O_{2i}}} \quad (4)$$

with

$$C_{O_{2i}} = C_{O_i}^2 \cdot K \quad (5)$$

where $D_{O_{2i}}$ is the diffusivity of oxygen dimer, $C_{O_{2i}}$ is the concentration of oxygen dimers, and K is the equilibrium constant of the reaction [Tak98].

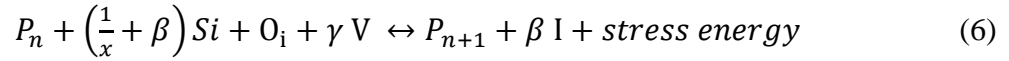
2.3. Nucleation of oxygen precipitates

2.3.1. Homogenous nucleation

The nucleation of oxygen precipitates in silicon is a stage in the process of phase transition leading to formation of silicon oxide SiO_x with stoichiometric factor $x = 1-2$. During the nucleation small nuclei of the new phase are formed. Depending on the conditions of the thermal treatments and thermal history of silicon crystal, the nuclei can grow increasing their size, if the critical radius was reached, or can be dissolved. An important parameter for the oxygen precipitation and the major force of the oxygen precipitation is the degree of supersaturation. It is the ratio between the concentrations of interstitial oxygen C_{O_i} and its solubility $C_{O_i}^{eq}$, which is a temperature dependent parameter. This parameter contributes to the volume free energy of formation driving the nucleation. If the degree of supersaturation is larger than 1, the volume free energy is higher and the driving force of nucleation and precipitation is larger. Because the oxygen is supersaturated in the silicon solute in a broad range of temperatures, the nucleation and precipitation during thermal treatment will easily occur. However, both the creation of a new interface and the strain induced by the precipitate in the host matrix compensate the effect of the supersaturation.

The nucleation of oxygen precipitates in silicon can occur homogeneously or heterogeneously. In case of homogeneous nucleation, the nuclei are formed randomly due to fluctuation in the density of oxygen. In case of heterogeneous nucleation, lattice defects or impurities serve as nucleation sites for oxygen precipitates reducing the energy needed to create a new interface. In order to understand the nucleation process in the most convenient way, one has to consider the Gibbs free energy of a silicon crystal containing atoms of interstitial oxygen O_i , silicon self-interstitials I , vacancies V , and oxygen precipitates. Minimizing this energy, one can calculate the critical radius of the precipitate. The considerations of the free energy of formation of homogeneous and heterogeneous nuclei, and the calculation of the critical radius are briefly described below.

The precipitation of oxygen atoms in a silicon crystal can be expressed by the dynamic equilibrium reaction



where P_n is the nucleus containing n oxygen atoms formed in the process of agglomeration of oxygen interstitial atoms O_i associated with ejection of silicon self-interstitials I and consumption of vacancies V in order to reduce stress, γ and β are stoichiometric factors attributed to the number of consumed vacancies or ejected silicon self-interstitials, respectively. The precipitate nuclei can grow by attaching oxygen atoms or can be dissolved depending on the annealing condition. The parameter deciding if the nuclei will grow or will be dissolved is the critical radius which can be calculated considering the total free energy of formation of a nucleus ΔG_{Total} consisting of n oxygen atoms. The total free energy of formation of homogeneous nuclei contains three major contributions as shows Eq. (7) [Tan94].

$$\Delta G_{Total} = -\Delta G_v + \Delta G_\sigma + \Delta G_\epsilon \quad (7)$$

where ΔG_v is the free energy of formation, ΔG_σ is the free energy necessary to create the new interface and ΔG_ϵ is the elastic strain energy. The negative free energy of formation is the main driving force for precipitate nucleation and according to Ref. [Van96] is given by

$$\Delta G_v = n \cdot k_B \cdot T \cdot \ln \left[\left(\frac{C_{O_i}}{C_{O_i}^{eq}} \right) \left(\frac{C_V}{C_V^{eq}} \right)^\gamma \left(\frac{C_I}{C_I^{eq}} \right)^{-\beta} \right] \quad (8)$$

where n is the number of oxygen atoms, C_{O_i} , C_V and C_I , are the concentrations of oxygen interstitials, vacancies and silicon self-interstitials, respectively and $C_{O_i}^{eq}$, C_V^{eq} and C_I^{eq} are their equilibrium concentrations. As shown in Eq. (8), the value of the free energy of formation increases with increasing supersaturation of interstitial oxygen and vacancies. It decreases with increasing supersaturation of silicon interstitials.

The surface and strain energies in Eq. (7) act against the nucleation. The free energy necessary to create a new surface ΔG_σ can be written as

$$\Delta G_\sigma = S_p \sigma \quad (9)$$

where S_p is the surface of the precipitate and σ is the surface energy per unit area. Because σ cannot be measured directly, it is often used as a fitting parameter. The third contribution to the total free energy is the elastic strain energy. This energy results from the difference between the volumes of the oxygen precipitate SiO_x and Si and can be described as a volume variation of the precipitate in terms of the elastic properties of silicon [Hu86]. The molecular volume of the oxygen precipitates is about two times larger than the molecular volume of silicon, accordingly the radius r_p of the growing unstrained precipitate is larger than the radius r_m of the unconstrained cavity created by missing Si atoms in the matrix. In order to reach a common, final radius r_F the cavity must be expanded and the precipitates must be compressed as illustrates Fig. 7.

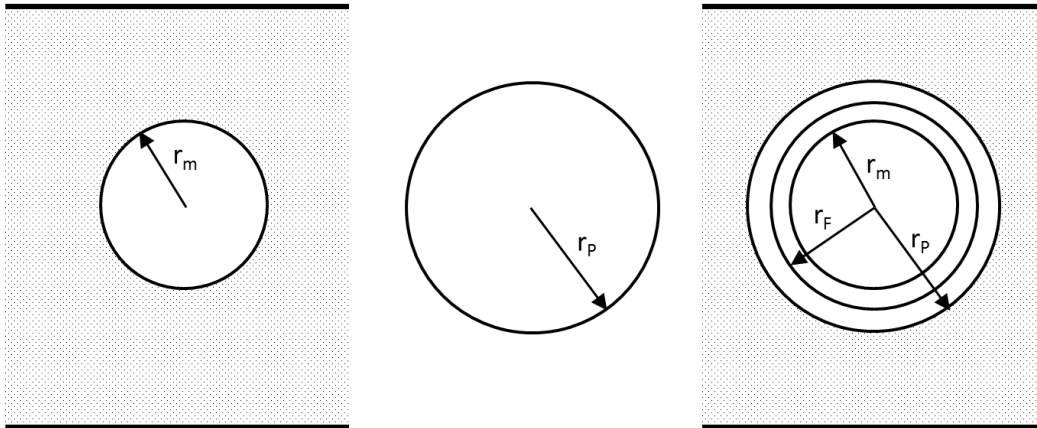


Figure 7: Volume variation of oxygen precipitates and matrix cavity.

According to Ref. [Van87/92], the unstrained radius of a precipitate can be written as

$$r_p = (1 + \delta)r_m \quad (10)$$

where δ is the linear misfit between SiO_x and the Si lattice. The final radius of a precipitate in the silicon matrix is given by

$$r_F = (1 + \varepsilon)r_m \quad (11)$$

where ε is the strain in the precipitate. Combining Eqs. (10) and (11), the final radius is

$$r_F = r_p \frac{(1 + \varepsilon)}{(1 + \delta)} . \quad (12)$$

The strain in the precipitate can be obtained from the linear misfit between the SiO_x and Si lattice, the shear modulus of silicon μ , and the bulk modulus of SiO_x K_p can be found in Refs. [Van87/92, Van05] as follows

$$\varepsilon = \frac{\delta}{1 + \frac{4\mu}{3K_p}} . \quad (13)$$

Finally the elastic strain energy stored in the precipitate is given by

$$\Delta G_\varepsilon = 6\mu\delta V_m \quad (14)$$

and

$$\Delta G_\varepsilon = \frac{6\mu}{\left(1 + \frac{4\mu}{3K_p}\right)} \delta^2 V_m \quad (15)$$

where V_m is the initial unconstrained volume of the matrix. As can be deduced from Eqs. (9) and (14) both the free energy necessary to create the new surface and the elastic strain energy depend on the morphology of oxygen precipitates. In both equations, shape dependent parameters like the surface and the volume of the precipice can be found. In order to reduce the surface energy, the precipitates will adopt the shape characterized by the lowest surface, thus the sphere is privileged. On the other hand, the strain energy would favor the plate-like shape which has the smallest volume. However, the strain energy can be reduced by punching out of dislocations and/or interstitial

emission [Hu86a]. This explains why oxygen precipitates are not only plate-like but have different forms depending on the anneal temperature.

Vacancy absorption can also relieve the strain of the precipitate. If the strain is fully relieved by vacancy absorption only the free energy of formation and the free energy necessary to create the new surface contribute to the total free energy of formation of a nucleus. Fig. 8 illustrates the dependence of the total free energy of formation, the volume free energy of formation, and the free energy necessary to create the new surface as a function of the radius of the nuclei.

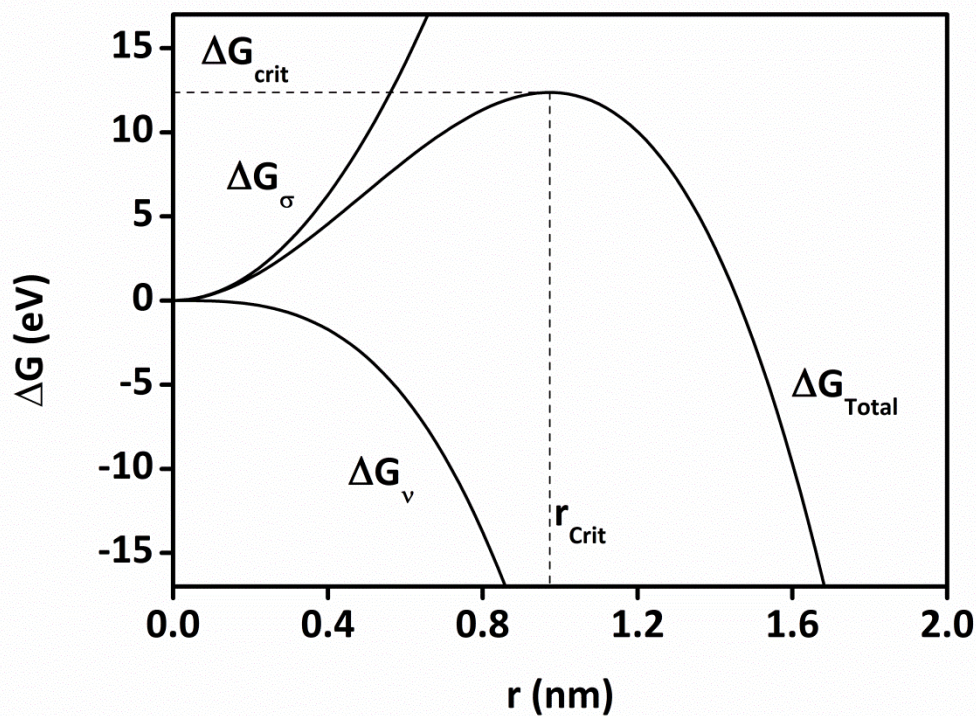


Figure 8: The free energy needed to form a spherical cluster of radius r [San07].

The curve of the volume free energy of formation decreases with increasing radius of the nuclei, while the free energy necessary to create a new interface increases. The sum of these two curves is the total free energy of formation of the nuclei. In the beginning, the absolute value of the free energy necessary to create the new interface is higher than the absolute value of the free energy of formation. However for higher radii this is changed. This gives rise to the maximum in the curve of total free energy. The maximum in the curve of the total free energy determines a critical radius of nuclei r_{crit} . If the radius of the nuclei is smaller than r_{crit} the volume free energy is lower than the surface energy and the nuclei dissolve but if the radius of nuclei is larger than r_{crit} the

volume free energy is higher and the nuclei can grow. The critical radius of the nuclei can be obtained by setting the first derivative of Eq. (7) to zero. The critical radius of nuclei according to Ref. [Van96] is then

$$r_{crit} = - \frac{2 \cdot \sigma \cdot \Omega}{x \cdot k_B \cdot T \cdot \ln \left(\frac{C_{OI}}{C_{OI}^{eq}} \left(\frac{C_V}{C_V^{eq}} \right)^\gamma \left(\frac{C_I}{C_I^{eq}} \right)^{-\beta} \right)} \quad (16)$$

and the critical free energy of formation of nuclei (free energy of formation of nuclei for r_{crit}) is given by

$$\Delta G_{crit} = \frac{16\pi \cdot \Omega^2 \cdot \sigma^3}{3 \cdot \Delta G_v^2} \quad (17)$$

where Ω is the molecular volume per oxygen atom.

It is clear that for low temperatures the equilibrium concentration of interstitial oxygen is low and the critical radius decreases in contrary to high temperatures where the supersaturation degree of interstitial oxygen decreases thus increasing r_{crit} . As a result of this, the function $r_{crit}(T)$ is monotonically increasing with temperature as shown in Fig. 9. The curves split growth of nuclei from dissolution. The nuclei with a radius above the curve will grow while the nuclei with a radius below the curve will be dissolved. As shown by the colored curves, r_{crit} can be significantly decreased by increasing the supersaturation of V.

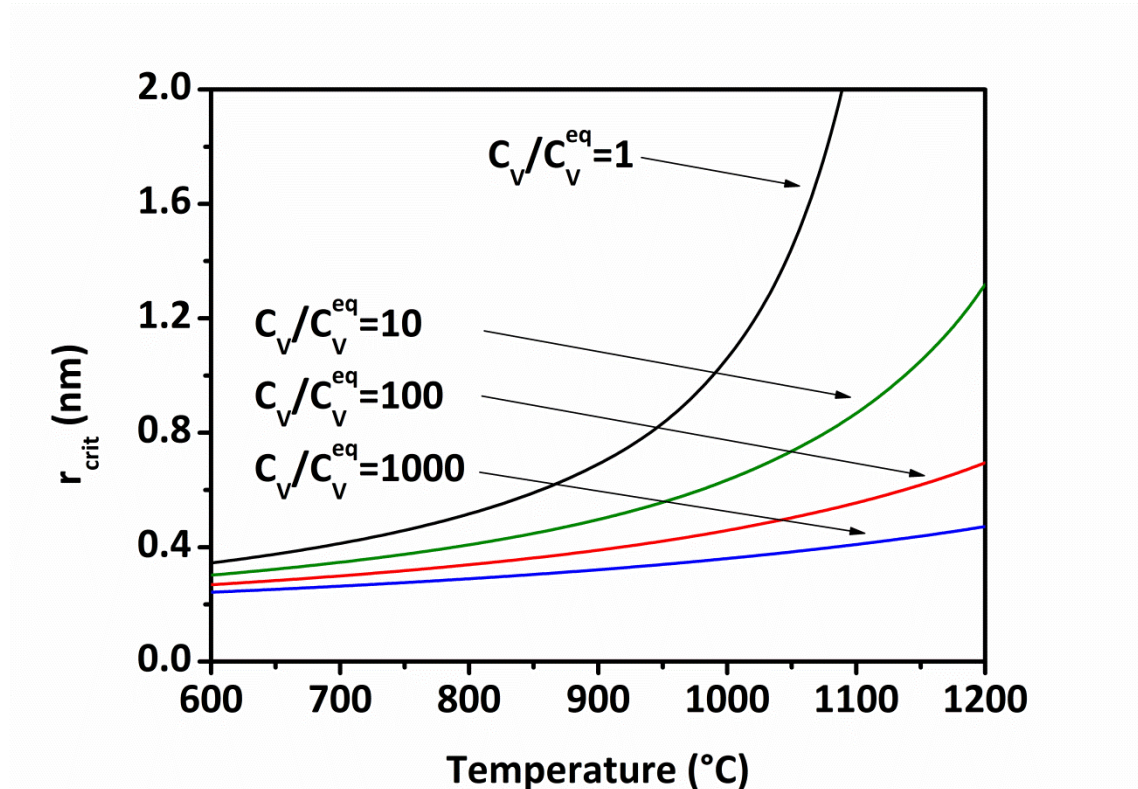


Figure 9: Critical radius as a function of temperature and supersaturation of V.

The nucleation rate is defined as the rate of formation of oxygen precipitate of critical size [Kas00, Tan94]. The general expression for the stationary, time independent nucleation rate according to Ref. [Tak98] is given by

$$J = N_{crit} \cdot \omega \cdot Z \quad (18)$$

where N_{crit} is the equilibrium concentration of oxide precipitate nuclei of critical size in silicon, ω is the frequency of the attachment of interstitial oxygen atoms to the nucleus and Z is the Zeldovich factor taking into account the fact that not every attachment event is successful. The equilibrium concentration of critical nuclei N_{crit} follows the Boltzman distribution and can be expressed as

$$N_{crit} = N_0 \cdot \exp\left(-\frac{\Delta G_{crit}}{k_B \cdot T}\right) \quad (19)$$

where N_0 is the density of nucleation sites. In case of homogeneous nucleation in silicon, N_0 is the concentration of O_i . The frequency of attachment of interstitial oxygen interstitial atom to the nucleus ω according to Ref. [Tak98] is given by

$$\omega = 4\pi \cdot r_{crit}^2 \cdot C_{O_i} \cdot D_{O_i} \cdot d^{-1} \quad (20)$$

where D_{O_i} is the diffusion coefficient of oxygen and d is the atomic distance in silicon (0.235 nm). The Zeldovich factor according to Ref. [Veh07] can be written as

$$Z = \sqrt{\frac{\Delta G_{crit}}{3\pi \cdot k_B \cdot T \cdot n_{crit}^2}} \quad (21)$$

where n_{crit} is the number of oxygen atoms in the nucleus of critical size which can be obtained by dividing the volume of the critical nucleus by the molecular volume of SiO_x . The final form of nucleation rate equation is then

$$J = N_0 \cdot \exp\left(-\frac{\Delta G_{crit}}{k_B T}\right) \cdot 4 \cdot \pi \cdot r_{crit}^2 \cdot C_{O_i} \cdot D_{O_i} \cdot d^{-1} \cdot \sqrt{\frac{\Delta G_{crit}}{3\pi \cdot k_B \cdot T \cdot n_{crit}^2}} \quad (22)$$

Fig. 10 shows an example of the nucleation rate as a function of the temperature for different O_i concentrations calculated according to Eq. 22. As it is clearly seen, the nucleation rate depends on the nucleation temperature and on the concentration of interstitial oxygen.

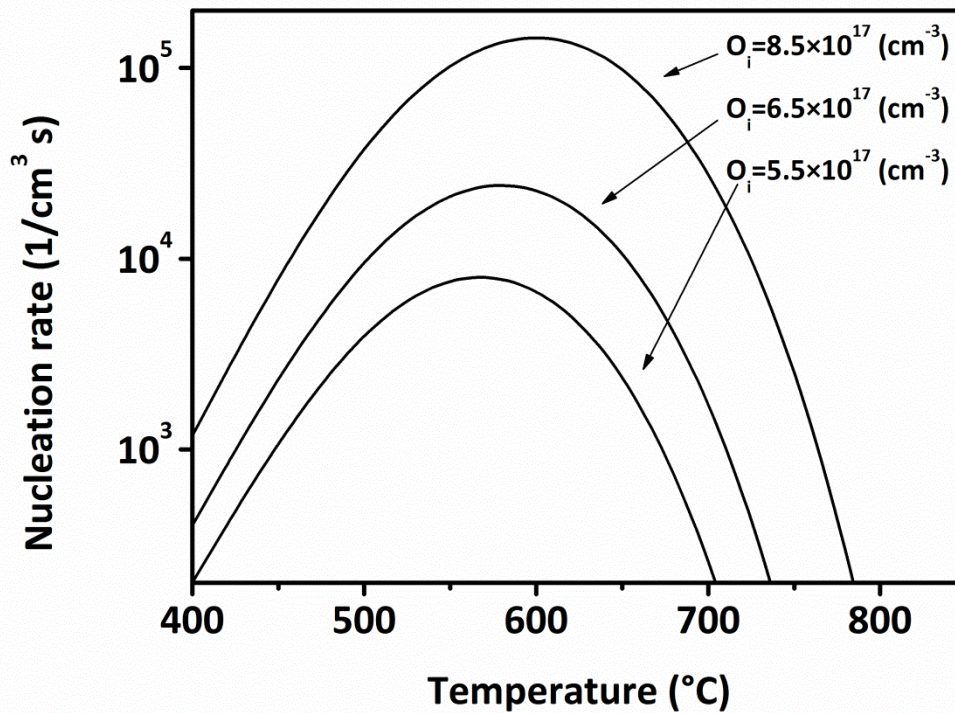


Figure 10: Nucleation rate as a function of temperature and initial concentration of interstitial oxygen.

2.3.2. Heterogeneous nucleation

Nucleation of oxygen precipitates at structural defects of the silicon lattice can significantly decrease the free energy of formation of nuclei. This type of oxide precipitate nucleation is called heterogeneous nucleation. The decrease of the free energy of formation can be achieved by decreasing the strain energy or surface energy or by adding additional negative contributions to the equation of total free energy. The source of heterogeneous nucleation can be impurities like C, B or N, vacancy or agglomerates of self-interstitials [Shi94]. The nucleation at preexisting small oxygen precipitates could be possible which give an energy gain by consuming part of the surface energy [Kis06]. Also, lattice defects like dislocations and stacking faults are reported as possible sites for heterogeneous nucleation [Sum99, Nak00].

2.3.3. Nucleation curves

The nucleation of oxygen precipitates in silicon wafers was investigated since decades [Ino87]. Many of experiments were affected by the thermal history of the samples. This

was the reason of the different results achieved by different researchers. Kelton et al. published nucleation curves for three different oxygen concentrations in the temperature range 400-750 °C and nucleation times up to 64 h. In the beginning, they annealed all samples at 1000 °C for 15 min to achieve identical cluster-size distribution in all samples. The results which they obtained show that the temperature dependent curves of oxygen nucleation have two maxima at about 500 °C and 650 °C. As expected, the density of the precipitates increases with the oxygen concentration in the sample. Moreover, they observed that at temperatures higher than 750 °C the density of precipitates remained below the detection limit. The curves obtained by Kelton et al. are shown in Fig. 11.

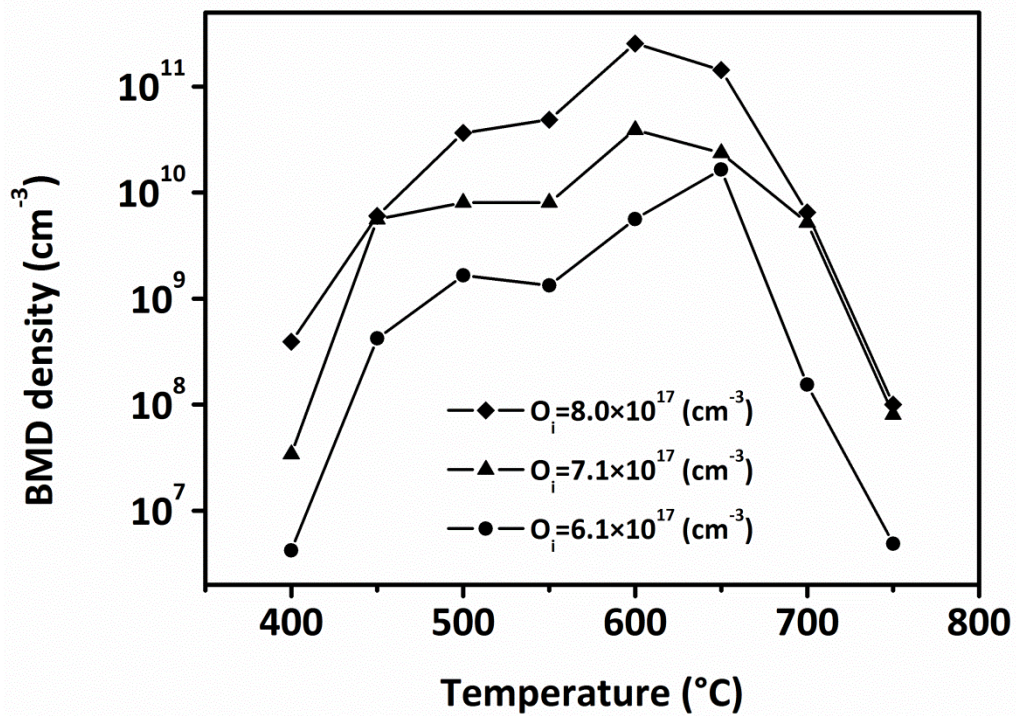


Figure 11: Density of bulk micro defects as a function of concentration of interstitial oxygen for temperatures between 400 °C and 750 °C for 16 h [Kel99].

They have attempted to explain these two peaks by the classical theory of nucleation. They obtained a quantitative agreement between the measured and the calculated densities of oxygen precipitates for the nucleation temperatures greater than 600 °C but for the temperatures below 600 °C the difference between the measured and the calculated densities of the oxygen precipitates were in range of several orders of magnitude [Kel99]. Better results were obtained after applying the “coupled-flux model”

[Kel03]. Although, the data of Kelton provide a lot of information concerning the nucleation of oxygen precipitates in silicon, they do not provide information about the influence of vacancies on the nucleation of precipitates.

2.4. Adjustment of vacancy concentration by RTA pre-treatments

As it was mentioned in the introduction, a well-defined vacancy concentration in the silicon wafers can be established by RTA. The basics of this process are point defect diffusion and the Frenkel-pair mechanism for generation and recombination of vacancies and silicon self-interstitials [Kis07]. The process of adjustment of the vacancy concentration is illustrated in Fig 12. The vacancies and silicon self-interstitials have a very low equilibrium concentration at room temperature as shown in Fig. 12 (a). During heating of the silicon wafer Frenkel-pairs are formed. However, the concentration of Frenkel-pairs is lower than the equilibrium concentration of vacancies and higher than the equilibrium concentration of silicon self-interstitials. Because of this difference, the vacancies will diffuse into the silicon in order to reach their equilibrium concentration and the silicon interstitials will diffuse out from the silicon bulk towards the silicon surface as is shown in Fig. 12 (b). After soak, the vacancies and silicon self-interstitials reach their equilibrium concentrations as shown in Fig. 12 (c). During cooling down, the vacancies and the silicon self-interstitials recombine but because of the difference between the concentrations of vacancies and silicon self-interstitials high concentration of vacancies remain in the bulk. Only at the surface, the concentration of vacancies is lower due to out-diffusion as shown in Fig. 12 (d).

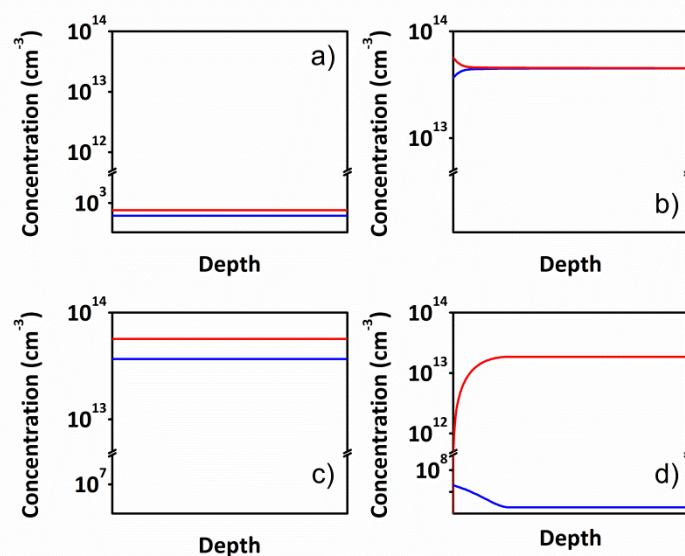


Figure 12: Concentrations of intrinsic point defects at different stages of the RTA process, before heating (a), before soak (b), after soak (c), after cooling (d). The vacancies and silicon self-interstitials are indicated by red and blue line, respectively.

The depth profiles of point defects in the samples pre-treated by RTA can be modeled using the following equations [Fre06]:

$$\frac{\partial}{\partial t} C_I = \frac{\partial}{\partial z} D_I \frac{\partial}{\partial z} C_I - k_{IV} (C_I C_V - C_I^{eq} C_V^{eq}) \quad (23)$$

$$\frac{\partial}{\partial t} C_V = \frac{\partial}{\partial z} D_V \frac{\partial}{\partial z} C_V - k_{IV} (C_I C_V - C_I^{eq} C_V^{eq}) \quad (24)$$

where, D_I and D_V are the diffusion coefficients of silicon self-interstitials and vacancies, respectively, C_I and C_V are the concentrations of silicon self-interstitials and vacancies, t is the time, and z is the depth from the wafer surface. C_I^{eq} and C_V^{eq} are equilibrium concentrations of silicon self-interstitials and vacancies, respectively. The first term to Eqs. (23) and (24) responds for the point defect diffusion and the second one describes the Frenkel-pair mechanism with the reaction constant k_{IV} .

The wafers investigated in this work were pre-treated by RTA at 1100 °C, 1150 °C, 1175 °C, 1200 °C, 1225 °C, and 1250 °C. An example of the ramp of the RTA pre-treatment is shown in Fig. 13.

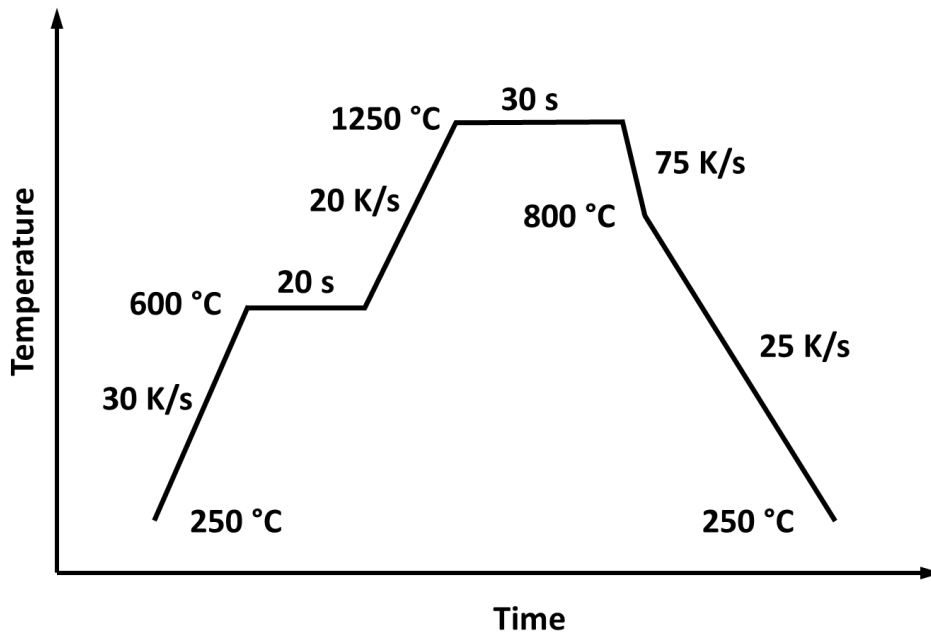


Figure 13: Ramp of the RTA pre-treatment used in the experiments.

Solving Eqs. (23) and (24) for the ramps presented in Fig. 13 and, with the diffusion coefficients and the equilibrium concentrations of silicon interstitials and vacancies from Ref. [Sin97] and reaction constant k_{IV} from Ref. [Bro94], the vacancy profile as a function of the wafer depth can be obtained. Fig. 14 shows the vacancy profiles calculated for six different temperatures of the RTA pre-treatment. The concentrations of the silicon self-interstitials obtained from the calculation were very low therefore the profiles of the silicon self-interstitials were not shown.

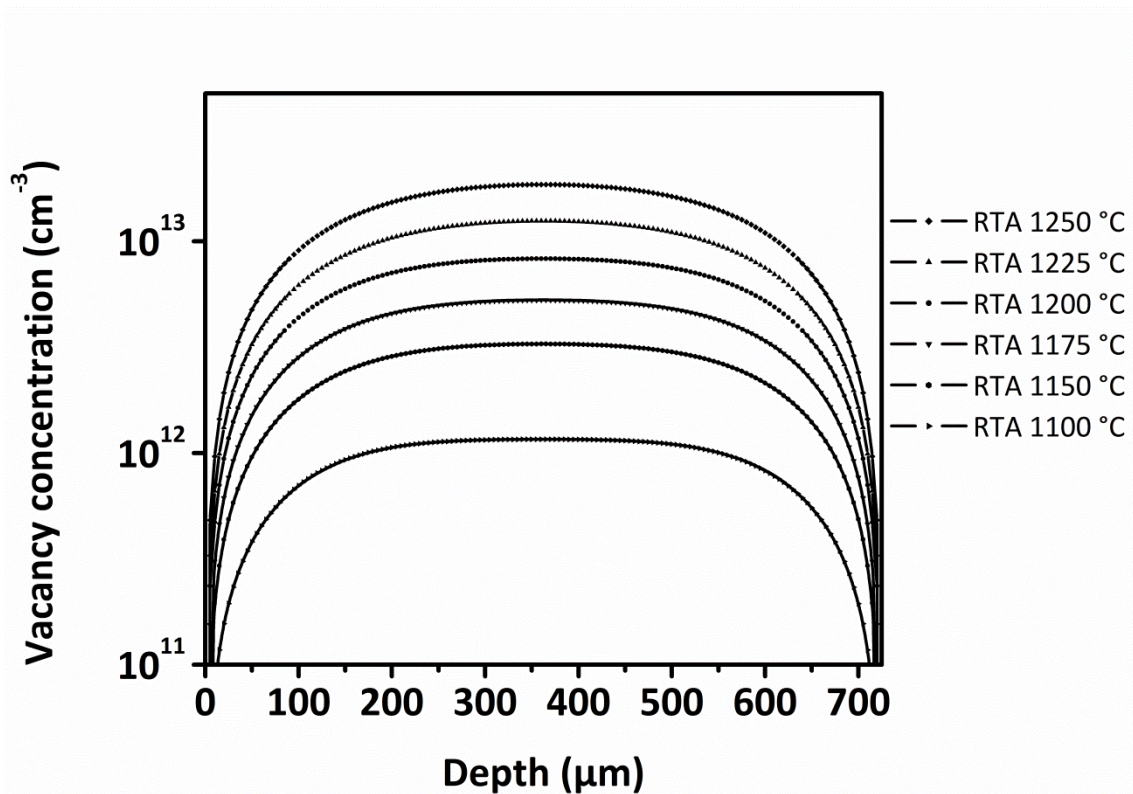


Figure 14: Calculated dependence of vacancy concentration as function of RTA temperature and depth below the surface.

In CZ silicon, the vacancies bind to oxygen and are mainly stored in VO_n complexes. The presence of VO_4 was experimentally evidenced by highly sensitive FTIR in wafers pre-treated by RTA at 1250 °C [Akh09, Kis11].

2.5. Growth of oxygen precipitates

The heat treatment of silicon wafers leads to the growth of oxygen precipitates. With increasing time of annealing the size of the precipitates becomes larger but for temperatures below 800 °C the increase of the precipitates size is very small. In the intermediate range of temperatures, between 800 °C and 1000 °C the growth of oxygen precipitates with the annealing time is significant. Temperatures above 1000 °C can be used as temperatures of pure growth of oxygen precipitates, which allow to obtain oxygen precipitates over hundred nanometer in size. Based on TEM results it was deduced that the size of the oxygen precipitates follows the square root of time [Sue93, Van95]. Based on the Ham's [Ham58] theory for diffusion limited precipitation the authors formulated the growth rate equation of spherical oxygen precipitates as follows [Tak98]:

$$\frac{dr}{dt} = \frac{D_{O_i}}{r} \left(\frac{C_{O_i} - C_{O_i}^{eq}}{C_p} \right) \quad (25)$$

where D_{O_i} is the diffusion coefficient of oxygen where, r is the radius of oxygen precipitate, C_{O_i} and $C_{O_i}^{eq}$ are the concentrations of interstitial oxygen and interstitial oxygen at equilibrium temperature, respectively. For SiO_x , C_p is the concentration of oxygen in the precipitate. $C_p = x/\Omega$ where Ω is the molecular volume of SiO_2 per oxygen atom. Integrating Eq. 25, one obtains the radius as a function time for spherical precipitates

$$r = \left(2 \frac{C_{O_i} - C_{O_i}^{eq}}{C_p} \right)^{0.5} \cdot (D_{O_i} \cdot t)^{0.5} \quad [\text{Van95}]. \quad (26)$$

The diffusion limited growth can be also applied for other morphologies of oxygen precipitate like an oblate spheroid or a plate-like precipitate. The edge length of octahedral precipitates l_{Oct} , length L_{Pl} and thickness d_{Pl} of plate-like precipitates are shown below [Van95].

$$l_{O_{ci}} = (8\pi)^{\frac{1}{3}} \left(\frac{C_{O_i} - C_{O_i}^{eq}}{C_p} \right)^{0.5} \cdot (D_{O_i} \cdot t)^{0.5} \quad (27)$$

$$L_{Pl} = 2\sqrt{2} \left(\frac{(C_{O_i} - C_{O_i}^{eq}) \cdot \sqrt{2}}{\beta_{Pl} \pi C_p} \right)^{0.5} \cdot (D_{O_i} \cdot t)^{0.5} \quad (28)$$

$$d_{Pl} = 4 \left(\frac{\beta_{Pl} (C_{O_i} - C_{O_i}^{eq})}{\pi C_p \cdot \sqrt{2}} \right)^{0.5} \cdot (D_{O_i} \cdot t)^{0.5} \quad (29)$$

where β_{Pl} is the aspect ratio between d_{Pl} and L_{Pl} .

By means of diffusion limited growth one can calculate the maximal size of the oxygen precipitates in the sample after certain time. However, in case of long annealing periods or high concentration of oxygen precipitates the consumption of interstitial oxygen has to be taken into account because this influences on the size of the oxygen precipitates. Therefore, in order to obtain reliable results, Eq. 25 must be modified.

$$\frac{dr}{dt} = \frac{D_{O_i}}{r} \left(\frac{(C_{O_i}(0) - C_{O_i}(Pr)) - C_{O_i}^{eq}}{C_p} \right) \quad (30)$$

Now C_{O_i} is replaced by the difference of the concentration of interstitial oxygen at the beginning of annealing $C_{O_i}(0)$ and the concentration of oxygen in the precipitates $C_{O_i}(Pr)$. The oxygen in the precipitates is the product of the density of oxygen precipitates N and the number of oxygen atoms in the precipitates n

$$C_{O_i}(Pr) = N \cdot n \quad (31)$$

For spherical precipitates n is given by:

$$n = \frac{4\pi \cdot r^3 \cdot C_p}{3} \quad (32)$$

Using Eqs. (30-32) the radius can be calculated numerically.

2.6. Morphology of oxygen precipitates

The oxygen precipitates can adopt various shapes depending on the annealing temperature, annealing time, concentration of interstitial oxygen and vacancy supersaturation. There are small spheres, ribbons, or needle like precipitates in the range of low temperatures (400 °C - 650 °C), square shaped plate-like precipitates on {100} planes with {110} edges in the range of intermediate temperatures (650 °C – 950 °C) and octahedral precipitates bound by {111} planes or polyhedral precipitates in the range of high temperatures (above 950 °C). The appearance of a specified shape of precipitates is not stiffly restricted by the temperature ranges. This means that the temperature ranges typical for certain precipitate morphologies may overlap [Sue93, Ber94, Fuj97].

Prolonged annealing at intermediate temperature can lead to a change of the precipitate morphology as it was shown by TEM as reported by Bergholtz et al. [Ber89]. Their proposed model explains the transformation of a plate-like precipitate to an octahedral precipitate. The thin plate-like precipitate of few atomic layers was formed in a first stage of annealing at 750 °C. Then at one of the ends the thickness of precipitate increases and spreads along the plate. During the following anneal, the thin plate-like became thick and in the following stage it develops fins of octahedral shape. The authors did not provide TEM results of the samples subjected to long enough annealing time to observe the final stage of precipitates. However, one can suppose that the transformation ends with an octahedral precipitate.

A morphology change of precipitates was also observed after two step annealing. The plate-like precipitates formed at a temperature of 800 °C changed their shape to octahedral after annealing at high temperatures (1100 °C) [Has92].

Increasing the concentration of stable nuclei of oxygen precipitates by the sequence of annealing steps at low and high temperature or by the fast neutron irradiation it is possible to impact the precipitates morphology as shown in Refs. [Cui08, Ma05].

A huge influence on the oxygen morphology in silicon wafers has the supersaturation of oxygen in silicon. By decreasing the oxygen supersaturation in samples, the precipitates can grow as octahedral precipitates instead of plate-like. In high range of temperatures (above 1000 °C) the increased supersaturation of interstitial oxygen makes that the octahedral precipitates become a polyhedral precipitates [Fuj97].

The concentration and dimension of plate-like precipitates cannot exceed some limit value compared to the spherical. Moreover it was found that the plate-like precipitates can grow in a dendritic form [Aok93, Bor00].

One should mention that the dopants like N or B and their various concentration levels also influence the precipitate morphology [Wan04, Deg03, Deg04].

2.7. Detection of oxygen precipitates

There are two main investigation methods which are most frequently used in order to determine the density of oxygen precipitates. The first of them is preferential etching. The principle of this method is very simple. The etchant containing a mixture of an oxidizing and an oxide etching component etches the silicon surface in two steps. First, it oxidizes the silicon surfaces and then it dissolves the SiO_2 . Since oxygen precipitates consist of SiO_2 the etchant dissolves the defect much faster than the silicon leaving etch pits behind. The etch pits are mainly attributed to oxygen precipitates. By dividing the number of etch pits per surface area by the etched depth one obtains the density of precipitates per volume unit. So far, various etchants were invented. They are characterized by parameters like etch rate, selectivity or sensitivity. Most commonly used in the industry and in scientific investigations are Sirtl, Wright and Secco etchants [Sir61, Wri75, Sec72]. Unfortunately, they can be harmful to the health due to the Cr IV content. In order to avoid dangerous elements, new Cr-free etchants were developed [Mäh09, Pel10, Kol10]. Defect delineation by chemical etching is a relatively simple method, which does not require expensive equipment however this method is slow compared to LST (laser-scattering tomography). LST provides comparable results to the results of chemical methods in a relatively short time. In this method, the infrared light of a laser beam perpendicular to the surface of a sample is scattered at oxygen precipitates or other defects. The scattered light is observed by optical microscopy using an IR sensitive camera. Using the principle of ultramicroscopy, IR-LST is able to detect defects smaller than the wavelength of the infrared light but similarly to preferential etching it cannot recognize the shapes of oxygen precipitates. Some attempts for the determination of the shape of precipitates by LST were undertaken like in Ref. [Sak97] but LST is mostly used for the determination of the BMD (bulk micro defect) density and defect denuded zone (DZ) [Kis96, Kis00].

For short annealing times, the size of the precipitates can be in the range of a few nanometers which is below the detection limit of both LST and preferential etching. In this case, the size of the precipitates should be increased by an additional annealing step, a so-called “growth anneal”. The temperature of 1000 °C at which the wafers are usually subjected to the growth anneal is a temperature of pure growth of precipitates. This means that only preexisting precipitates grow. After 16 h of growth, the size of the precipitates is sufficiently large and they can be detected. Often in case of small

precipitates, a stabilization step at 780 °C for 3 h or 800 °C for 4 h is carried out in advance [see e.g. Aka02, Kis06a]. Defects in densities higher than $2 \times 10^{10} \text{ cm}^{-3}$ cannot be resolved by LST. This is not a problem for chemical etching where a density of 10^{11} cm^{-3} defects can be measured.

Transmission Electron Microscopy (TEM) is another important method of determination and investigation of oxygen precipitates. TEM is the method not requiring pre-anneal of samples. It gives information about morphology, structure and density of oxygen precipitates. In spite of these advantages, the TEM method is unpractical in the determination of density of oxygen precipitates. The sample preparation is time consuming and for samples with defect density below 10^{10} cm^{-3} the investigation of oxygen precipitates is very difficult.

3. Gettering of metal impurities

The term “gettering” defines the process of reduction of unintentional metal impurities from the electrically-active zone in semiconductor devices. Prerequisite are gettering sinks. These are usually crystal defects which are located outside of the device active region. The impurities are attracted by the strain fields of the defects and diffuse there to be trapped in a region where they are no more dangerous for the devices. Over the years, many gettering techniques were developed and categorized in several groups.

3.1. Metal impurities in silicon

Metals are a group of impurities that has a strong influence on the device performance on the silicon wafer. Especially transition metals like Fe, Ni, or Cu impact significantly the electrical properties of the devices. The high minority carrier capture cross-section of the metals leads to a decrease of the diffusion length and the lifetime of the carriers. Moreover, the generation leakage current which is one of the important device parameters increases with increasing concentration of the impurities. Most of the transition metals are fast diffusing species and even at low temperature their mobility remains fast enough to let them go through the whole thickness of a silicon wafer. This means that even at small concentrations of the impurities a singular atom per cubic micrometer the metal can influence on the electronic properties of devices [Mye00]. In order to reduce the degrading influence of the metal impurities on the devices yield, different gettering techniques are used (see chapter 3.2). The knowledge of the properties of the transition metals is prerequisite for applying efficient gettering techniques.

In this section, the properties of Cu, Ni, and Pd, the contamination species used in this work, are described. Nickel and copper are major impurities in device production therefore they are an object of investigation. Although, palladium does not belong to the main impurities in device production it forms characteristic haze which can be used as a measurement technique of the getter efficiency [Gra95].

3.1.1. Transition Metals Properties

The main metallic impurities in device production are believed to occupy predominantly interstitial sites in the silicon crystal, what is a reason of their rapid diffusion. The temperature dependent diffusion coefficients of Cu, Ni, and Pd are expressed by an equation given as

$$D_M(T) = D_{0M} \cdot \exp\left(-\frac{H_M}{k_B \cdot T}\right) \quad (33)$$

where D_{0M} is the pre-factor and H_M is the migration enthalpy.

Another important propriety of metals in the silicon is their solubility. In the silicon crystal the metals dissolve very weakly and the solubility of the metals decreases exponentially with decreasing temperature. The solubility of meals in silicon can be obtained by the following formula [Gra95]:

$$S_M(T) = 5 \cdot 10^{22} \cdot \exp\left(S_S - \frac{H_S}{k_B \cdot T}\right) \quad (34)$$

Where S_S is the solution entropy and H_S is the solution enthalpy of the metal atoms in silicon with respect to the metal atoms in the silicide phase. Figure 15 shows the diffusion coefficients (right) and the solubilities (left) of Cu, Ni, and Pd obtained from Eqs. (33) and (34) and the parameters given in Tables 4 and 5. Two different set of parameters for the Cu diffusivity in Table 4 are a consequence of the fact that the diffusion of Cu can be affected by the presence of B doping. The positively charged interstitial copper Cu⁺ and the negatively charged substitutional boron B⁻ create pairs. Although, not the all Cu atoms are paired with B atoms and the pairing is temporary, the average diffusion is retarded. The values in Table 4 assigned by the symbol (*) are related to the effective diffusivity of Cu in silicon while the parameters assigned by the symbol (**) are related to the intrinsic diffusivity of Cu. In order to calculate the effective diffusivity of Cu in a Si crystal doped with B, one should use the following equation

$$D_{Cu_{eff}} = \frac{3 \times 10^{-4} \cdot \exp(-2090/T)}{1 + 2.584 \times 10^{20} \cdot \exp(4990/T) \cdot (N_a/T)} \text{ (cm}^2 \text{ s}^{-1}) \quad (35)$$

where N_a is the boron doping level in cm^{-3} [Ist98].

TABLE 4. Diffusion coefficient parameters for Cu, Ni, and Pd [Gra95].

Metal	D_{0M} (cm ² /s)	H_M (eV)	T region (°C)	Ref.
Cu	4.7×10^{-3} (*)	0.43 (*)	400-900	[Gra95]
	3.0×10^{-3} (**)	0.18 (**)		[Ist98]
Ni	2.0×10^{-3}	0.47	800-1300	[Gra95]
Pd	8.0×10^{-2}	0.89	950-1100	[Gra85]

TABLE 5. Solubility parameters for Cu, Ni, and Pd [Gra95].

Metal	S_S	H_S (eV)	T region (°C)	Ref.
Cu	2.4	1.49	500-800	[Web83]
Ni	3.2	1.68	500-950	[Web83]
Pd	1.2	1.64	-	[Gra95]

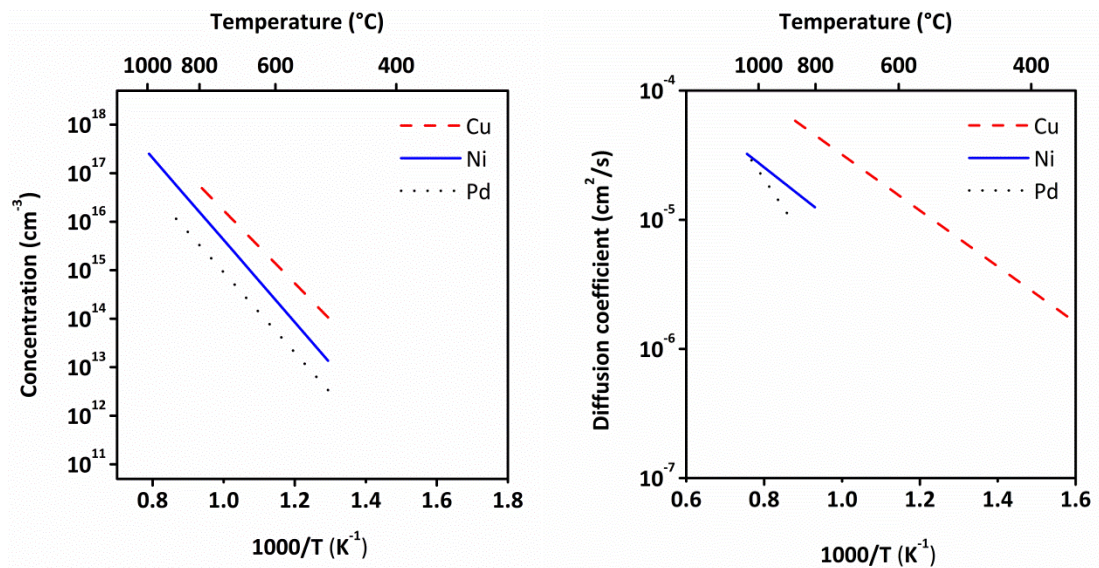


Figure 15: Solubility of Cu, Ni, and Pd in Si (left), diffusion coefficient of Cu, Ni and Pd in Si (right) [Gra95, Gra85, Web83].

The rapid decrease of the metal solubility with decreasing temperature leads to a high supersaturation being a strong driving force for precipitation. Precipitating metals create metal silicides which are different depending on the kind of the metal atom. Nickel and palladium create silicon-rich silicides NiSi_2 and PdSi_2 while copper forms a metal-rich silicide Cu_3Si . The volume change associated with the composition of the silicides can vary significantly. During formation of nickel silicide NiSi_2 at room temperature, the Si atomic volume per metal atom N_{Si} amounts only -0.024 while for Cu_3Si it is +0.55. This value means the number of emitted or absorbed Si atoms per precipitated metal atom. For NiSi_2 , there is almost no change in the volume due to precipitation while for Cu_3Si the relative volume change is around 150 % [Sch02]. The misfit of the various silicides with respect to the silicon lattice and the volume change associated with the formation of silicide precipitates give rise to the formation of secondary defects. The secondary defects formed in consequence of the silicide precipitation and the main physical properties of the metal silicide precipitates are summarized in Table 6.

Table 6. Physical properties of metal silicide precipitates [Sch02, Sei09].

Metal	Silicide	N_{Si}	$\Delta V/V$ (%)	Secondary defects
Cu	Cu_3Si	+0.55	150	Metastable SFs Frank-type SFs Edge dislocations
Ni	Ni_2Si	-0.024	-1.2	Punched-out dislocations
Pd	Pd_2Si	+0.50	100	Edge dislocations

3.1.2. Electrical activity of metals

The transition metals dissolved in silicon lattice are electrically active impurities. Their electrical activity was investigated over a few decades mainly by means of deep level transient spectroscopy (DLTS) and minority carrier transient spectroscopy (MCTS). It was found that the transition metals form deep levels in the silicon band gap [Sei09]. The most frequently referred centers relate to Cu, Ni and Pd atoms are included in Table 7.

TABLE 7. Activation energies (E_A) and capture cross-sections (σ_M) for Cu, Ni and Pd related centers in silicon [Bro87,Gra95].

Cu		Ni		Pd	
E_A (eV)	σ_M (cm ⁻²)	E_A (eV)	σ_M (cm ⁻²)	E_A (eV)	σ_M (cm ⁻²)
Ec-0.161	3.3×10^{-17}	Ec-0.41	-	Ec-0.21	2.7×10^{-16}
Ec-0.402	3.0×10^{-15}	Ec-(0.35-0.38)	-	-	-
Ev+0.093	$>10^{-14}$	Ev+0.33	-	-	-
Ev+0.233	$>10^{-14}$	Ev+0.22	-	-	-
Ev+0.425	$>10^{-14}$	Ev+(0.15-0.18)	-	-	-

The electrical activity of metals is not only the effect of singular atoms but also the effect of metal silicide precipitates. Metal silicide precipitates are extended defects. Their growth contributes to the formation of secondary defects (see Table 6). Both the precipitate/matrix interface and dislocations cause the appearance of centers in the DLTS spectrum. In case of dislocations, there are the well-known lines A at about $E_C - 0.19$ eV, B at about $E_C - 0.3$ eV, C at $E_C - (0.37 - 0.43)$ eV, and D at $E_C - 0.54$ eV. NiSi₂ and Cu₃Si precipitates reveal delocalized band-like states in the DLTS spectrum. In order to understand the complicated electronic states of metal silicide precipitates the reader is referred to literature [Sei99, Sei09].

3.2. Gettering techniques

Already at the beginning of the 1960s, the gettering of metallic impurities was a very important issue in the semiconductor technology [Goe60]. The gettering techniques which were developed so far can be classified into the following categories: external gettering (EG), internal gettering (IG), proximity gettering (PG) and chemical gettering (CG).

External gettering is a category which relates to the place where gettering takes place. In this case, it is the back surface of the silicon wafer. The gettering sites are created by applying of different abrasive methods. One of them is the mechanical damage of the back surface of the silicon wafer by sand-blasting, mechanical abrasion, laser irradiation or ion implantation. Furthermore, the deposition of stress inducing films like silicon nitride or poly-Si films is another possibility for EG. Finally, applying the diffusion of impurities such as boron or phosphorus can also be a source for gettering.

Internal gettering is the next group distinguished by the place of trapping of metal impurities. In this type of gettering, the impurities are gettered in the silicon bulk. The driving force for internal gettering comes from the defects which are mainly oxygen precipitates or secondary defects formed in the process of precipitate growth. The advantage of IG compared to EG is a shorter distance which the impurities must diffuse in order to get from the device active region to the getter sites. This distance is even shorter in the case of proximity gettering. The name of this type of gettering for the first time was used by Wong et al. [Won88]. Proximity gettering is a gettering process which occurs directly beneath a device active zone in the range of about 0.1 to 4.5 μm . In this category, the defects which are in most cases the consequence of ion implantation or proton irradiation create the getter site. Depending on the type of implanted ions, their doses, and implantation energy, one can obtain different types of defects like cavities, dislocation loops, point defects or their clusters which create a gettering layer [Sko95, Sch99, Pér01, Kre05, Bre06]. The proximity gettering layer can also be generated by deposition of epitaxial layers of strained or relaxed SiGe [Lu09]. Also rapid thermal annealing (RTA) can be used to create a defect layer below the surface. It is possible by properly chosen parameters of the RTA treatment which result in layers of nucleation centers located below the surface. After sufficiently long annealing time, the nuclei form a layer of oxygen precipitates being able to getter metal impurities [Lee04, Par06].

Recently reported results demonstrate a method based on wafer bonding. A direct silicon bounded (110)/(001) interface acts as a proximity gettering site for metal impurities [Yu09].

The last category of gettering techniques is the chemical gettering. All techniques aiming on the removal of metal impurities from the wafer surfaces by their evaporation in a process of chemical reaction belong to this category. A well known process is HCl-oxidation. A scheme including all described categories of gettering and the corresponding techniques is shown in Fig. 16.

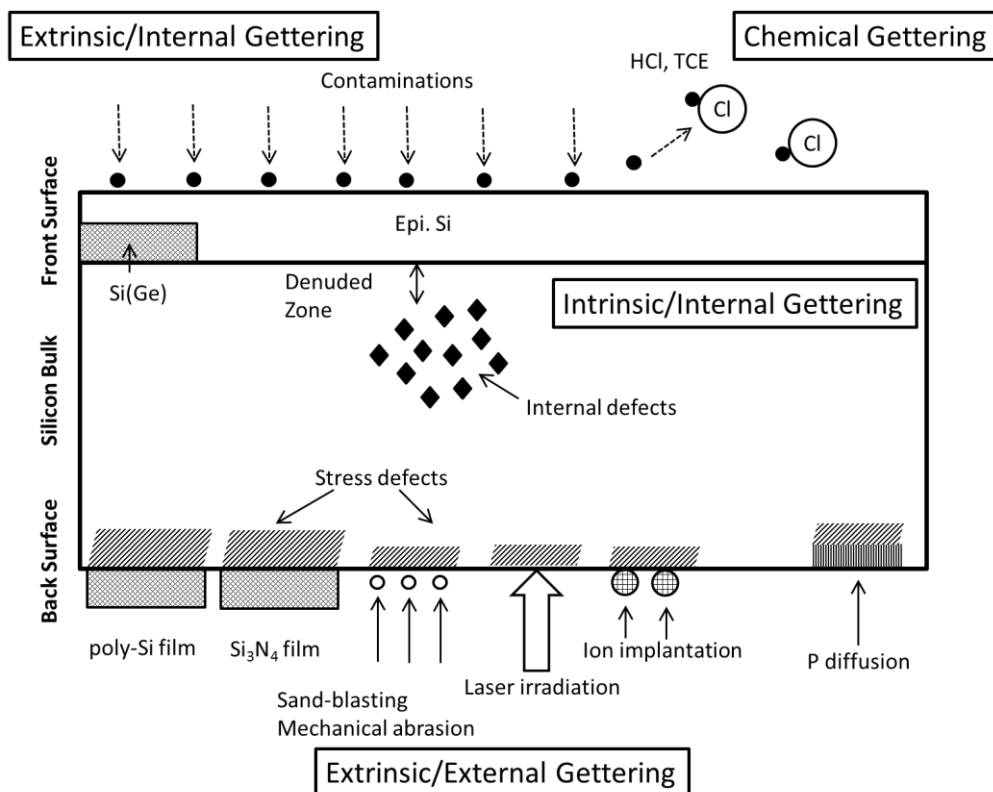


Figure 16: Gettering categories and gettering techniques [Shi94].

3.3. Gettering mechanisms and getting sinks

The getting process in silicon is driven not by a singular getting mechanism but many mechanisms different from each other. They are active or inactive depending on the type of dopant in the silicon material, the type and concentration of defects or the type and concentration of impurities. Below the possible getting sinks for metal impurities in silicon wafers and the getting mechanisms are described.

Oxygen precipitates. This type of defects is most frequently referred as a getter sink for metal impurities. The growing oxygen precipitates create an interface in the silicon matrix at which the metal impurities can be trapped. There are two mechanisms which can be an explanation of this kind of getting. The first mechanism is based on the classical model of heterogeneous nucleation. The getting process occurs mostly during cooling down of the silicon wafer. At low temperatures, the metals become supersaturated. The solubility decreases with decreasing temperature. Such state is energetically unfavorable. Therefore, the metal impurities start to nucleate metal silicide precipitates, thereby lowering energy. The defects present in the silicon bulk become centers for the heterogeneous nucleation of the metal silicides. Because heterogeneous nucleation is much more energetically favorable than homogeneous nucleation, the metals can more easily precipitate in the region containing defects than in the region without defects. The mechanism based on the precipitation of supersaturated impurities at defects is commonly termed “relaxation getting” [Sch91]. The second mechanism which explains getting of metals at the precipitates surface is related to the structure of the precipitate itself. In the case, when precipitates grow incoherently the interface between the oxygen precipitates and the silicon matrix becomes a site at which dangling bonds exist. These are getting sites for metal impurities. For the first time, the surface of oxygen precipitates was used as a criterion for getting by Hölzl et al. [Höl02]. They used the total inner surface (S_{BMD}) of oxygen precipitates normalized by the thickness of the silicon wafer as a criterion for getting of metal impurities. In their work, they determined threshold values of S_{BMD} for Cu and Ni atoms. However, it is still not known where the precise location of the getting sites at oxygen precipitates is. Nevertheless, EBIC micrographs have shown a copper decoration of oxygen precipitates for a Cu concentration in the range from $4 \times 10^{14} \text{ cm}^{-3}$ to $4 \times 10^{15} \text{ cm}^{-3}$ [Ist00].

Due to the molecular volume of silicon oxide which is about two times larger than the molecular volume of silicon, the precipitates are compressively strained. The surface

and elastic energy of precipitates formed at intermediate temperature (650 °C – 950 °C) are relatively high. The most favorable shape of precipitates in this case is plate-like (see section 2.6). At high temperatures, these energies are less important therefore precipitates become octahedrons. Although the precipitates are compressively strained, the silicon matrix surrounding a plate-like precipitate does not have to be compressively strained. As it was shown by Yonemura et al. the strain along the direction normal to the precipitate is compressive and the strain along the direction parallel to the precipitate is tensile [Yon00]. The draft of strain distribution around platelet precipitates is shown in Fig. 17.

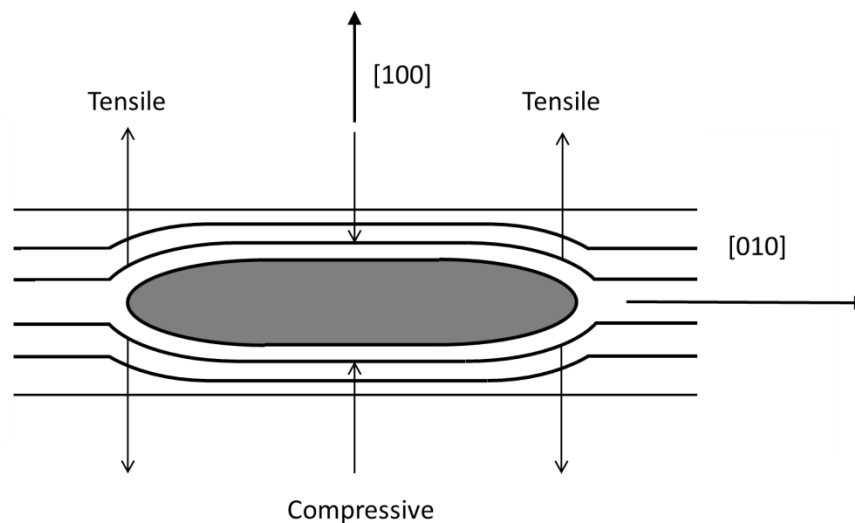


Figure 17: Strain in the Si matrix around a plate-like precipitate.

The silicon lattice at the edge of plate-like precipitates is tensile strained thus creating space for large impurity atoms, thus such a place become a gettering site.

There is a model proposed by Falster et al. assuming that a sufficiently high density of at least 10^7 cm^{-3} of strained plate-like precipitates is required to provide efficient gettering for Cu in silicon wafers [Fal91, Fal04, Fal05]. The model, well known as ninja-theory, is based on the transformation of unstrained, so-called “ninja” precipitates, to a strained form of precipitates. The absence of strain for “ninja” precipitates means that this kind of precipitates is unable to getter impurities in contrast to the strained precipitates.

Further growth of oxygen precipitates increases the stress which must be finally released. This can be done by emission of silicon self-interstitial atoms to the silicon matrix or by punching-out of dislocation loops. Both punched-out dislocation loops and

interstitials are themselves very good getter centers. Moreover, the accumulation of interstitials leads to nucleation of stacking faults. Their surrounding dislocations are also getter sinks for metal impurities [She94]. The punched-out dislocations and stacking faults are a source of dangling bonds attracting charged species while interstitials themselves provide material for silicide [Our84]. The gettering mechanism of dislocations can be also explained based on an elastic interaction arising from the difference in size between solute (impurities atom) and solvent (edge dislocation) atoms as it was suggested in Ref. [Kan89].

Voids are another type of defects which can create getter sites for metal impurities. This type of defects can be introduced into the silicon wafer by ion implantation (see section 2.2.1) or in the case of wafers with low content of oxygen by RTA pre-treatment [Fre06]. Voids can also be formed during crystal growth. These voids are agglomerates of vacancies [Oh00]. Unfortunately, voids can appear on the surface of wafers after cutting out of the silicon ingot. Such voids are commonly called crystal originated precipitates (COPs). The presence of COPs at the wafer surface can degrade the gate oxide integrities [Par01]. Nevertheless, voids are efficient getter centers as shown by the results in Refs. [Kis10, Kis10a]. Depending on the method by which voids are created in silicon wafers their morphology can be different. After ion implantation cavities, a spherical type of voids, vacancies, or vacancy clusters are formed. The RTA introduces nano-size voids and the COPs are several tens of nm in size and their walls are often covered with oxide films. The mechanism of void gettering is explained by gettering to dangling bonds or free space for metal impurities. Moreover, the cavities can serve as unique binding site whose properties are unaffected by occupation of neighboring sites [Mye00]. In such case the gettering effect would be enhanced. During investigation of Cu in cavities by Myers et al. this effect was indeed observed. The researchers explained the phenomenon of strong gettering of cavities by cavity-wall chemisorption [Mye96]. Chemisorption itself is chemical absorption during which very strong chemical bonds are built strongly related with an orientation effect, induction effect, and electrostatic interactions. The possible getter centers and gettering mechanism are summarized in Fig. 18.

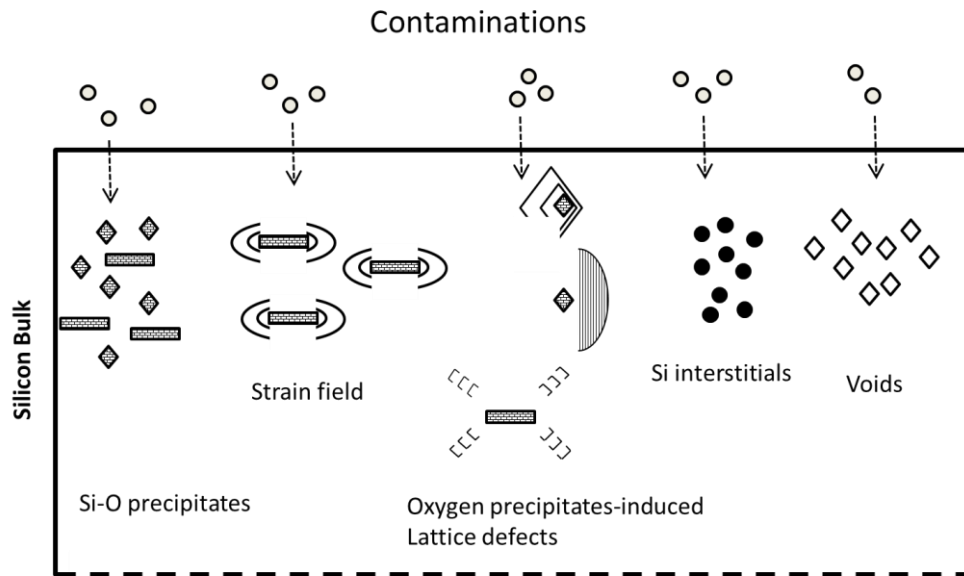


Figure 18: Gettering sinks and accompanied them gettering mechanism in Silicon.

4. Experimental methods and techniques

In this section, the experimental methods and techniques that were used during the investigations are briefly described. The chapter includes only the information which are important to carry out the investigations shown in this work. The main experimental method used in this work was preferential etching. It was used for both defect delineation and the haze getter test. Additional investigations were carried out by means of experimental techniques like ToF-SIMS, STEM or FTIR spectrometry. The investigations were supported by Nomarski microscopy and profilometer measurements. The methods used delivered valuable information about size, density and morphology of oxygen precipitates and about surface contamination with metallic impurities.

4.1. Preferential etching

In this work, the Secco etchant [Sec72] was used for the delineation of defects and metal haze. It consists of HF (50%) mixed with a solution of 44 g $K_2Cr_2O_7$ in 1 l of H_2O in the ratio of 2:1. In order to delineate the defects on (100) wafers, the wafers were cleaved and etched. The defects were investigated on the (110) cleavage plane perpendicular to the (100) surface. An example of etched surface of a sample containing large oxygen precipitates is presented in Fig. 19. Most of the etch pits can be attributed to oxygen precipitates but the pits appearing along lines like the ones marked by a circle in Fig. 19 can be attributed to punched-out dislocation loops.

During etching a part of the sample stuck in a Teflon holder. This results in a step which was measured by a profilometer giving the value of etched depth. Dividing the number of defects counted by the area of investigation and etched depth one can obtain the density of defects per unit volume, the so called bulk micro defect density (BMD).

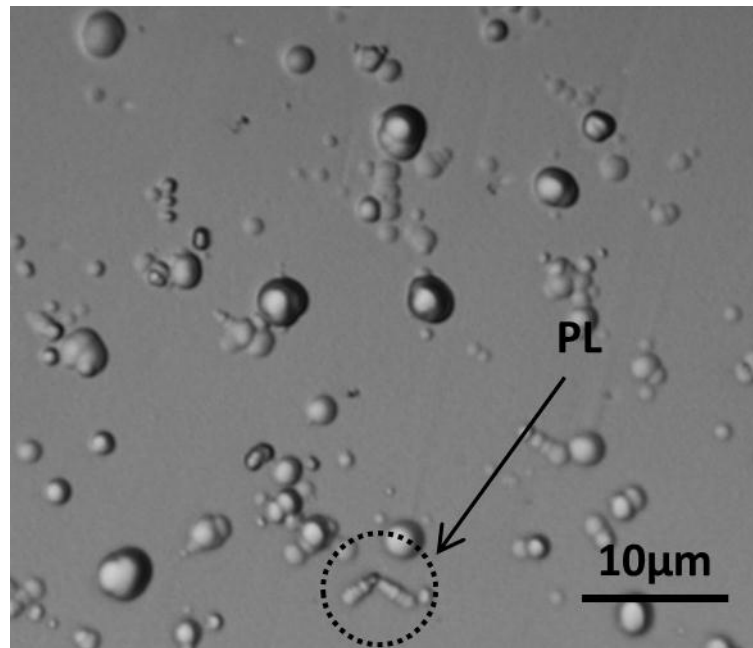


Figure 19: Etch pits observed after etching for 3 min in Secco.

4.2.STEM

A modern scanning transmission electron microscope (STEM) the FEI Tecnai Osiris was used in order to investigate the morphology of oxygen precipitates and the presence of metallic contaminations. The microscope is equipped in three detectors: a bright field (BF), a dark field (DF), and a high angle annular dark field (HAADF) detector which all can be used simultaneously. The BF images contain crystallographic information. However, a significant benefit of the STEM is offered by the dark field operation like HAADF imaging. In this mode, no Bragg diffracted electrons only the elastically scattered electrons are collected which passed very close to the atomic nuclei in the sample. The HAADF signal is directly proportional to the density and thickness of the specimen and proportional to $Z^{3/2}$ where Z is the atomic number. Thus, the HAADF images are characterized by material contrast. A scheme of an STEM is shown in Fig. 20.

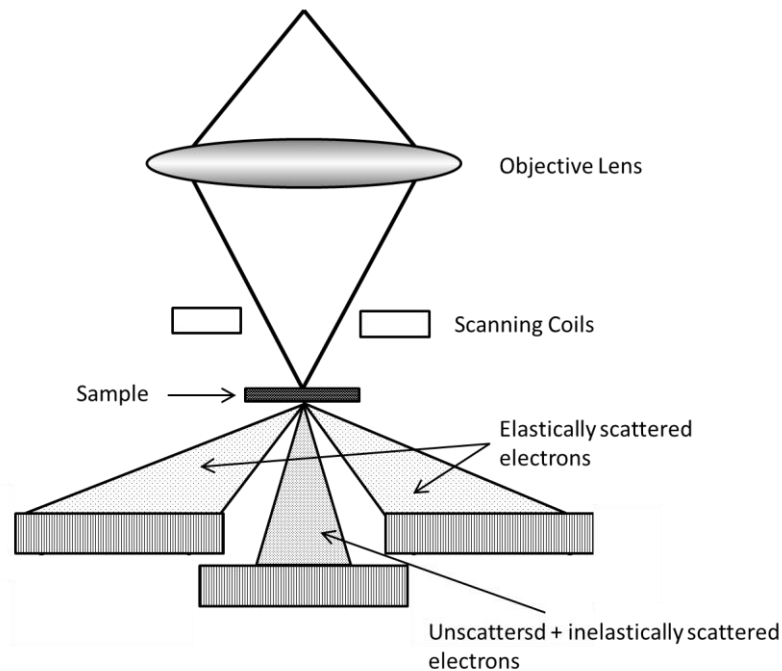


Figure 20: Scheme of a STEM microscope.

4.3.FTIR

Fourier transform infrared spectroscopy was used to determine the concentration of interstitial oxygen atoms and the morphology of the oxygen precipitates. While, the determination of the concentration of interstitial oxygen by means of FTIR is a commonly used method, the determination of the morphology of oxygen precipitates requires low temperature measurements e.g. at liquid helium. The temperature investigation of the bands attributed to oxygen precipitates by FTIR spectroscopy at room temperatures is problematic because of the close neighborhood of the strong bands of interstitial oxygen. The bands overlap and they are difficult to distinguish. However, measurements carried out at low temperature avoid this problem. The bands of precipitates and interstitial oxygen atoms are well separated as is shown in Fig. 21 (a). There are two characteristic broad bands at 1095 cm^{-1} and at 1225 cm^{-1} which belong to spherical and plate-like precipitates, respectively. The other sharp bands (1136 cm^{-1} and satellites and 1205 cm^{-1}) are attributed to interstitial oxygen. In order to observe precipitate-related bands in heat-treated samples, the loss of interstitial oxygen between an unannealed sample and an annealed sample must be significant otherwise the bands of the oxygen precipitates will be too weak. An example of a spectrum which belongs to a sample in which the oxygen loss is too small is shown in Fig. 21 (b). There the bands of the precipitates are not seen and only the peaks of the thermal double donors (TDD) are an evidence that the samples were annealed. In an as-grown sample only the bands of O_{2i} or O_i are present in the investigated range as shown in Fig. 21 (c).

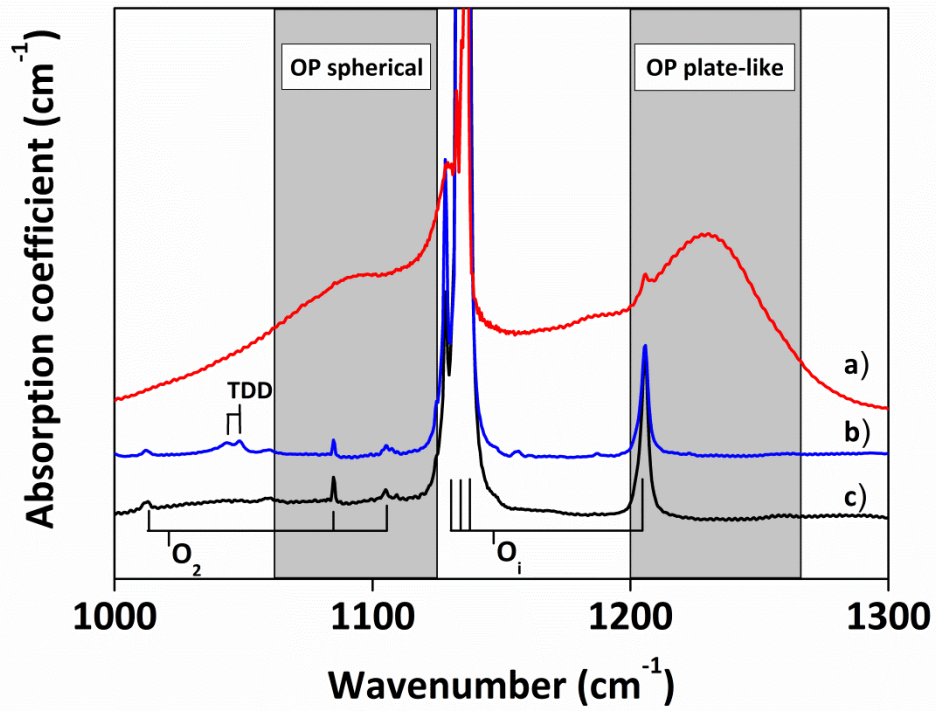


Figure 21: Examples of FTIR spectra taken at liquid helium temperature: spectrum of samples with oxygen precipitates (a), sample with thermal double donors (b), as grown sample without annealing (c).

4.4.Haze getter test

A haze getter test is a type of test which is used for the qualitative estimation of the getter efficiency in silicon wafers. The principle of this test is the so-called haze which can be observed on the front surface of a silicon wafer after contamination with metal at the back surface followed by annealing at temperature about 1000 °C and chemical etching [Gra95]. Depending on the type of the metal, different forms of the haze can be observed. Fig. 22 shows typical etch pits of the haze observed in samples contaminated with Cu (left) and Ni (right). If the sample contains defects in the bulk, the metal atoms are gettered and the observed haze is weaker or completely disappears. Thus, comparing density of the etch pits of the haze in the sample without defects and with defects one can estimate the getter efficiency. In this work, the haze getter test was carried out with following steps. First, the samples were dipped in HF (5%), then contaminated by scratching the back surfaces with wires of Cu, Ni and Pd. In order to diffuse the metal atoms into the silicon bulk, the samples were annealed at 900 °C for 10 min in air. After the so-called drive-in step, the samples were again dipped in HF (5%) and etched in Secco etchant for 3 min. The getter efficiency η_{Haze} was determined according to Eq. 36.

$$\eta_{Haze} = \left(1 - \frac{N_{hv}}{N_{Ref}} \right) \cdot 100\% \quad (36)$$

where, N_{hv} is the number of etch pits on the investigated sample and N_{Ref} is the number of etch pits on the referential sample. The referential sample was cut out from a p-type as-grown wafer.

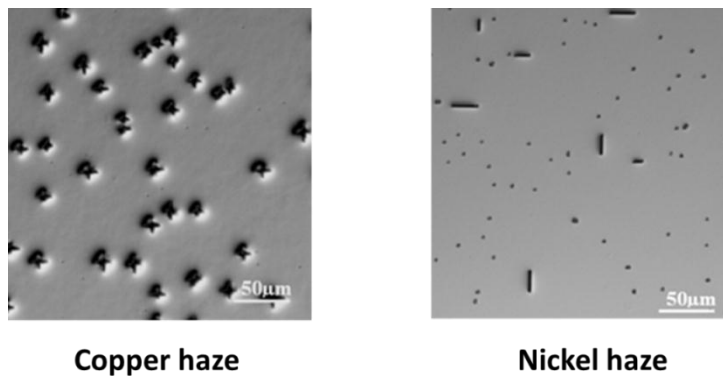


Figure 22: Etch pits of Cu and Ni Haze.

4.5.ToF-SIMS

The time of flight secondary ions mass spectroscopy (ToF-SIMS) is a technique used in this work for the measurement of the surface concentration of Cu. The measurement of the Cu concentration by means of ToF-SIMS is the basis of the ToF-SIMS 7 day storage getter test. The development of this test and the flow are described in chapter 6.5. The principle of the ToF-SIMS is illustrated in Fig. 23. A Bi ion beam is focused on the silicon sample. As the result of this impulse secondary ions are ejected and fly to the detector. The time of flight of ions having different mass is measured and subsequently converted to their mass. The final result is a spectrum presenting the intensity of counts as a function of the mass.

In order to investigate the Cu concentration, an area of $500 \times 500 \mu\text{m}^2$ was analyzed by Bi ions with an energy of 25 keV. The value of the Cu concentration was determined by the ratio of the peak area of the ^{63}Cu and the ^{28}Si isotopes multiplied by the relative sensitivity factor (RSF) provided by ION-TOF the manufacturer of ToF-SIMS.

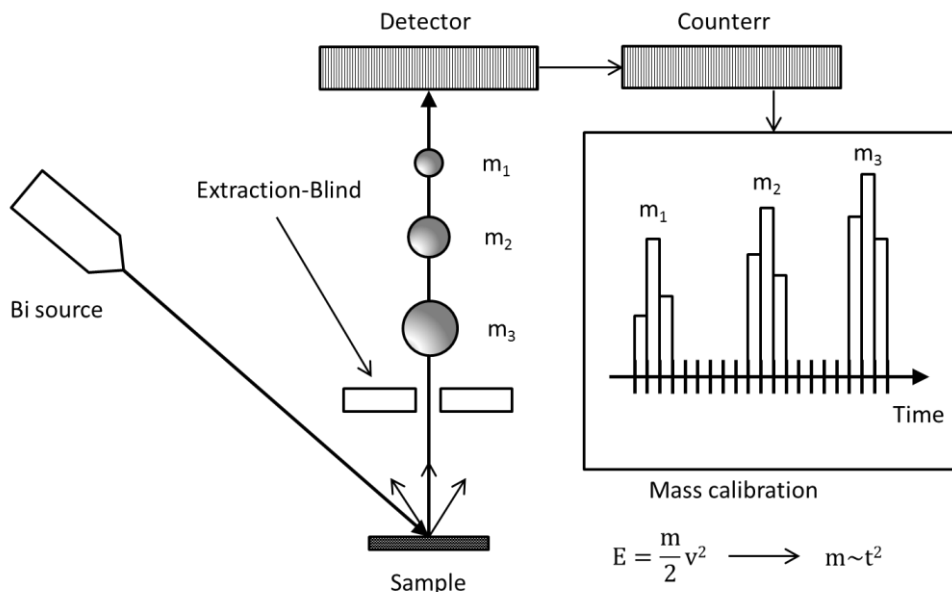


Figure 23: Principle of ToF-SIMS.

5. Aim of this study

The aim of this study was to investigate the influence of vacancies on the nucleation of oxygen precipitates, their size and morphology. Additionally, the investigations on the impact of vacancy on the getter efficiency were a particular point of interest. These all issues are very important for the development of future silicon wafers, especially in terms of the design of getter sites for metal impurities.

Detailed goals of this work can be listed as follows:

1. Investigation of the nucleation of oxygen precipitates in a broad range of nucleation temperatures for samples pre-treated by RTA at different temperatures in order to generate well defined vacancy profiles in the wafers.
2. Detailed investigation of the morphology and the size of oxygen precipitates by means of FTIR spectroscopy and STEM.
3. Investigation of the getter sites for metal impurities by STEM and EDX.
4. Investigation of the getter efficiency of oxygen precipitates for Cu, Ni, and Pd in samples pre-treated by RTA for high concentration of metals.
5. Development of a getter test for the investigation of the getter efficiency in samples contaminated with 10^{12} - 10^{13} cm⁻² of Cu and investigation of getter efficiency these samples.

6. Results and discussion

This chapter is concerned with the influence of a vacancy supersaturation on the behavior of oxygen in silicon wafers. The detailed studies are directed to such issues as nucleation of oxygen precipitates, influence of vacancies on the morphology and size of oxygen precipitates, and gettering efficiency of oxygen precipitates formed in vacancy supersaturated wafers.

In section 6.1 the influence of the vacancy supersaturation on the nucleation of oxygen precipitates is shown. The nucleation curves obtained for different vacancy supersaturations are analyzed and compared with the results of samples without vacancy supersaturation. In addition, the nucleation kinetics at the peaks of the nucleation curves was studied.

The next section, 6.2, is devoted to the investigation of the influence of the vacancy supersaturation on the morphology and size of the oxygen precipitates. The precise morphology and the size of the precipitates were determined by means of STEM equipped with an EDX detector. The size of the oxygen precipitates was compared with the size obtained by theoretical diffusion limited equations of precipitates growth. Finally, samples contaminated with low and high concentration of Cu were investigated in order to find out where the getter sink at the oxygen precipitates is.

Further information about the morphology of the oxygen precipitates obtained by analyzing FTIR spectra were discussed in section 6.3. The main attention was focused on the assignment of the absorption bands attributed to the different morphologies of oxygen precipitates.

The two last sections are dedicated to investigations of the getter efficiency of oxygen precipitates formed in vacancy supersaturated samples. In section 6.4, the well known haze getter test was used to determine the getter efficiency of Cu, Ni, and Pd in samples contaminated with high concentrations of the metals. Section 6.5 provides the results obtained on the samples contaminated with low concentration of Cu. In order to investigate the getter efficiency in the samples contaminated with low concentration of Cu, a ToF-SIMS getter test was developed. In the both section devoted to gettering experiments the oxygen precipitates and extended defects like punched-out dislocation are assumed as possible getter sites for metal impurities.

6.1. Nucleation of oxygen precipitates in RTA pre-treated wafers

6.1.1. Introduction

Although, the precipitation of oxygen in silicon substrates supersaturated with vacancies was investigated since the end of the 90`s still a lot of information on this topic is missing. Especially noticeable is the lack of results giving information about vacancy dependent nucleation curves as they were shown by Kelton et al. for pre-annealed wafers [Kel99]. Until now, the works which can be found in the literature reported about the enhancement of the oxygen precipitation the vacancy supersaturated samples due to RTA pre-treatment at different temperatures and for different soak time [Pag97, Fal97]. Further works are concerned with the influence of the gas ambient and the cooling rate of RTA on the oxygen precipitation [Aka02].

The data of homogenized samples published by Kelton et al. provide a lot of valuable information about the temperature dependent nucleation of oxygen precipitates in silicon wafers. They showed double-peak spectra (Fig. 11) what cannot be explained by classical nucleation theory assuming one type of spherical nucleation centers, where the nucleation curve would show just one peak as seen in Fig. 10. The peak position is the result of the supersaturation of interstitial oxygen, which decreases with increasing temperature, and the oxygen diffusivity which increases with increasing temperature. Although, the peak at higher temperature can be explained based on the classical nucleation theory the explanation of the peak at lower temperature is not possible.

In this chapter, the influence of the vacancy supersaturation, introduced into the silicon samples by RTA pre-treatment, on the nucleation of oxygen precipitates is shown. The BMD density as a function of the nucleation temperature measured for different RTA temperatures was analyzed in terms of the nucleation rate of oxygen precipitates and possible nucleation centers. Moreover, the nucleation kinetics for the chosen nucleation temperatures is discussed in terms of the critical radius of the nuclei. The nucleation of oxygen precipitates was investigated in the temperature range between 400 °C and 1000 °C thus in a wider range than in Ref. [Kel99]. However, in the samples with high supersaturation of vacancies even at 1000 °C an enhanced density of BMDs was observed.

6.1.2. Experimental details

The samples used for the investigations are mainly cut out from two types of wafers. One part of samples was cut out from B-doped (100) CZ-Si wafers 200 mm in diameter with resistivity of about 10 Ωcm . The concentration of interstitial oxygen according to DIN 50438/1 was $6.5 \times 10^{17} \text{ cm}^{-3}$. This type of samples will be named in the following “low O_i ”. The second type of wafers used was B-doped (100) CZ-Si 150 mm in diameter with a resistivity of about 50 Ωcm . The concentration of interstitial oxygen according to DIN 50438/1 was $8.5 \times 10^{17} \text{ cm}^{-3}$. This type of wafer will be called “high O_i ”. Both wafer types were polished at the front side and etched at the back side.

The samples used for the nucleation experiments were cut out from the low O_i wafers. First, the wafers were pre-treated by RTA at temperatures of 1250 °C, 1225 °C, 1200 °C, 1175 °C, 1150 °C, and 1100 °C for 30 s in Ar atmosphere containing 1000 ppm of oxygen. Then the wafers were cut into pieces of 35×35 mm size which were annealed at different temperatures in the range of 450 °C to 1000 °C for 1 h, 4 h, 8 h, and 16 h in N_2 . In order to determine the BMD density, the samples annealed at temperatures below 750 °C were annealed additionally at 780 °C for 3 h and 1000 °C for 16 h in N_2 . Because of rapid heating of the samples with a rate of 100 K/min only part of the precipitates can survive the growth anneal. The annealing step at 780 °C for 3 h stabilizes a large part of the precipitates that they become able to survive the subsequent step at 1000 °C. It is clear that not all precipitates which are formed at low temperatures survive the growth anneals and that the concentration of survived precipitates depends on the time of nucleation. For the samples with nucleation at temperatures higher than 750 °C, the size of the precipitates is larger than the critical radius at 780 °C and therefore the stabilization step at 780 °C was omitted.

The samples annealed at temperatures higher than 750 °C were annealed only at 1000 °C for 16 h in N_2 . This step is commonly called “growth anneal” and for simplification in the further parts of this work this name will be used.

The RTA pre-treatment is used in order to generate different concentration of vacancies in the silicon samples. The concentrations of vacancies formed by the different RTA pre-treatments can be found in chapter 2.4. The annealing step which follows the RTA pre-treatment is called “nucleation annealing”. During this step the oxygen precipitates nucleate. The growth anneal is an annealing step required for the detection of the oxygen precipitates formed during the nucleation anneal which are too

small to be detected by etching. The ramps of the nucleation and growth anneals are shown in Fig. 24.

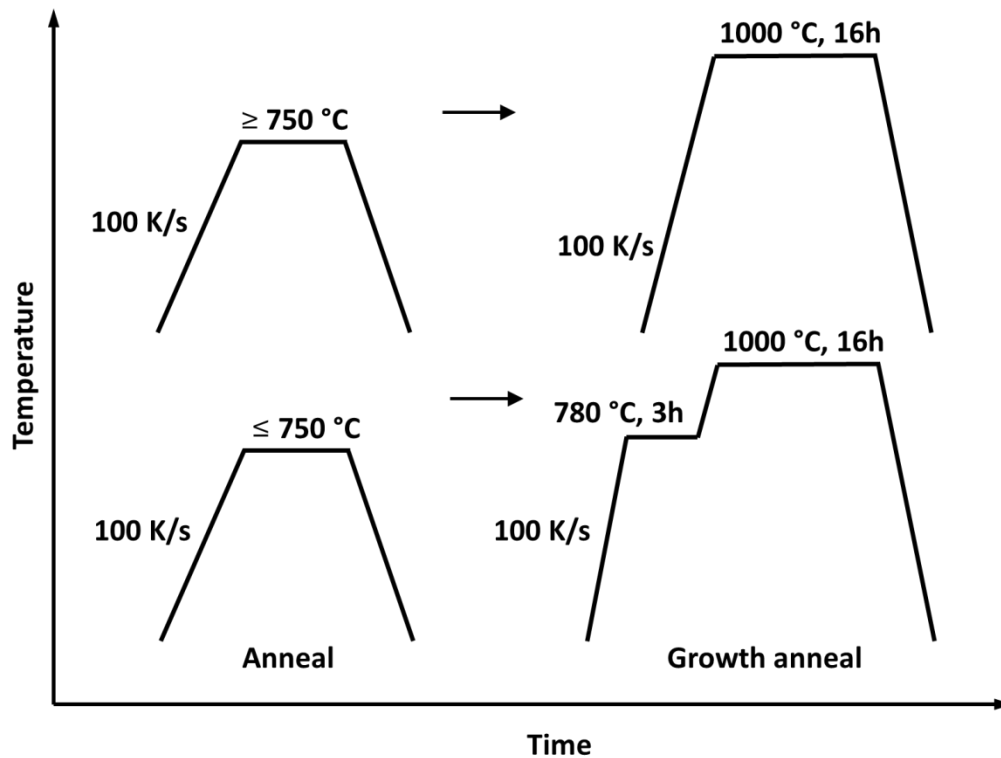


Figure 24: Ramps of the nucleation anneal and growth anneals.

6.1.3. Results and discussion

BMD densities and ΔO_i as a function of the nucleation temperature and vacancy supersaturation

Fig. 25 shows the BMD densities (left) and ΔO_i (right) both as a function of the nucleation temperature for various nucleation times and for different temperatures of RTA pre-treatment, thereby for different initial vacancy supersaturation. The black vertical line on the graphs splits the part of the data obtained on the samples subjected to nucleation anneal followed by a growth anneal with stabilization step (left) from the part of the data obtained on the samples subjected to nucleation anneal followed by the growth anneal without stabilization step (right). In Fig. 25, one can clearly see that the BMD density and ΔO_i increase with increasing temperature of RTA pre-treatment for all nucleation temperatures. Moreover the curves exhibit three characteristic maxima.

Two of them, the ones located at around 450 °C and 650 °C, are seen for the samples pre-treated by RTA at all of the temperature investigated while the third maximum, located at 800 °C, is observed only for the samples pre-treated by RTA at 1250 °C, 1225 °C, and 1200 °C. The maxima at 450 °C and at 650 °C appear also in the samples without vacancy supersaturation as shown by the data of Kelton et al. marked in Fig. 25 by gray lines with empty triangles. The BMD densities obtained on the samples pre-treated by RTA are in most cases higher than the BMD densities of Kelton, although the concentration of interstitial oxygen in Kelton's samples was somewhat higher with $7.1 \times 10^{17} \text{ cm}^{-3}$.

The BMD densities as a function of the nucleation time at the temperature of the three maxima and 1000 °C are plotted in Fig. 26. The temperature of 1000 °C is first of all a temperature of growth of oxygen precipitates. The data of time "0" presented here belong to samples subjected only to the growth anneal with and without stabilization step for the nucleation annealing at temperatures below 750 °C and above 750 °C, respectively.

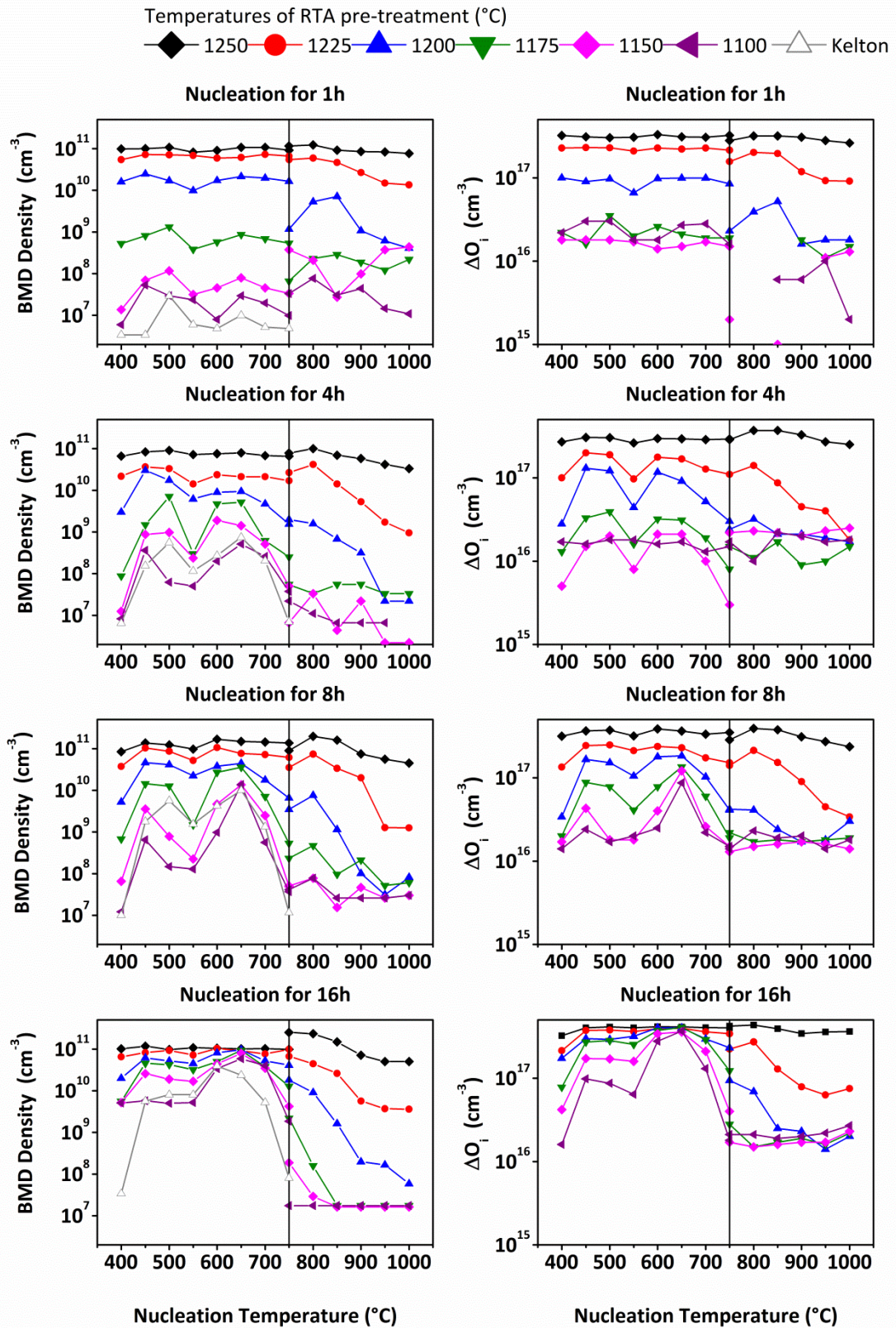


Figure 25: BMD density (left) and ΔO_i (right) as functions of the nucleation temperature for various times and RTA temperatures.

Nucleation kinetics

As it is shown in Fig. 26, the dependencies of the BMD density on the nucleation time in the samples pre-treated by RTA at various temperatures and subjected to nucleation annealing at temperatures of 450 °C, 650 °C, 800 °C, and 1000 °C are different. The BMD density depends on the temperature of the RTA pre-treatment and the temperature of nucleation anneal.

The nucleation kinetics at 450 °C strongly depends on the temperature of the RTA pre-treatment. The BMD densities in the samples pre-treated by RTA at 1200 °C and at higher temperatures are almost on the same level after one hour of nucleation anneal. In the case of the samples pre-treated by RTA at temperatures lower than 1200 °C, the BMD density monotonically increases with increasing time of nucleation. After 16 h of annealing, the difference of the BMD density in the samples pre-treated by RTA at various temperatures still exists. The data of Kelton et al. presented in this graph are similar to the data determined in the samples pre-treated by RTA at 1100 °C. This would mean that sample pre-treatment by RTA at 1100 °C has a similar homogenization effect like annealing at 1000 °C for 15 min.

The next dependencies of the BMD density on the nucleation time presented in Fig. 26 regards the nucleation annealing at 650 °C. The appearance of the curves is similar to the curves observed for the samples annealed at 450 °C. The only difference is the faster increase of the BMD density with the nucleation time in the samples pre-treated by RTA at temperatures lower than 1200 °C. As a consequence, the BMD densities saturate after a nucleation time of 16 h in all samples pre-treated by RTA. The data of Kelton et al. are analogous to the data obtained on the samples pre-treated by RTA at the two lowest temperatures.

The dependence of the BMD density on the nucleation time at 800 °C differs significantly from those at 450 °C and 650 °C. After the growth anneal (nucleation time “0”), the BMD densities increases with increasing temperature of the RTA pre-treatment. There is also a jump of the BMD density between the nucleation time “0” and 1 h for all samples. The further extension of the nucleation time in all samples pre-treated by RTA does not change the BMD density anymore.

An extended annealing time at 1000 °C does not influence the BMD density. Although the BMD density increases with the temperature of the RTA pre-treatment the BMD densities after “0” and after 16 h are almost the same for each of the samples.

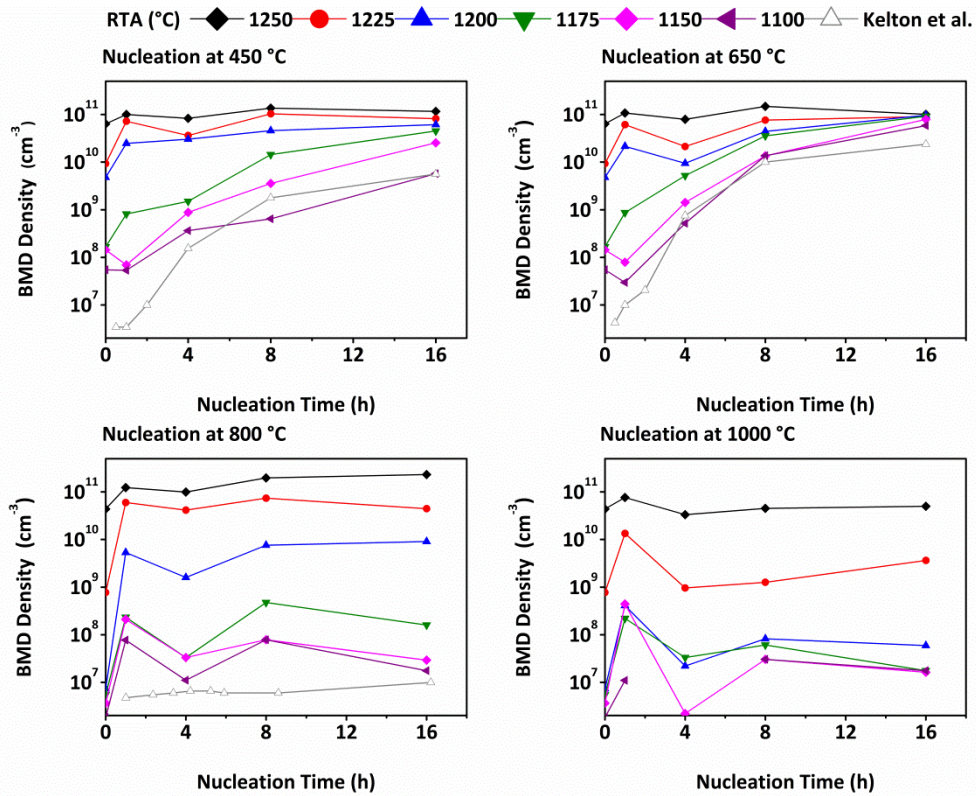


Figure 26: BMD density as a function of the nucleation time in the samples pre-treated by RTA at various temperatures.

The behavior of the BMD density in the samples pre-treated by RTA and subsequently annealed at 450 °C, 650 °C, 800 °C, and 1000 °C can be explained by considering the distributions of the oxygen precipitates after the annealing steps.

Fig. 27 (a) shows a schematic size distribution of oxygen precipitates after the homogenization step at 1000 °C for 15 min [Fal97a]. This distribution should look similar in the samples pre-treated by RTA. In the samples subjected to nucleation annealing at 450 °C or 650 °C for different times, the maximum concentration of precipitates moves towards larger values of r as shown in Fig. 27 (b). The subsequent growth anneal at 780 °C for 3 h plus 1000 °C for 16 h determines the amount of oxygen precipitates which will be seen after chemical etching. If the nucleation time is too short as in case of t_1 , a low density of precipitates survives the stabilization step and the subsequent growth step reveals mainly the precipitates with the critical radius which exceeds the critical radius at 1000 °C (pattern fill). The extended annealing at 450 °C or 650 °C allows more precipitates to survive the annealing at 1000 °C what is shown in Fig 27 (c). Increasing the nucleation time at 450 °C or 650 °C, times t_2 and t_3 in the figure, will increase the concentration of the oxygen precipitates after the growth step. Sufficiently long annealing time for nucleation at lower temperatures moves the peak of

the distribution to values exceeding the critical radius at 780 °C and most of the precipitates can survive the growth step. In this point, the BMD density observed after chemical etching saturates at nucleation temperatures of 450 °C and 650 °C as shown in the experimental results of Kelton et al. and in the results of the samples pre-treated by RTA at temperatures lower than 1200 °C in Fig. 26 (top). In the case of annealing at 450 °C, the saturation process will take much longer because of a lower nucleation rate of the precipitates at 450 °C compared to 650 °C.

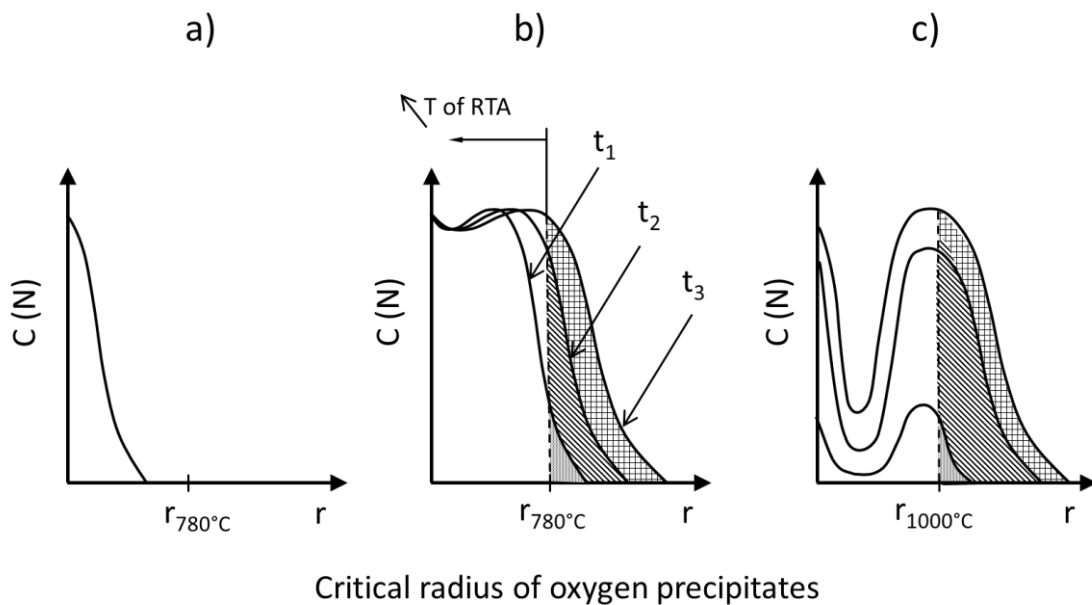


Figure 27: Schematic view of the size distribution of oxygen precipitates compared to the critical size of the precipitates: in as-grown sample (a), after nucleation at 450 °C or 650 °C for three different times (pattern fill indicates subsequent annealing at 780 °C) (b), after stabilization at 780 °C for 3 h (pattern fill indicates subsequent annealing at 1000 °C) (c).

In the samples pre-treated by RTA at temperatures of 1200 °C and above, the BMD density increases very fast. This can be explained by the fact that the critical radius decreases with increasing vacancy concentration as it was shown in Fig. 9.

The dependencies of the BMD density the nucleation times at 800 °C and 1000 °C are similar. The time “0” is the same for both temperatures. The BMD density for time “0” is increasing with increasing temperature of the RTA pre-treatment. This is due to the decrease of the critical radius with increasing concentration of vacancies. It is interesting that with a high vacancy supersaturation the critical radius can be reduced so that the very small oxygen precipitates will survive the anneal at 1000 °C as shown in Fig. 28 (a). The decrease of the vacancy concentration results in a rapid drop of the

BMD density because the critical radius is increasing and the concentration of oxygen precipitates decreases rapidly.

The jump of the BMD density between the nucleation times “0” and 1 h in the samples annealed at 800 °C appears because of a lower critical radius at 800 °C compared to 1000 °C. Annealing at 800 °C for 1 h is sufficient to increase the critical size of most of the precipitates to a size which survives the growth annealing at 1000 °C as can be seen in Fig 28 (b).

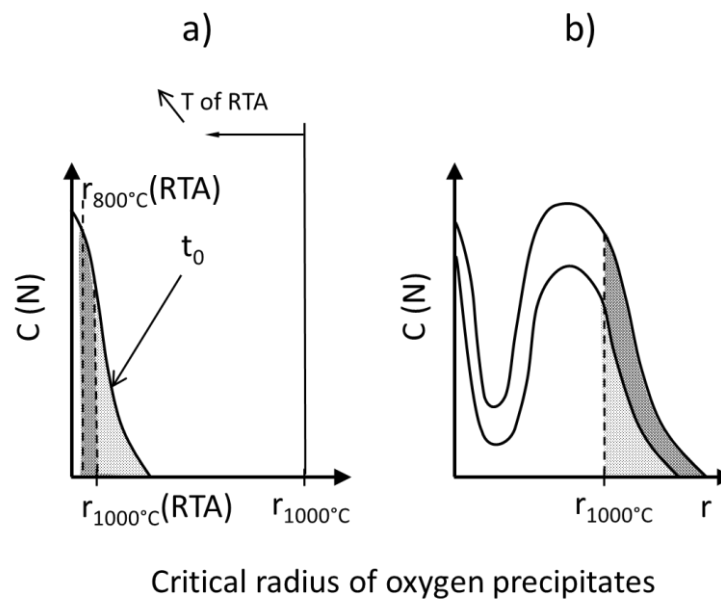


Figure 28: Schematic view of the size distribution of oxygen precipitates compared to the critical size of the precipitates which decreased in consequence of the vacancy supersaturation introduced by RTA: in as-grown sample (pattern fill indicates subsequent annealing at 800 °C or 1000 °C) (a), after annealing at 800 °C or 1000 °C for few hours (pattern fill indicates subsequent annealing at 1000 °C) (b).

Vacancy dependent nucleation curves

The peaks in Fig. 25 can be explained assuming three types of nucleation centers, considering the shape of the nucleation curve as the sum of three individual curves. In this approach, the measured BMD densities were divided by the annealing time giving the average nucleation rate.

In order to simulate the two peaks at 450 °C and at 650 °C, the coherent oxygen mono-layers ((O_i)₂-p1) and oxygen double-layers ((O_i)₂-p2) the so-called seed oxides were used [Kis08]. These nuclei are circular plates which also can be regarded as an intrinsic loop with the displacement vector *b*, which can be obtained from the difference

of the lattice constants $a_{Si} - a_{Seed}$. The agglomeration of interstitial oxygen atoms in single-layer and double-layer plates is energetically favorable in terms of the formation energy compared to incoherent nuclei [Kis08a]. The structure of $(O_i)_2$ -p1 and $(O_i)_2$ -p2, shown in Figs. 29 and 30, respectively, was modeled by ab initio calculation.

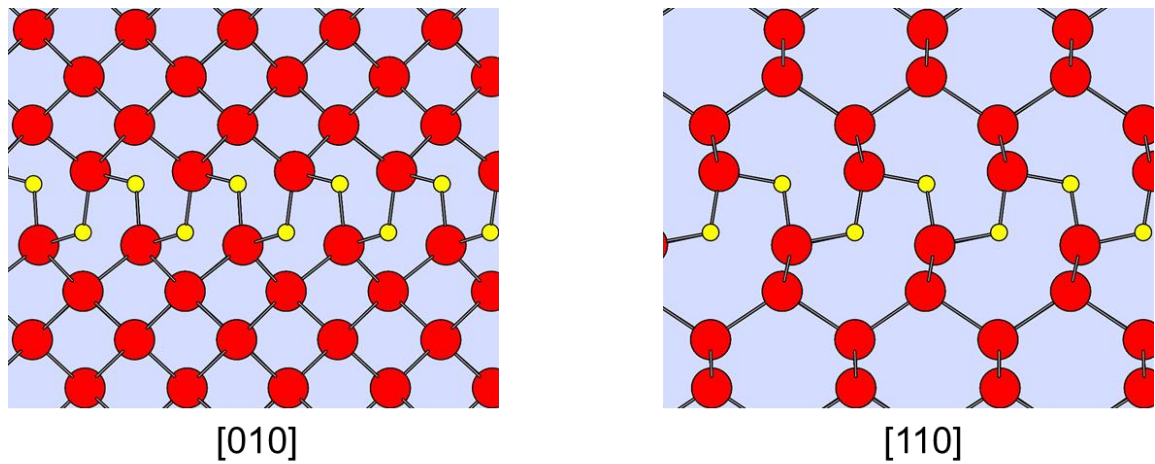


Figure 29: Single layer $(O_i)_2$ -p1 (001) platelet [Kis08b].

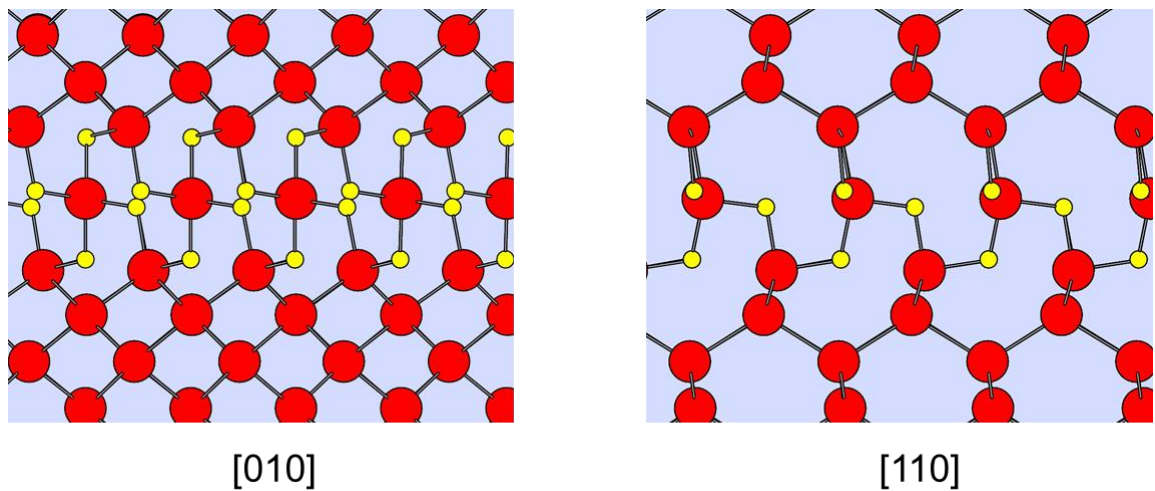


Figure 30: Double plane $(O_i)_2$ -p2 (001) platelet [Kis08b].

For modeling of the nucleation curves of $(O_i)_2$ -p1 and $(O_i)_2$ -p2, the classical nucleation theory presented in chapter 2.3.1 was applied. The total free energy and its contribution can be written now as follows [Kis08a]:

$$\Delta G^{plate} = -\Delta G_v + \Delta G_\sigma^{plate} + \Delta G_\varepsilon^{plate} \quad \text{with} \quad (37)$$

$$\Delta G_v = n \cdot k_B \cdot T \cdot \ln \left[\left(\frac{C_{O_i}}{C_{O_i}^{eq}} \right) \left(\frac{C_v}{C_v^{eq}} \right)^\gamma \right] \quad \text{and} \quad (38)$$

$$\Delta G_\sigma^{plate} = \left(\frac{\Omega_p \cdot 2n}{x} \right) \cdot \sigma \quad \text{and} \quad (39)$$

$$\Delta G_\varepsilon^{plate} = \frac{1}{8\pi \cdot (1-\nu)} \cdot \ln \left(\frac{64 \cdot n \cdot \Omega_p}{x \cdot \pi \cdot b^2 \cdot e^2} \right) \cdot \mu \cdot b^2 \cdot \sqrt{\frac{4\pi \cdot n \cdot \Omega_p}{x}}. \quad (40)$$

In the equation of the free energy of formation ΔG_v , the supersaturation of vacancies amounts 1. The surface needed for the calculation of the strain energy ΔG_σ^{plate} in this case is twice the area of the circular plate. The strain energy $\Delta G_\varepsilon^{plate}$, according to Ref. [Hu86a] can be calculated as the strain energy of a dislocation loop with the Burgers vector b . The Poisson's factor ν and the shear module of silicon μ are 0.28 and 6.41×10^{10} Pa, respectively [Wor65, Van02]. Setting the first derivative $d\Delta G/dn$ to zero, the critical number of oxygen atoms in a critical nucleus can be obtained. This is used for the calculation of the nucleation rate J_{plate} of coherent mono-layered and double-layered nuclei according to following equation

$$J_{plate} = N_0 \cdot \exp \left(-\frac{\Delta G_{crit}}{k_B \cdot T} \right) \cdot C_{O_i} \cdot \left(\frac{2n_{crit} \cdot \Omega}{x} \right) \cdot D_{O_i} \cdot d^{-1} \cdot Z \quad (41)$$

In order to simulate the third peak at 800 °C in the nucleation curve, the coherent mono-layered VO₂ agglomerates consisting of, so-called seed-SiO was used. The structure of these nucleation centers was also modeled by ab initio calculation. The atomistic view of seed-SiO is shown in Fig. 31.

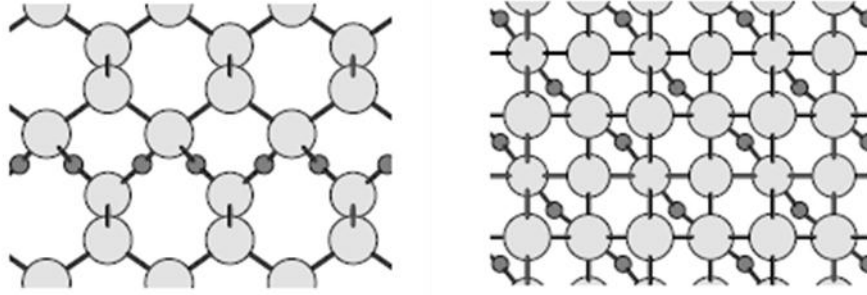


Figure 31: Coherent mono-layered VO₂ agglomerates - seed-SiO [Kis08a].

The parameters used for the simulation of the nucleation rate of the plate-like nuclei are included in Tab. 8. The surface energies σ were adjusted to get the best fit of the nucleation curves to the experimental data. Because the peaks at 450 °C and at 650 °C are located in the range of enhanced diffusivity of interstitial oxygen, for simulation of their nucleation rates the effective diffusivity according to Ref. [Tak98] was used whereas for the peak at 800 °C the normal diffusivity from Ref. [Mik86] was applied. The enhanced diffusivity leads to broader peaks and better fit of the simulated curves to the experimental data. Moreover, by varying the density of the nucleation sites N_0 , the height of the nucleation curves was adjusted to the experimental data. Please note that in Eqs. 38 the term of vacancy supersaturation is used only for simulation the peak at 800 °C.

TABLE 8. Parameters used for modeling coherent nucleation of plate-like nuclei.

Type of nucleus	Ω (cm ⁻²)	b (cm)	x	γ	σ (eV/cm ²)
(O _i) ₂ -p1	7.23×10^{-16}	4.70×10^{-9}	1	0	4.30×10^{14}
(O _i) ₂ -p2	7.23×10^{-16}	1.03×10^{-8}	2	0	4.20×10^{14}
(VO ₂)-(seed-SiO)	7.23×10^{-16}	7.05×10^{-9}	1	0.5	3.80×10^{14}

In Figs. 32 and 33, the results of the simulated nucleation curves are shown. In order to fit simulated nucleation rates to the experimental nucleation rates obtained from the BMD measurements, the simulated nucleation rates of the three types of nuclei were added forming one solid line. Fig. 32 presents nucleation curves for three peaks fitted to the experimental data obtained on the samples pre-treated by RTA at 1250 °C, 1225 °C, and 1200 °C and subsequently annealed at different temperatures for 1, 4, 8, and 16 h. The best fit was achieved for the peak at 800 °C almost for all presented experimental

data. The peaks at 450 °C and at 650 °C are well adjusted to the data of samples pre-treated by RTA at 1200 °C. At higher temperature of RTA pre-treatment, the space between the peaks was not sufficiently fulfilled. The “background” is assumed to be caused by a high density of as-grown nuclei which survived due to a decrease of the critical radius as the result of the high temperature of the RTA pre-treatment. For decreasing vacancy supersaturation by decreasing temperature of the RTA pre-treatment below 1200 °C, the “background” vanishes as shown in Fig. 33. The peak at 800 °C cannot be simulated because of the very low nucleation rate in the samples with low vacancy supersaturation. Therefore, only the simulations of the peaks at 450 °C and at 650 °C are shown in Fig. 33. The right peak in the simulated curve of the nucleation rate is well fitted to the experimental data. The left peak has a milder slope towards lower temperatures compared to experimental data. This is due to the application of effective diffusivities for all data even for temperatures lower than 400 °C. If we would use the normal diffusivity at 400 °C the simulation would fit much better at this temperature.

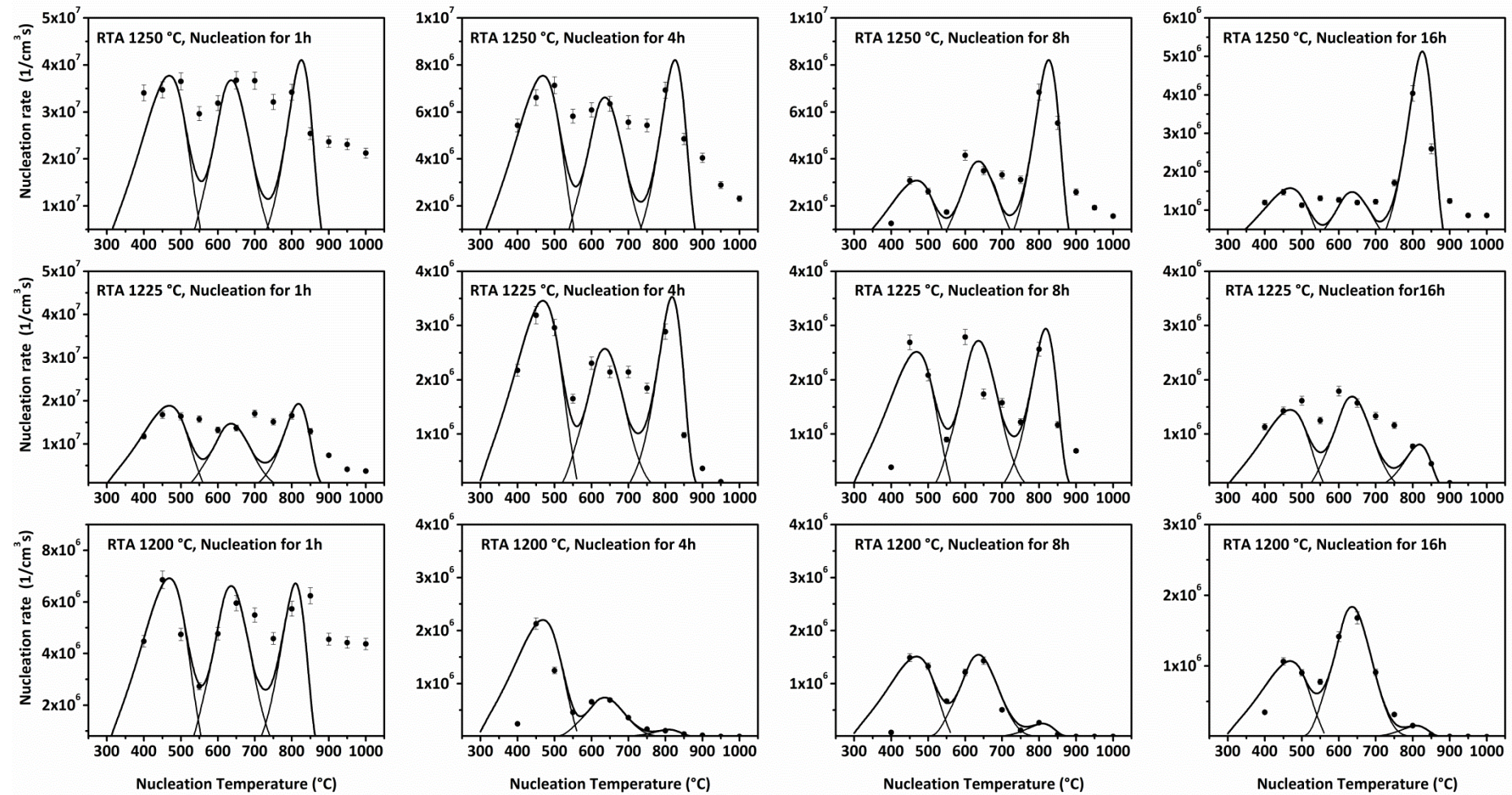


Figure 32: Comparison of experimentally obtained nucleation rates (data points) and simulated nucleation rates (full lines).

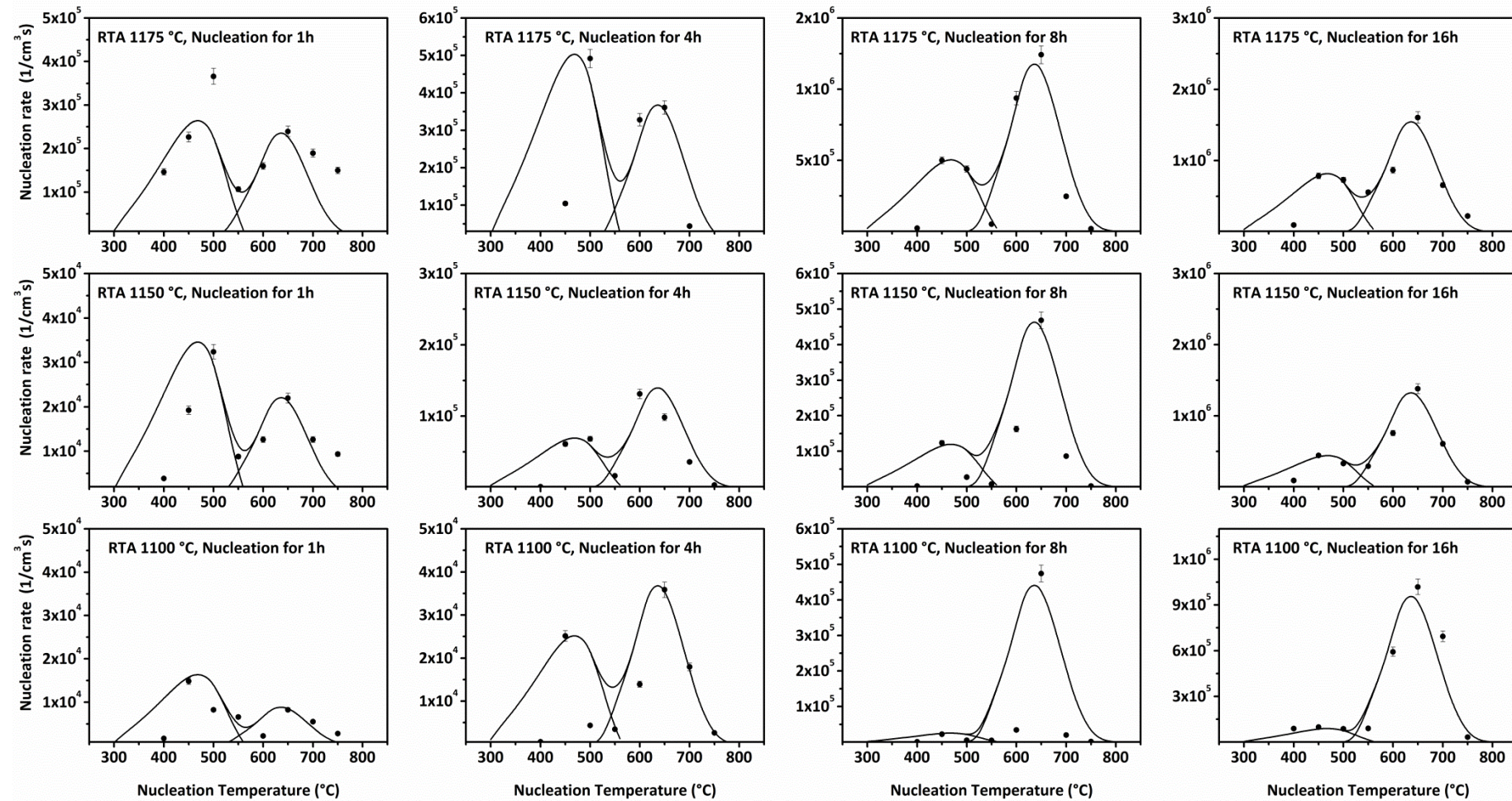


Figure 33: Comparison of experimentally obtained nucleation rates (same data points) and simulated nucleation rates (full lines).

6.1.4. Conclusions

In this chapter, the results of the nucleation experiments carried out on the samples with defined vacancy supersaturation were presented. From these results, the following conclusions can be drawn:

1. The BMD density increases with increasing vacancy concentration at all investigated temperatures. Three peaks were observed in the nucleation curves wherein two of them at 450 °C and 650 °C are also present in samples without vacancy supersaturation. The peak at 800 °C appears only in the samples with high vacancy supersaturation.
2. The nucleation kinetics at 450 °C, 650 °C, 800 °C, and at 1000 °C in the vacancy supersaturated samples can be explained considering influence of vacancies on the critical radius, which decreases with increasing vacancy supersaturation, and considering the size distribution of oxygen precipitates.
3. The three peaks in the vacancy dependent nucleation curves can be explained assuming the nucleation of coherent plate-like nuclei consisting of mono-layers ((O_i)₂-p1) and double-layers ((O_i)₂-p2) for the peaks at 450 °C and at 650 °C and mono-layered VO₂ layers for the peak at 800 °C.

6.2. Influence of vacancies on the morphology and size of oxygen precipitates investigated by STEM

6.2.1. Introduction

The high BMD density between 800 °C and 1000 °C caused by a high vacancy concentration provides a good opportunity to investigate the morphology and the size of oxygen precipitates by means of STEM. Especially in the samples pre-treated by RTA at temperatures above 1200 °C, the amount of precipitates is high enough that they can be found by STEM after a relatively short time of annealing. Until now, only results of samples annealed for very long time but without increased vacancy supersaturation were published in the literature [Pon89, Has92, Sue93]. In this chapter, the influence of vacancies introduced by RTA on the morphology and the size of oxygen precipitates in the temperature range between 800 °C and 1000 °C are shown. A second interesting issue addressed in this chapter is the influence of the vacancy concentration on the morphology and the size of oxygen precipitates. The final part of this chapter is concerned with the getter sites for Cu atoms. Special attention is paid to oxygen precipitates. Their capability to getter metal atoms is discussed since decades [Sue06, Web02, Ist02, She94]. Although, defects like dislocations and stacking faults are well known as a getter sites for metals there is no direct proof regarding the getting of metals by oxygen precipitates.

6.2.2. Geometry of STEM investigations

As it was described in chapter 2.6, the morphologies of oxygen precipitates which can be found between 800 °C and 1000 °C are plate-like or octahedral. In most of the cases in this work, the samples were investigated in the cross-sectional view. This means that for (110) foils the scans were taken on the (110) plane. During the analysis of the morphology of the oxygen precipitates in this view, plate-like precipitates appear in the same way like octahedral precipitates. Therefore, in order to distinguish between plate-like and octahedral precipitates the following additional features were used.

The plate-like precipitates can occur in the silicon crystal in three different positions while the octahedral precipitates can be situated in the silicon bulk only in one position. In the (001) view, one can see square shaped precipitates surrounded by {110} planes

and two sets of thin line-shaped precipitates located perpendicularly to each other and tilted to the $\{110\}$ planes by an angle of 45° as demonstrated in Fig. 34 (left). These shapes belong to plate-like precipitates. In the same view, the projection of octahedral precipitates takes the shape of a square surrounded by $\langle 110 \rangle$ edges. The possible projections of plate-like and octahedral precipitates on the (110) plane are demonstrated in Fig. 34 (right). In the (110) view, the octahedral precipitates appears like a rhombus bound by $\{111\}$ planes with an angle of 70.53° . Unfortunately, the projection of plate-like precipitates lying on (100) , (010) , $(\bar{1}00)$, or $(0\bar{1}0)$ planes are equal to the projection of octahedral precipitates on the (110) plane. The plate-like precipitates lying on the (001) plane in the (110) view can be observed as a thin line.

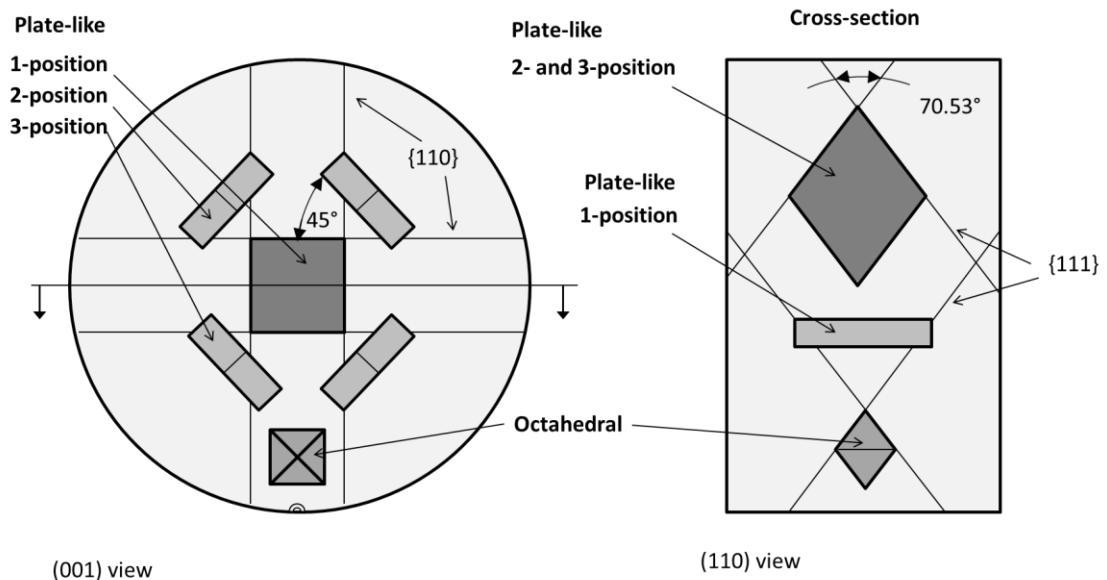


Figure 34: View of plate-like and octahedral precipitates on (100) and (110) surfaces.

A characteristic STEM image of a plate-like precipitate in the (110) view having a rhombus-like projected shape is shown in Fig. 35 (left). Some of the plate-like precipitates are seen only partially, mainly at the edge of the STEM sample where the foil thickness is below 100 nm. Such a view is observed if a part of the precipitate was cut off during the sample preparation. An example of such a precipitate is shown in Fig. 35 (right). During the investigation, precipitates which look like a mirror image of the one presented in Fig. 35 (right) were also found. Because the projection of the cut off octahedral precipitates cannot appear in this way, this is one way to distinguish between the octahedral and the plate-like precipitates. The octahedral precipitates are

also smaller than the plate-like precipitates and despite of the small size they are characterized by sharp edges.

In Figs 36 and 37, two other ways how to distinguish between a plate-like and octahedral precipitate are demonstrated. In case of the plate-like precipitates, which look like octahedral precipitates one can tilt the sample. The shape of the precipitate will change from rhombus to square or rhombus to straight line depending on the direction of the rotation. The images of the precipitate in the tilted sample are usually less sharp than in the untitled sample due to difficulties with focusing as shown in Fig. 36. If the plate-like and the octahedral precipitates are close to each other, one can make an EDX scan. In this case, the signal of oxygen from the octahedral precipitates should be much stronger than the signal of oxygen from the plate-like precipitates as can be seen in Fig. 37.

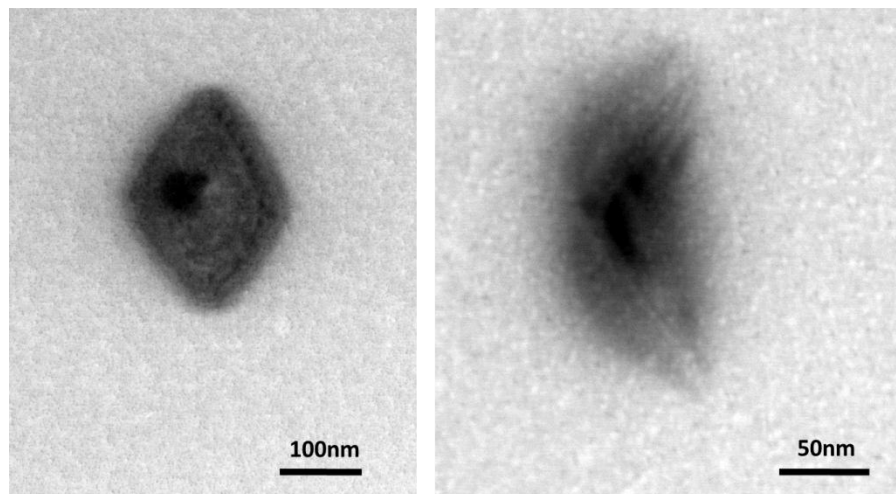


Figure 35: Plate-like precipitates in the (110) view: plate-like precipitate – whole defect (left), plate-like precipitate partially cut out during sample preparation (right).

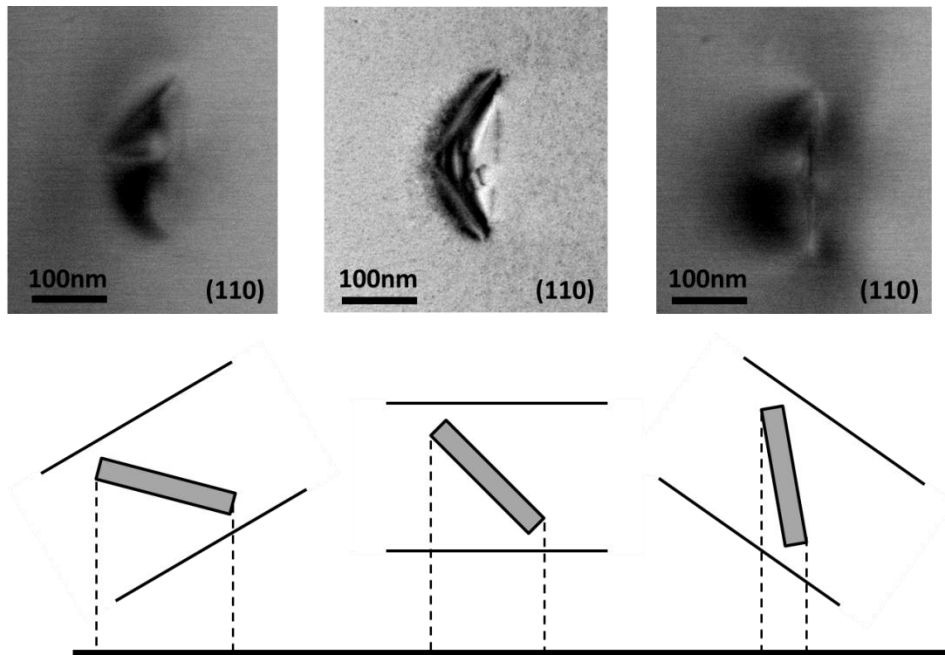


Figure 36: Rotation of plate-like precipitate by an angle of about 30° in two opposite directions (left and right), unrotated sample (middle).

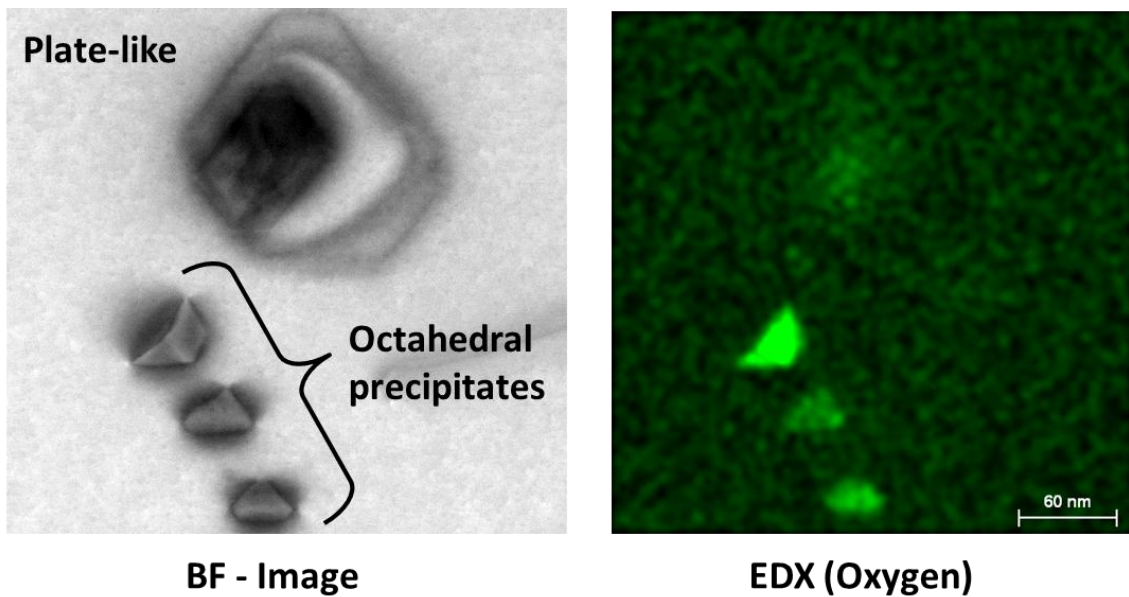


Figure 37: Method to distinguish between octahedral and plate-like precipitates in the (110) view by EDX scanning: plate-like and octahedral precipitates observed by the BF detector (left), plate-like and octahedral precipitates observed by the EDX detector.

6.2.3. Experimental details

In order to investigate the influence of vacancies, annealing temperatures, and times on the morphology of oxygen precipitates, two sets of heat treatments were used. The specification of the samples was the same as for the nucleation experiments.

In the first set, the samples were pre-treated by RTA at 1250 °C for 30 s in Ar atmosphere containing 1000 ppm of oxygen and annealed at 800 °C, 900 °C, and 1000 °C for 8 h, 32 h, and 64 h in N₂. In the second set, the samples were pre-treated by RTA at 1250°C, 1225°C, 1200 °C, and 1175 °C for 30 s and annealed at 800 °C for 64 h.

The next part of STEM investigation was focused on the investigation of getter sites for Cu atoms. For this experiment, tree samples were used. The first sample was cut out from a high O_i wafer. This sample was pre-treated by RTA at 1250 °C for 30 s and annealed at 800 °C for 32 h and at 1000 °C for 16 h in N₂. Then, the sample was contaminated with Cu with a concentration of $1.0 \times 10^{13} \text{ cm}^{-2}$ and annealed at 1000 °C for 10 min.

The two next samples were cut out from a low O_i wafers. First the sample was pre-treated by RTA at 1250 °C for 30 s and annealed at 1000 °C for 8 h in N₂. Then, the sample was contaminated with Cu by scratching with a Cu wire at the back surface and annealed at 900 °C for 10 min. The concentration of Cu in these samples reached the solubility limit of Cu at 900 °C ($2.2 \times 10^{17} \text{ cm}^{-3}$ [Web83]). The second sample was pre-treated by RTA at 1175 °C for 30 s and annealed at 800 °C for 64 h in N₂ and then contaminated with high concentration of Cu.

6.2.4. Results and discussion

The STEM investigations carried out on the samples pre-treated by RTA at 1250 °C and subsequently annealed in the temperature range between 800 °C and 1000 °C showed that the morphology of the oxygen precipitates strongly depends on the annealing temperature. After annealing at 800 °C, the oxygen precipitates appear mainly in the form of **two (2D) or three (3D) dimensional dendritic plate-like defects**. Annealing at higher temperatures (900 °C and above) results in a **plate-like** or an **octahedral** morphology of the oxygen precipitates. Moreover, large **dendritic plate-like** precipitates can be found after annealing at temperatures of 900 °C and 1000 °C. All the forms of the oxygen precipitates found at each of the mentioned temperature are described in detail below.

Oxygen precipitates after annealing at 800 °C

At this temperature, the prolonged annealing of silicon wafers pre-treated by RTA leads to the formation of three dimensional dendritic oxygen precipitates for which the two dimensional dendritic form lying on one of the {001} planes is a base as shown in Fig. 38. This form has the major branches along $\langle 110 \rangle$ directions and the minor branches along $\langle 001 \rangle$, $\langle 012 \rangle$, and $\langle 013 \rangle$ directions. The 3D dendrite consists of two perpendicular 2D dendritic plates. Such a 3D dendrite as it is observed in [110] is shown in Fig. 39 (right). The directions in figure are ordered with respect to the directions of the branches of the precipitate while the angles are attributed to the angles of the projection of the dendritic branches on the (110) plane. The analysis of the spatial form of 3D dendrites was deduced based on the several EDX images. Fig. 39 (left) shows an EDX image of a dendritic precipitate with all possible branches. The strong signal of oxygen in the middle of precipitate belongs to the 2D plate lying perpendicular to the image plane.

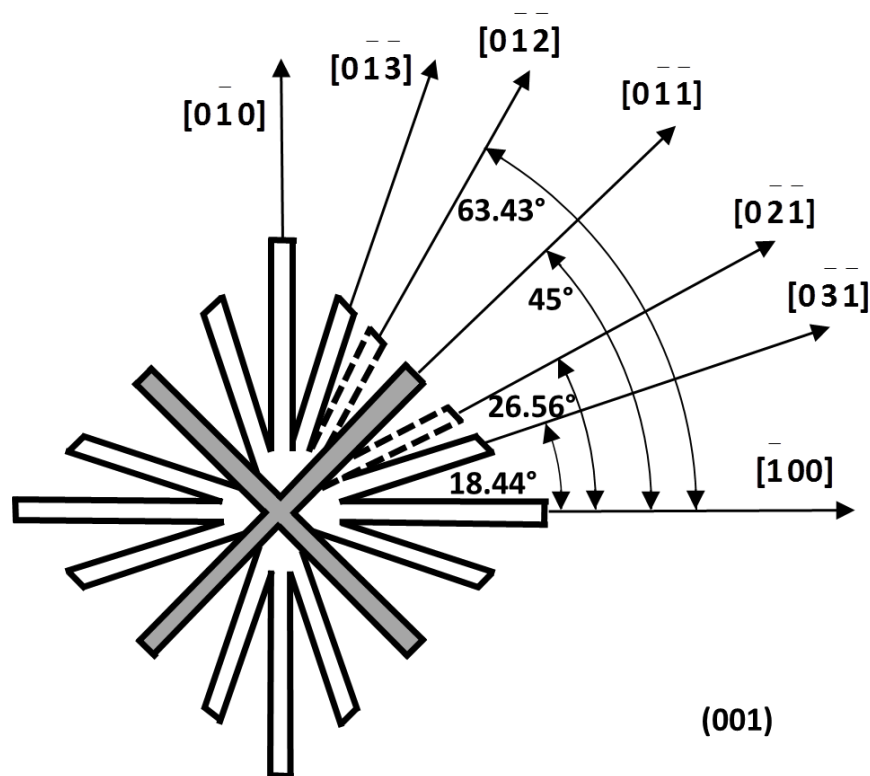


Figure 38: Basic form of dendritic precipitates.

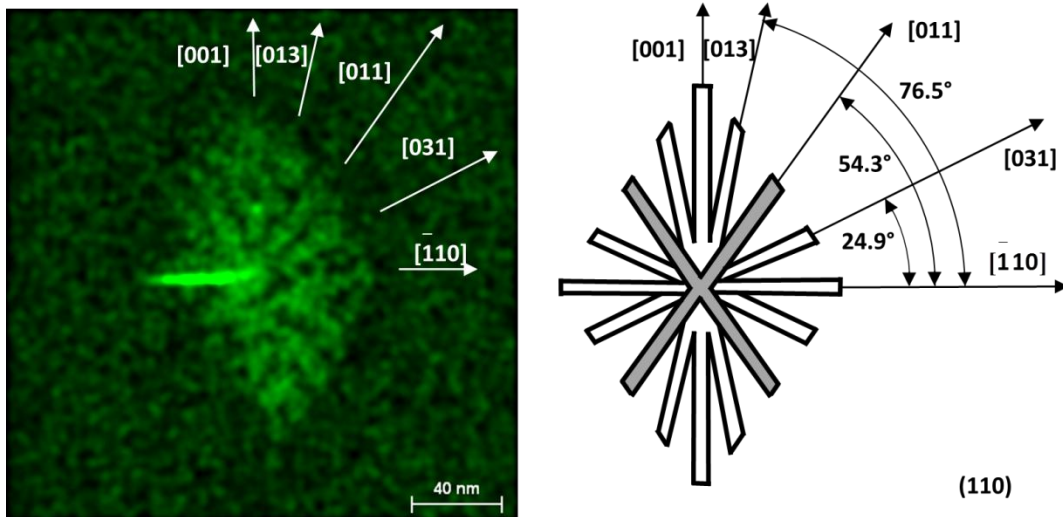


Figure 39: Three dimensional (3D) dendritic plate-like: observed by EDX (left) in a sample pre-treated by RTA at 1225 °C for 30 s and annealed at 800 °C for 64 h in N₂, model retrospect form the EDX images (right).

A clear dendritic form of the oxygen precipitates can be observed in the samples after annealing at 800 °C at least for 64 h. For shorter times of annealing, the analysis of the dendrites becomes difficult because they are too small. After 8 h of annealing at 800 °C, the average size of the oxygen precipitates equals about 10 nm. Due to this, the EDX investigation is useless because the intensity of the oxygen in the precipitate is not high enough. Fig. 40 shows a typical image of the oxygen precipitates observed in the sample pre-treated by RTA and annealed at 800 °C for 8 h. Although, the image of the oxygen precipitate is quite distinct, the morphology of the oxygen precipitate cannot be determined. Clear branches of the oxygen precipitates can be seen after annealing of the sample for 32 h as can be seen in Fig. 41 (bottom). The oxygen precipitate presented here is an example of a typical oxygen precipitate observed in the silicon wafer after annealing at 800 °C for 32 h. Fig. 41 (top) presents also two 2D dendrites crossing each other observed in the [110] view.

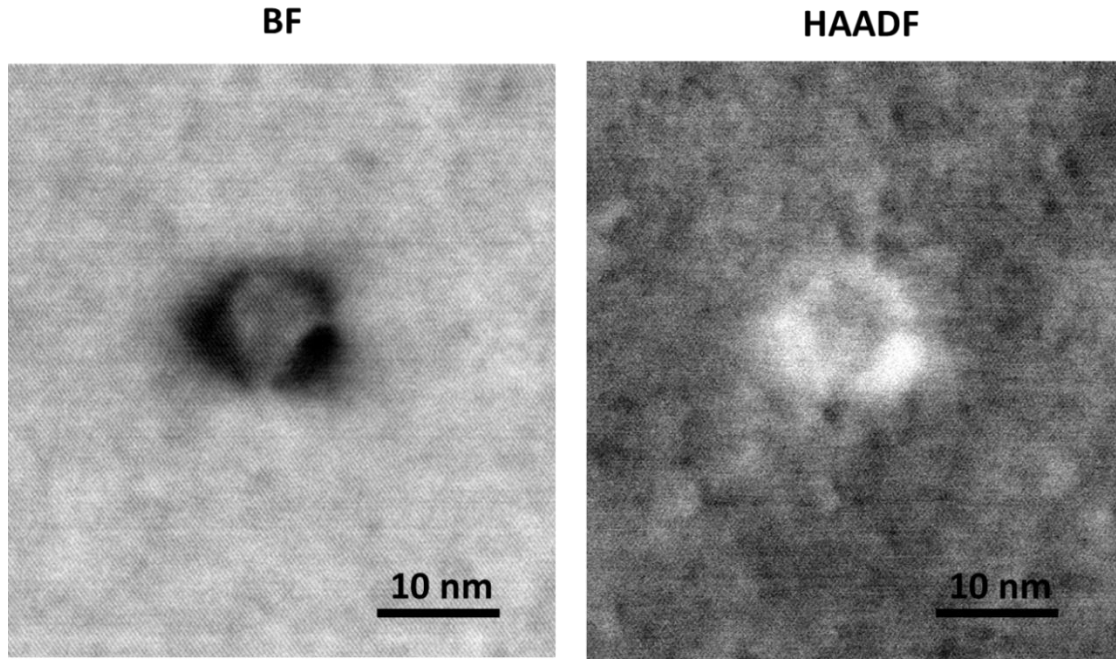


Figure 40: Small oxygen precipitate observed in the sample pre-treated by RTA at 1250 °C for 30 s and annealed at 800 °C for 8 h in N₂

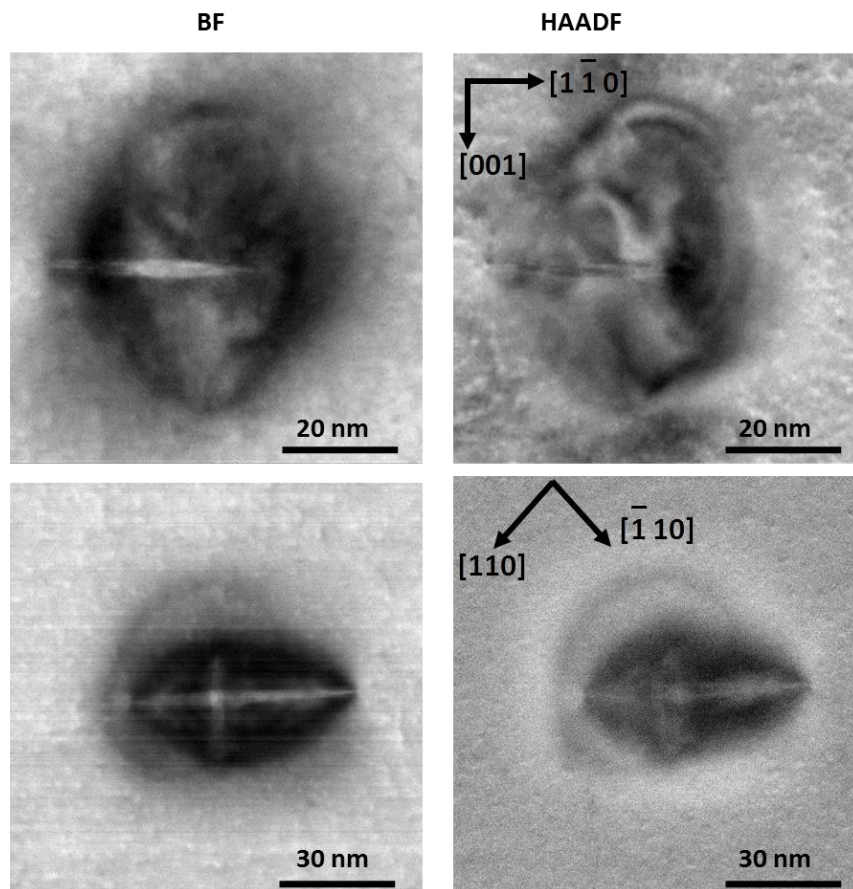


Figure 41: Three (3D) dimensional dendritic precipitates in the sample pre-treated by RTA at 1250 °C for 30 s and annealed at 800 °C for 32 h in N₂: precipitate observed in [110] view (top images), precipitate observed in [001] view (bottom images).

Until now dendritic precipitates were observed only at 1000 °C in the form of large plate-like precipitates [Aoki93, Fuj97]. According to the literature, the formation of dendritic precipitates occurs under high supersaturation in contrast to the octahedral precipitates which grow under low supersaturation. The 3D dendrites reported in this work are much smaller than the dendrites observed at 1000 °C and their branches are much thinner. However, their formation should be based on the same principle like the formation of large dendritic plate-like precipitates. According to Ref. [Zio11] very high supersaturation of solute is a reason of the formation of thin branches in dendrites. The formation of 3D dendrites at 800 °C is associated with a high supersaturation of oxygen what can explain the thin branches of the 3D dendrites.

Oxygen precipitates at 900 °C

The increase of the annealing temperature to 900 °C changes the morphology of the oxygen precipitates. Although, 3D dendritic precipitates are still observed, their density is much lower than at 800 °C and the dominating morphology of the precipitates is now the plate-like form. The plate-like precipitates are often associated with dislocation loops. At this temperature, octahedral precipitates also appear. They are much smaller than the plate-like precipitates. In many cases, octahedral precipitates nucleate at dislocations originated from the plate-like precipitates. Just some of the plate-like precipitates have a dendritic structure.

Fig. 42 shows typical oxygen precipitates observed after annealing at 900 °C. Figs. 42 (a) and (b) present plate-like precipitates located in the crystal in different orientations. The dislocation loops and the octahedral precipitates nucleated at these loops are typical defects observed in the samples annealed at 900 °C for 32 h as shown in Fig. 42 (c). Moreover, plate-like precipitates with dendritic branches can be found as shown in Fig. 42 (d). This type of precipitates was reported by Aoki and called the starfish-like dendritic oxides [Aoki93]. A similar defect appears also in the samples after 64 h of annealing. According to Aoki, these defects are formed during annealing at 1000 °C. The reason why the dendrites in our case occur at lower temperature can be explained by the high supersaturation of vacancies increasing the growth rate of oxygen precipitates. As shown in Fig. 42, large plate-like precipitates and small octahedral precipitates (e) and precipitates with dislocation loops (f) are observed. The defect at the bottom of image (f) can be a 3D dendritic precipitate as indicated by the plate-like precipitate which is seen perpendicular to the image plane in the center of precipitate.

The presence of the plate-like precipitates at 900 °C is common but octahedral or polyhedral precipitates can be observed only under special conditions like very long annealing time and location in the wafer bulk. Sueoka et al observed polyhedral precipitates in a sample annealed at 900 °C for 700 h [Sue92]. Fujimori has found polyhedral precipitates already after 8 h of annealing at 900 °C but only in the denuded zone (DZ) area less than 10 µm below the surface [Fuj97]. He concluded that the polyhedral precipitates occur if the supersaturation of oxygen is low. The octahedral precipitates observed in this work occur in the bulk already after 8 h. With increasing time their concentration increases. The presence of octahedral precipitates in the samples annealed at 900 °C can be explained as follows. The high concentration of vacancies increases the nucleation rate of the oxygen precipitates. After a short time of annealing, a high concentration of plate-like precipitates is formed. Due to this, the supersaturation of oxygen rapidly decreases. The low supersaturation creates good conditions for the growth of octahedral precipitates, which nucleate at the dislocations formed during the growth of plate-like precipitates. Generally speaking, a high density of precipitates accelerates the formation of octahedral precipitates. A similar effect was observed by Hallberg et al. These authors investigated the influence of VO and VO₂ centers on the enhancement of the formation of oxygen precipitates by means of IR spectroscopy [Hal92]. In their as-grown sample without VO and VO₂ annealed at 900 °C, the IR absorption bands attributed to plate-like and spherical precipitates appeared after 30 h and 50 h, respectively. While in the sample with VO₂ electron irradiated at a dose of 10¹⁸ cm⁻², the absorption bands of plate-like and the spherical precipitates appeared after 25 h and 28 h, respectively. The formation time of spherical precipitates, which in reality are octahedral precipitates is significantly decreased in the VO₂ rich sample.

Oxygen precipitates at 1000 °C

At this temperature, the morphology of the oxygen precipitates is of the form of small octahedral precipitates or large plate-like precipitates. The plate-like precipitates are often associated with dislocation loops and punched out dislocation loops. Moreover, dendritic square plate-like precipitates with growth stripes between their branches can be observed.

Fig. 43 shows the typical oxygen precipitates observed in the sample after annealing at 1000 °C. Images (a), (b), and (c) in Fig. 43 show a large plate-like precipitate, a truncated octahedral precipitate, and an octahedral precipitate, respectively. At 1000 °C

also dendritically grown plate-like precipitates appear like the one in Fig. 43 (d). This type of dendrites was also found by Aoki [Aok93]. Aoki described these defects as a dendritic square-plate oxide with a starfish-shaped oxide inside that extends in the $\langle 110 \rangle$ direction. He also mentioned that the observed concentric circles are growth stripes. The author assumed that the growth stripes observed between the branches are formed in following way. The dendritic oxides produce strain due to volume expansion resulting from the precipitation. This strain generates rectangular dislocations between the dendritic branches. Interstitial oxygen is then aggregated at the dislocation. In order to check this hypothesis, an EDX investigation was carried out on this type of precipitates. Fig. 44 shows BF, HAADF, and EDX images of a large dendritically grown plate-like precipitate. The signal of the oxygen comes clearly from the main branches growing in $\langle 110 \rangle$ directions, but there is no signal at the site of the stripes. However, the HAADF image shows a clear material contrast of the stripes. Therefore, the presence of oxygen cannot be definitely excluded.

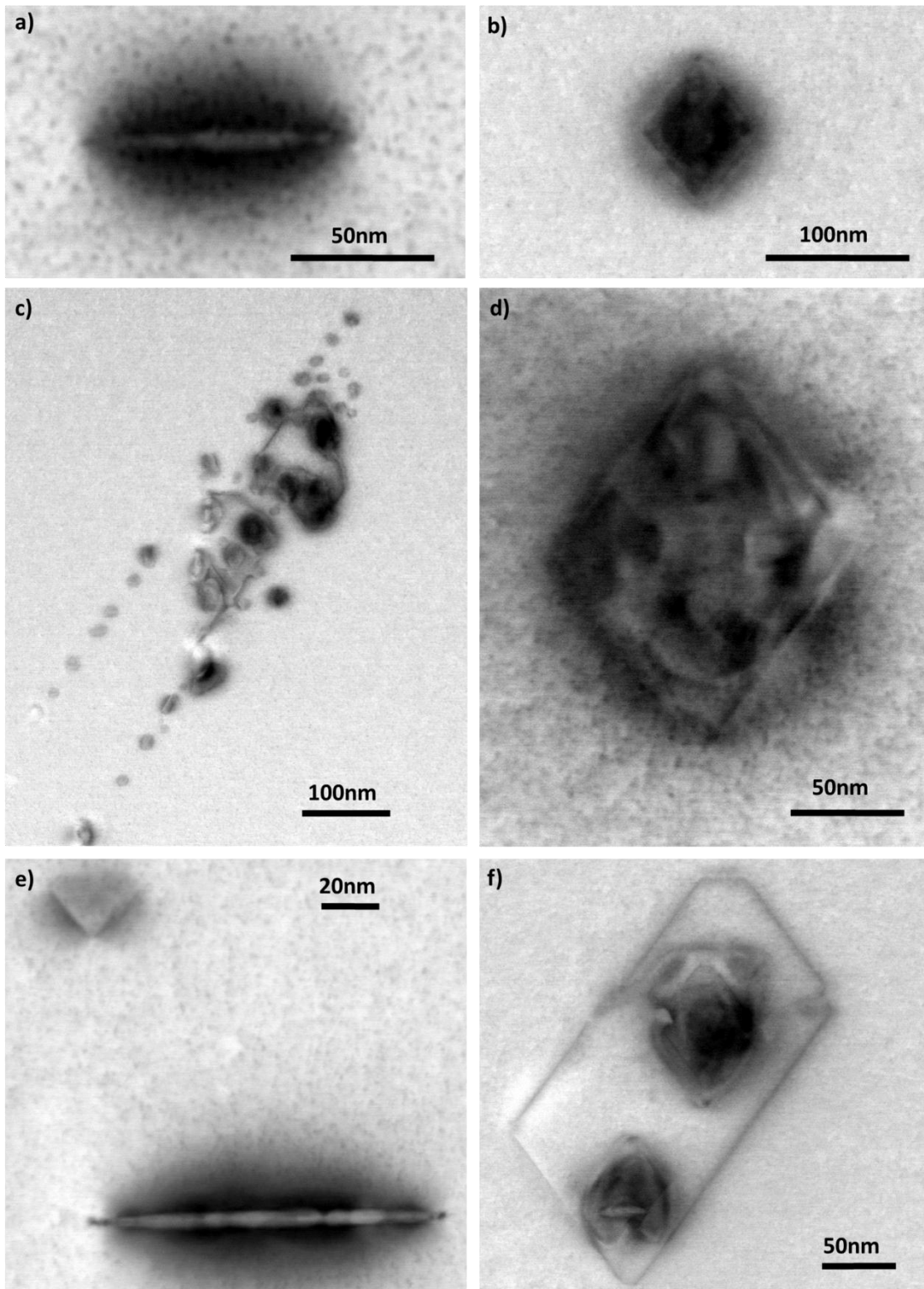


Figure 42: Oxygen precipitates observed in the samples pre-treated by RTA at 1250 °C and annealed at 900 °C: plate-like precipitates in the sample annealed for 8 h (a and b), dislocation loops and the octahedral precipitates nucleated at these loops in the samples annealed for 32 h (c), starfish-like dendritic oxygen precipitates in the sample annealed for 32 h (d), large plate-like precipitate and small octahedral precipitate in the sample annealed for 64 h (e) 3D dendrite with plate-like precipitate and dislocation loop in the sample annealed for 64 h (f).

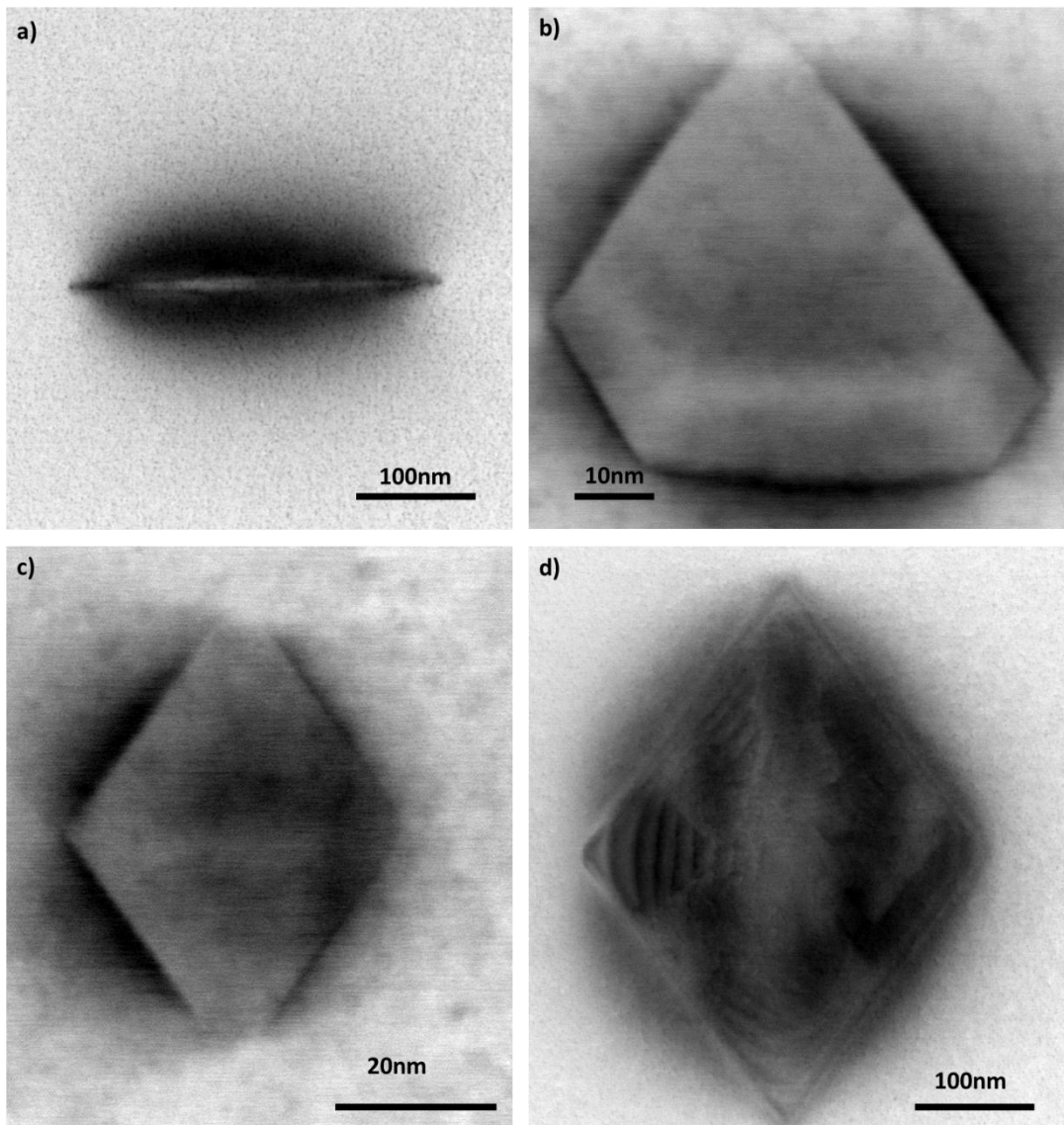


Figure 43: Oxygen precipitates observed in the samples pre-treated by RTA at 1250 °C and annealed at 1000 °C: plate-like precipitate in the sample annealed for 32 h (a), truncated octahedron in the sample annealed for 32 h (b), octahedral precipitate in the sample annealed for 64 h (c), large dendritically grown plate-like precipitates in the sample annealed for 32 h (d).

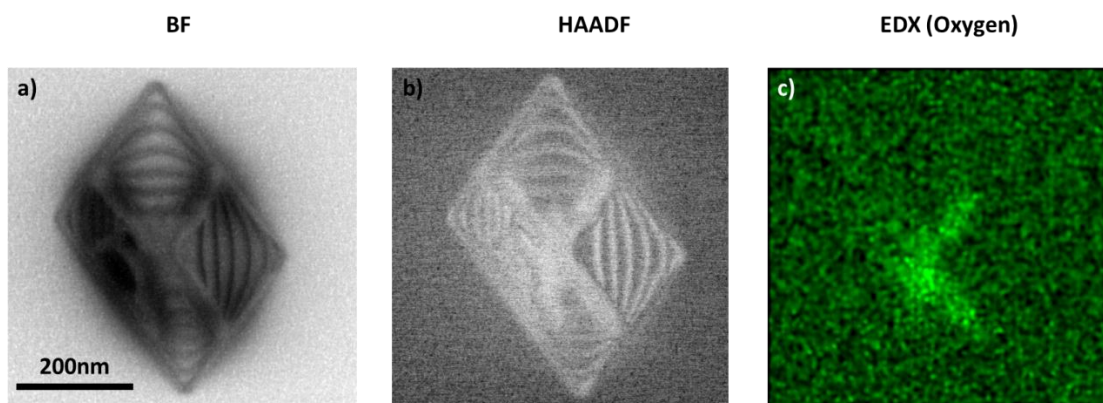


Figure 44: Large dendritically grown plate-like precipitate: STEM BF image (a), HAADF image (b) and EDX image (c).

Influence of the vacancy concentration on the morphology of oxygen precipitates

The STEM investigations carried out on the samples subjected to RTA pre-treatments in the temperature range between 1175 °C and 1250 °C followed by annealing at 800 °C for 64 h showed that the change of the temperature of the RTA does not influence the morphology of the oxygen precipitates. The morphology of the oxygen precipitates remains the same like the morphology observed in the sample pre-treated by RTA at 1250 °C and annealed at 800 °C for 64 h. This means that the oxygen precipitates have the form of 3D and 2D dendrites as shown in Fig. 45.

It was theoretically calculated that when a supersaturation of vacancies exists the spherical precipitates have a lower free energy than the plate-like precipitates. This means that under pre-existing supersaturation of vacancies, the morphology of precipitates should be spherical [Wan02]. However, if we consider vacancy concentration, size and density of oxygen precipitates, and the number of ejected silicon interstitial atoms per each oxygen atom attached to the precipitate, it becomes clear that the supersaturation of vacancies disappears very quickly. As the result, for precipitates having a few nm in size there is no supersaturation of vacancies in the bulk anymore and the spherical morphology of the precipitates is no longer favorable. The oxygen precipitates in the sample pre-treated by RTA at different temperatures and annealed at 800 °C for 64 h are of about 160 nm edge length. Also the density of precipitates is high and for an RTA pre-treatment at 1175 °C it exceeds $1 \times 10^{10} \text{ cm}^{-3}$. For such a large size and high density of precipitates, the pre-existing vacancy supersaturation should be fully compensated by the ejected silicon interstitial atoms.

However, a pre-existing supersaturation of vacancies could have an influence on the dendritic morphology of oxygen precipitates at 800 °C. If a vacancy supersaturation exists in the initial stage of the precipitate growth, the precipitates grow in the form of spheres instead of plate-like precipitates. A longer growth of oxygen precipitates in the form of sphere could be decisive for the formation of dendritic precipitates. In the sample without supersaturation of vacancies, the small spherical precipitates change their morphology very quickly into plate-like from in order to minimizing the surface energy at the beginning of the growth [Vor01, Sue03]. In case of vacancy supersaturation, the spherical form is kept longer. During spherical growth, a local perturbation at the interface of the spheres could cause the formation of many fronts of growth as shown in Fig. 46. Such a model of dendritic growth was described in Ref. [Woo73]. The parts of the nucleus which are more far away from the center will grow

faster than those parts of the interface being nearest to the center due to the gradient of oxygen supersaturation.

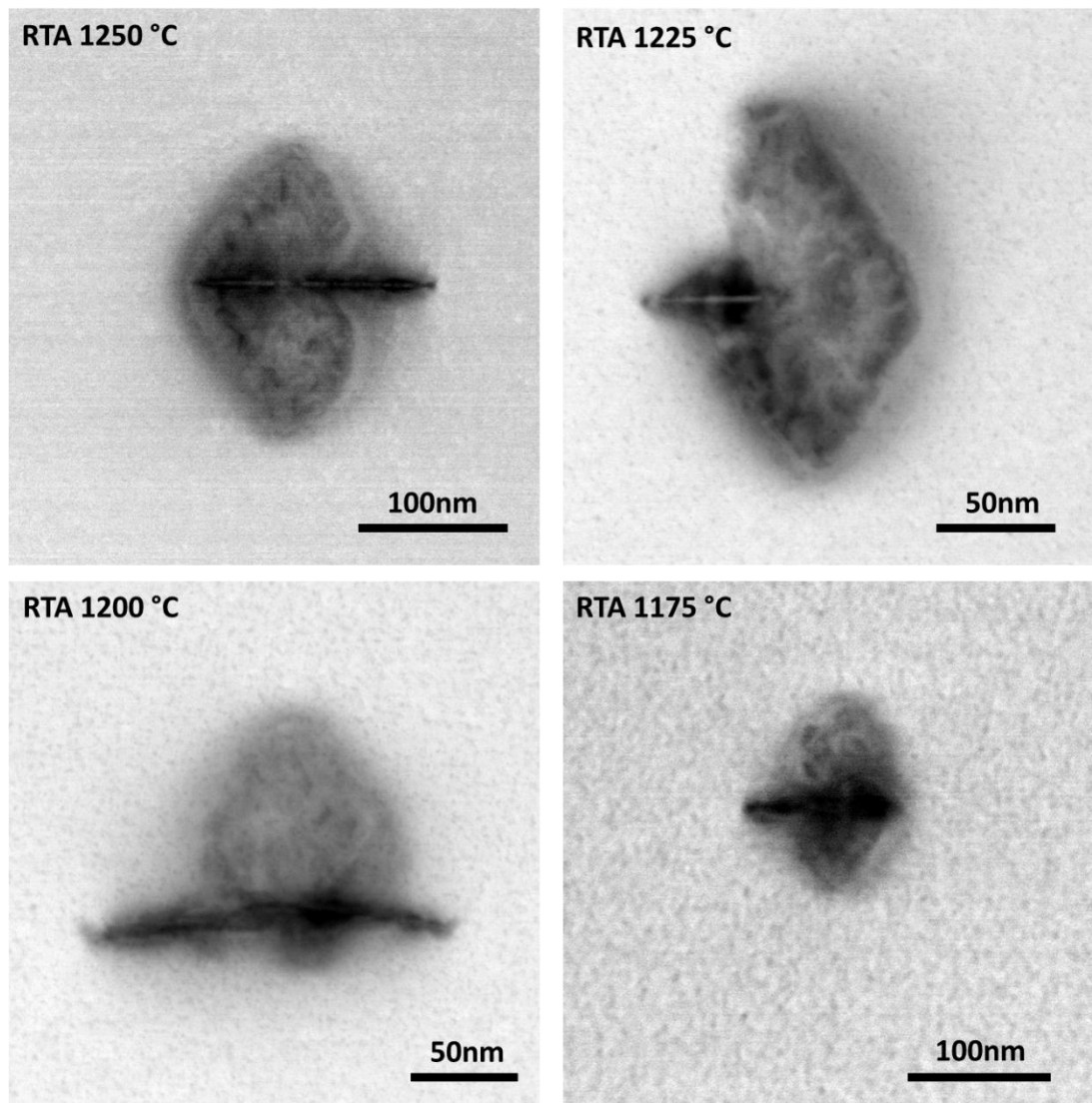


Figure 45: The 3D dendrites observed in the samples pre-treated by RTA at 1250 °C, 1225°C, 1200°C, and 1175°C followed by annealing at 800 °C for 64 h.

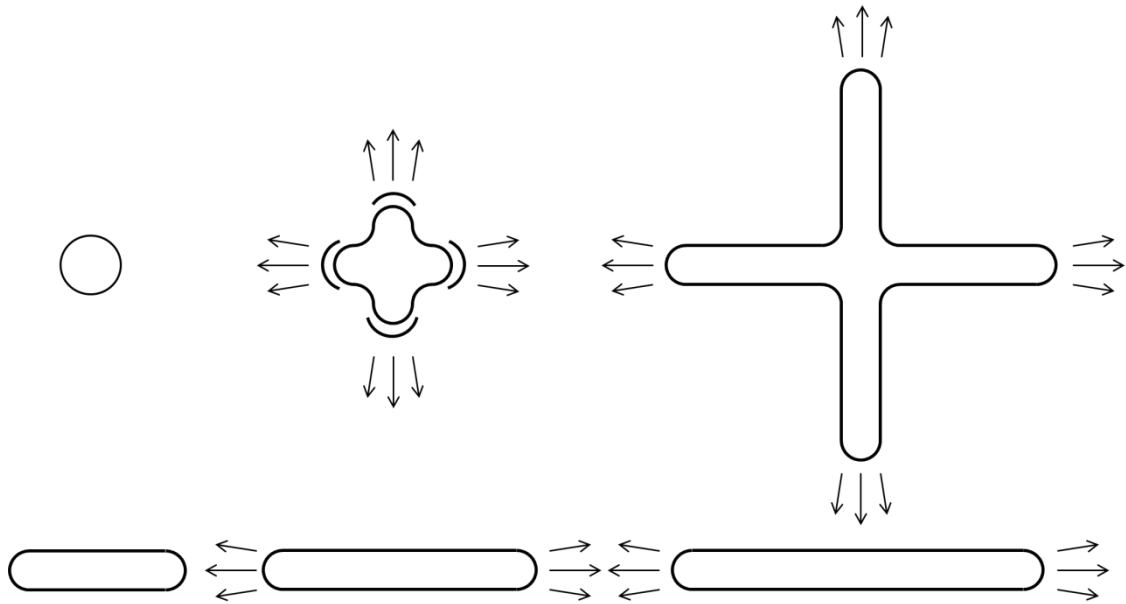


Figure 46: Growth fronts of formation of a spherical (top) and a plate-like precipitate (bottom).

Density and size of oxygen precipitates

The BMD density determined from the STEM images of the samples pre-treated by RTA at 1250 °C and annealed in the temperature range between 800 °C and 1000 °C for 8, 32, or 64 h was in the range between $4 \times 10^{11} \text{ cm}^{-3}$ and $2.5 \times 10^{12} \text{ cm}^{-3}$ as shown in Fig. 47 (left). For samples pre-treated by the RTA at different temperatures and annealed at 800 °C for 64 h, the BMD density increases exponentially with increasing temperature of the RTA pre-treatment as shown in Fig. 47 (right).

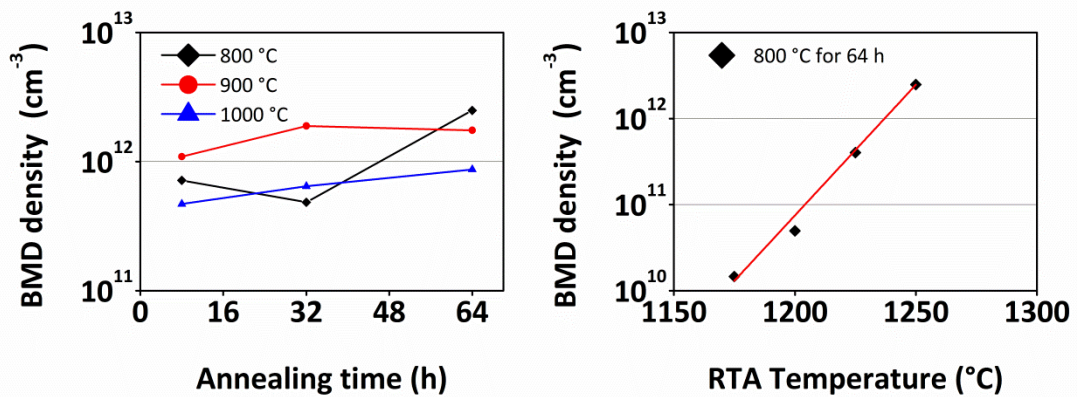


Figure 47: BMD density in samples pre-treated by RTA at 1250 °C and annealed at different temperature for various time (left), and in the samples pre-treated by RTA at different temperature and annealed at 800 °C for 64 h (right).

Fig. 48 shows the edge length of the 3D dendritic plate-like precipitates measured by STEM as a function of the annealing time at 800 °C. As shown in Fig. 48, the values of the length of the precipitates vary for different times of nucleation. It is clearly seen that the maximum length of the precipitates is increasing linearly with the time. This is characteristic for dendritic growth. From the slope, one can determine the growth rate. For annealing at 800 °C, it is 2.5 nm/h.

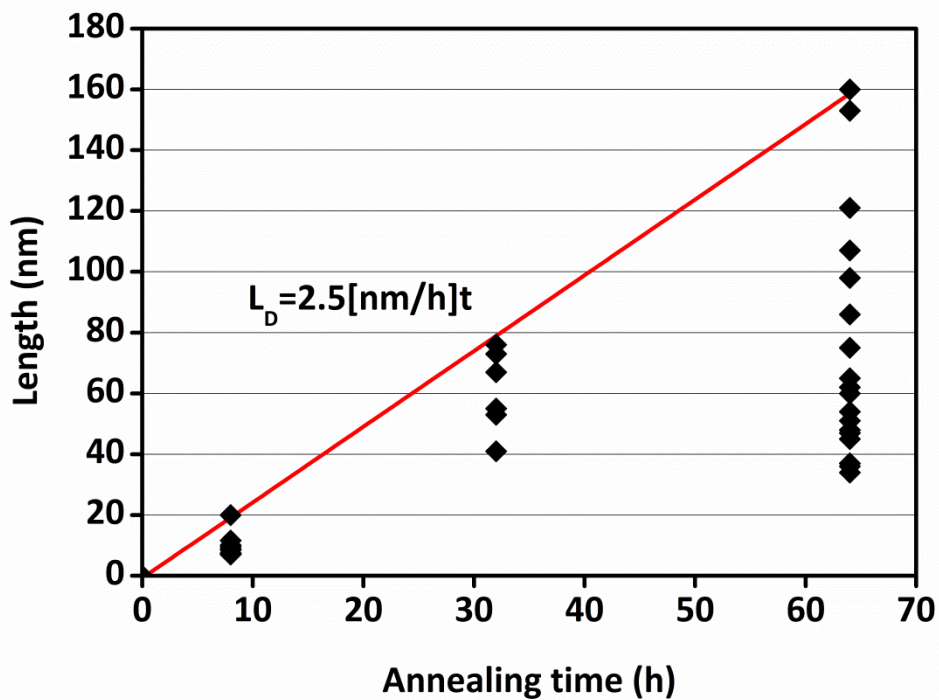


Figure 48: Edge length of the 3D dendritic plate-like precipitates shown as a function of the annealing time at 800 °C (L_D - length of the dendritic precipitates).

The different temperatures of the RTA pre-treatment do not influence the edge length of the plate-like precipitates in the silicon samples annealed at 800 °C for 64 h as shown in Fig. 49. The edge length varies between about 30 nm and about 160 nm at each temperature of the RTA pre-treatment but the maximum length remains constant. The length variation could be caused by different starting points of the dendritic growth during annealing.

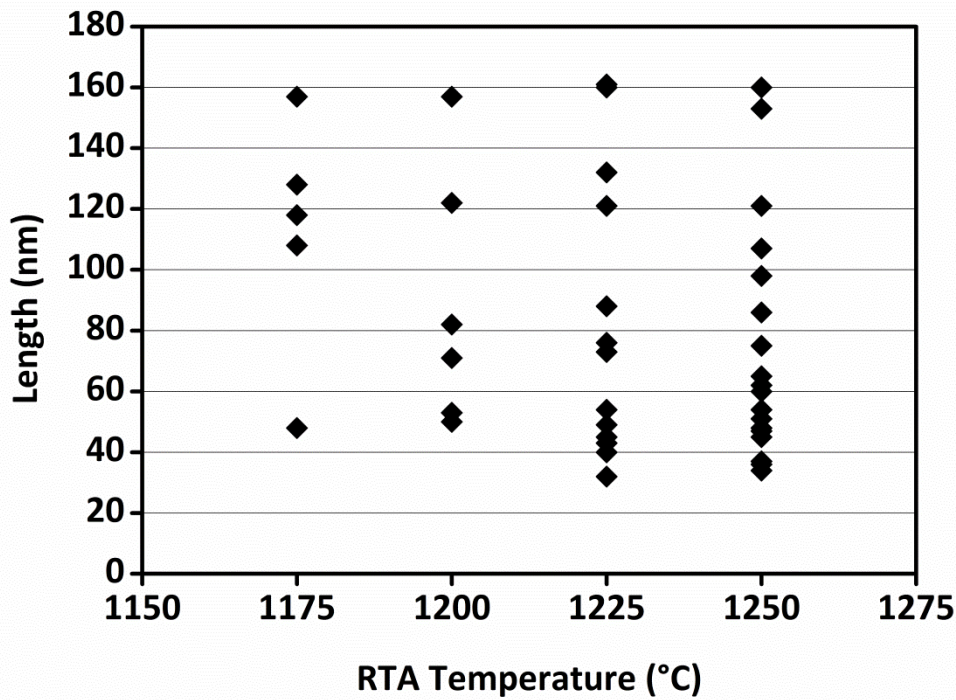


Figure 49: Edge length of 3D dendritic plate-like precipitates as a function of the RTA temperature for samples annealed at 800 °C for 64 h.

We also analyzed the growth kinetics of 2D dendritic and plate-like precipitates. The side lengths of the platelets plotted as a function of annealing time at 800 °C, 900 °C, and 1000 °C can be found in Figs. 50 (a), (b) and (c), respectively. Different fit functions are shown in the graphs, diffusion limited growth of platelets with and without limitation by oxygen consumption and linear fits for dendritic growth according to Eqs. (28) and (30), respectively. For annealing at 800 °C, the graph is very similar to Fig. 48 and the linear fit is the most suitable. For the 900 °C anneal, the data correspond to diffusion limited growth of a real platelet. At 1000 °C, most data can be fitted by diffusion limited growth but for 30 h only a linear fit with a growth rate of 19.3 nm/h can explain the size.

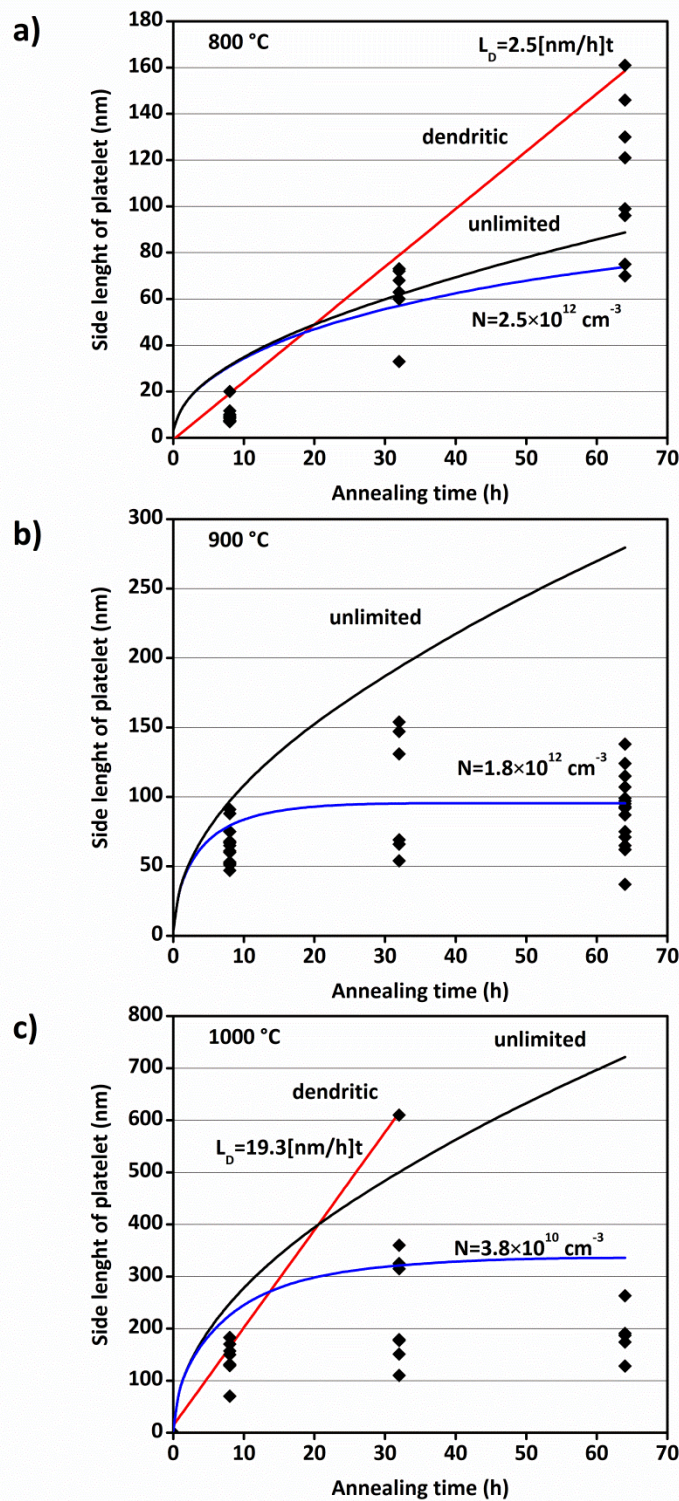


Figure 50: The side lengths of the platelets plotted as a function of annealing time at 800 °C (a), 900 °C (b), and 1000 °C (c). Side length of platelets calculated with (blue curve) and without (black curve) limitation by oxygen consumption according to Eqs. (28) and (30), respectively. Linear fits for dendritic growth (red line). N – density of oxygen precipitates.

Fig. 51 shows the side lengths of octahedral precipitates plotted as a function of the annealing time at 900 °C and 1000 °C. These data can be fitted well by diffusion limited growth of octahedral precipitates

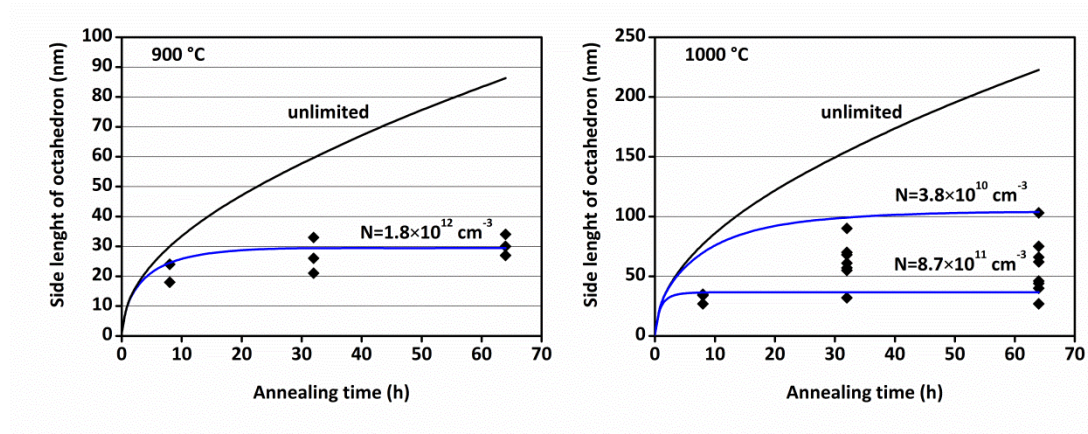


Figure 51: The side lengths of octahedral precipitates plotted as a function of annealing time at 900 °C and 1000 °C. The side lengths of octahedral precipitates calculated with (blue curve) and without (black curve) limitation by oxygen consumption according to Eqs. (27) and (30), respectively. N – density of oxygen precipitates.

Gettering of Cu at the edges of plate-like precipitates

Because of the low concentration of Cu atoms, the investigation of Cu getter sites by means of STEM and EDX in the samples with high density of defects is very difficult. For most cases, the presence of Cu at the surface of the defects or in the vicinity of the defects was not observed. A singular example of the presence of Cu at defect is shown in Fig. 52. The defect observed there is a plate-like precipitate which is partially dendritic as shown in EDX image in Fig 52 (a). A clear indication of Cu can be seen in Fig. 52 (b). In the image in Fig. 52 (d), where the images of EDX for O and Cu and the bright field images of the defect are overlapped, it is clearly demonstrated that Cu atoms accumulate at the edge of a precipitate. This is in good agreement with the assumption that a getter site could exist at the place of tensile strain.

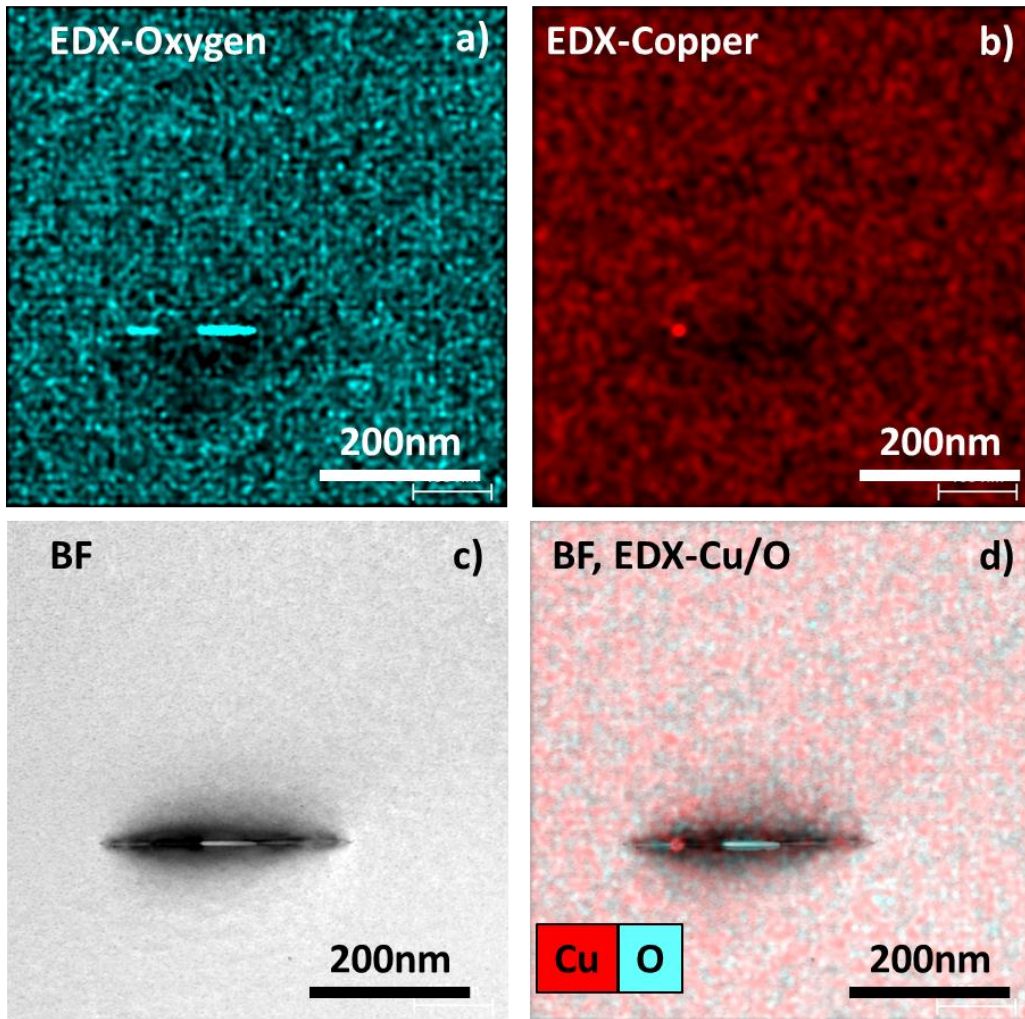


Figure 52: Cu aggregation at the edge of a plate-like precipitate: EDX of O (a), EDX of Cu (b), Bright Field (c), overlapped image of all previous images (d).

In the wafers which were highly contaminated with Cu, the Cu precipitates in the bulk of silicon by a repeated nucleation process on climbing edge dislocations forming Cu colonies [Nes71, Nes72, Nes73]. We found the same behavior of Cu in our investigations on the samples which were highly contaminated with Cu. In our investigations, the Cu colonies are always accompanied by oxygen precipitates. This means that oxygen precipitates play an important role in the nucleation process of Cu precipitates in silicon. Fig. 53 shows a 3D dendritic plate-like oxygen precipitate accompanied by a colony of Cu precipitates. In the HAADF image, the Cu precipitates exhibit a strong white contrast. The colony grows on an (001) plane being the extension of the plate-like precipitate. Fig. 54 shows a (010) plate-like precipitate in a (110) surface foil surrounded by a Cu colony on the (010) surface with dislocation loops

oriented in $\left[\bar{1}01 \right]$ and $\left[\bar{1}0\bar{1} \right]$ directions. The presence of Cu precipitates is approved by the EDX image presented in Fig. 54 (right).

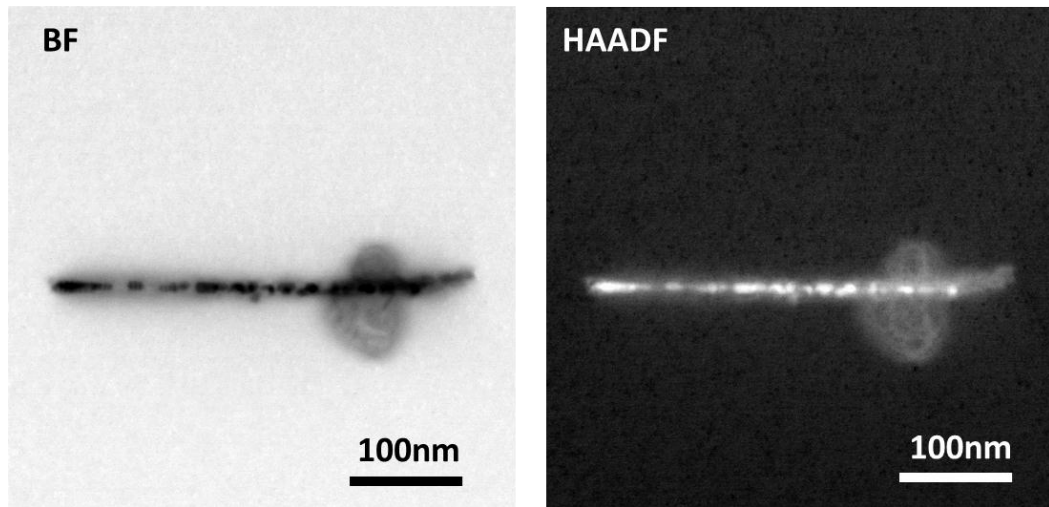


Figure 53: Cu colony at an oxygen precipitate: Bright Field (left), HAADF (right).

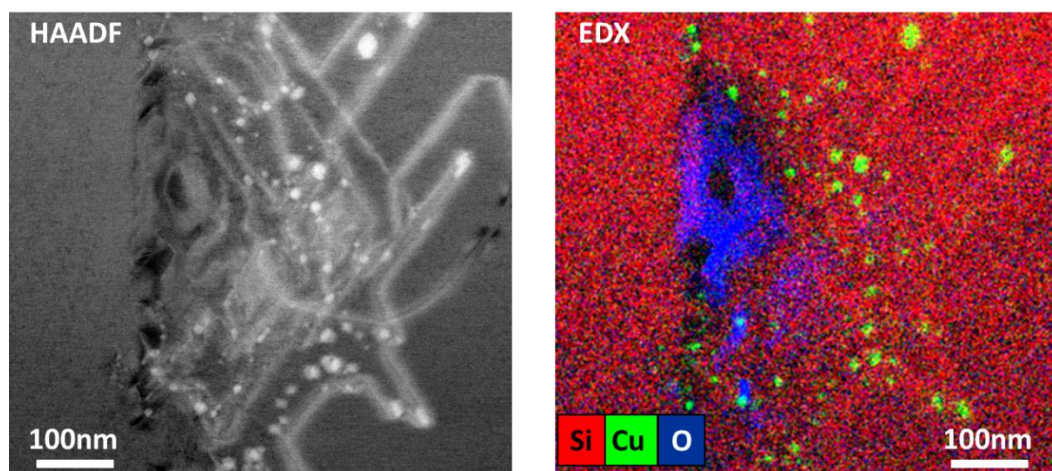


Figure 54: Cu colony at an oxygen precipitate: HAADF (left), EDX of Si, Cu and O (right).

6.2.5. Conclusions

The investigations carried out on the evolution of oxygen precipitates in RTA pre-treated wafers (vacancy supersaturated) and on the sites for Cu gettering showed that:

1. The morphology of the oxygen precipitates strongly depends on the annealing temperature. In the samples annealed at 800 °C for 8 h, the oxygen precipitates are too small to determine their morphology. However, the prolonged annealing showed that the oxygen precipitates at this temperature have the form of 3D or 2D dendrites. At 900 °C, octahedral precipitates, plate-like precipitates, 3D

dendrites and large square plate-like dendritic precipitates appeared. At 1000 °C, the oxygen precipitates that occur most frequently are octahedral or plate-like precipitates but large dendritic precipitates can be also found.

2. In the samples annealed at 800 °C for 64 h, the morphology of the oxygen precipitates does not depend on the temperature of the RTA pre-treatment. This means the morphology of the oxygen precipitates does not depend on the vacancy supersaturation. The morphology of the oxygen precipitates in this kind of treatment is 3D or 2D dendritic.
3. The BMD density in samples pre-treated by the RTA at 1250 °C for 30 s in oxygen containing Ar and annealed at 800 °C, 900 °C, or 1000 °C for 8 h, 32 h, or 64 h was in the range between $4 \times 10^{11} \text{ cm}^{-3}$ and $2.5 \times 10^{12} \text{ cm}^{-3}$.
4. The BMD density in the samples pre-treated by the RTA at 1250 °C, 1225 °C, 1200 °C, or 1175 °C for 30 s in oxygen containing Ar followed by an anneal at 800 °C for 64 h exponentially increases with increasing temperature of the RTA pre-treatment.
5. The different temperatures of the RTA pre-treatment do not influence the edge lengths of the plate-like precipitates in the silicon samples annealed at 800 °C for 64 h. The edge length varies between about 30 nm and about 160 nm for each temperature of the RTA pre-treatment.
6. For the samples annealed at 800 °C, the maximum length of the plate-like dendritic precipitates and the size of 3D dendrites increases linearly with time. The growth rate of dendritic precipitates at 800 °C amounts 2.5 nm/h. A dendritic growth rate of 19.3 nm/h was determined for 1000 °C. Dendritic precipitates can reach much larger dimensions than precipitates grown by usual diffusion limited growth.
7. Octahedral precipitates can be fitted by usual diffusion limited growth as usual.
8. The oxygen precipitates play an important role in the nucleation process of Cu precipitates in silicon. The edges of plate-like or dendritic precipitates which are tensile strained serve as getter sites for Cu. In the samples with high concentration of Cu further growth of Cu precipitates occurs by a repeated nucleation process on climbing edge dislocations.

6.3.FTIR

6.3.1. Introduction

The aim of the FTIR investigations was to get further information about the morphology of oxygen precipitates in the silicon samples and to compare the results with the results of the STEM investigations. The question if 3D dendrites cause new absorption band in the FTIR spectrum was of special interest. As it was mentioned already in chapter 2.2.1, the oxygen precipitates give rise to two characteristic absorption bands in the low temperature spectrum. The broad peak at 1095 cm^{-1} belongs to spherical precipitates and the broad peak at 1225 cm^{-1} to plate-like precipitates. In reality these two bands can consist of many smaller peaks originating from oxygen precipitates with slightly different morphologies. For example, the plate-like precipitates contributing to the plate-like peak can have different aspect ratios. In case of the peak of spherical precipitates, the precipitates contributing to this peak can have the form of an octahedron, a truncated octahedron, a polyhedron, a sphere or an oblate spheroid with various aspect ratios between long and short axis. Such a situation where various peaks belonging to the oxygen precipitates having different morphologies was predicted by a simulation based on the effective-medium theory (EMT) [Hu80, Bor92, Deg02, Tol03].

In the literature, many peaks were reported which can be attributed to different morphologies of the oxygen precipitates. The low temperature peaks at 1225 cm^{-1} , 1220 cm^{-1} , 1217 cm^{-1} , 1183 cm^{-1} , 1175 cm^{-1} , and 1170 cm^{-1} were assigned to plate-like precipitates and the peaks at 1124 cm^{-1} , 1120 cm^{-1} , 1116 cm^{-1} , 1095 cm^{-1} , and 1085 cm^{-1} were attributed to spherical precipitates [Hal92, Sas99, Sas00, Bor00]. However, in order to be able to study the absorption bands of oxygen precipitates by FTIR, the difference ΔO_i between the concentration of O_i before and after the thermal treatment should be at least $1.16 \times 10^{17}\text{ cm}^{-3}$ [Bor00].

6.3.2. Experimental details

For FTIR investigations two sets of samples were used. In the first set, the low O_i wafers were used. The samples were pre-treated by RTA at 1250 °C for 30 s and annealed at 800 °C, 900 °C, and 1000 °C for 8 h, 32 h and 64 h in N_2 . In the second set, the samples of low O_i wafers were pre-treated by RTA at 1200 °C, 1225 °C, and 1250 °C for 30 s and annealed at 800 °C for 4 h and 1000 °C for 16 h in N_2 .

6.3.3. Results and discussion

Fig. 55 shows the values of ΔO_i as a function of the annealing time for different annealing temperatures. All samples were pre-treated by RTA at 1250 °C. The low values of ΔO_i in some samples mean that in these samples the bands of oxygen precipitates will not be detectable. The highest values of ΔO_i belong to the samples annealed for 64 h. The low temperature spectra of these samples exhibit clear bands of oxygen precipitates as shown in Fig 56. The spectra of the samples annealed at 900 °C and at 1000 °C are very similar what is in good agreement with the results of the STEM investigations where the same types of defect were detected. However, some differences can be found. Both spectra have broad peaks at 1085 cm^{-1} and at 1225 cm^{-1} which can be attributed to the spherical and plate-like precipitates, respectively, but in the spectrum of the sample annealed at 1000 °C, the peak of the spherical precipitates is clearly split up in two sharp peaks at 1115 cm^{-1} and 1095 cm^{-1} . Moreover, the peak of the plate-like precipitates is significantly higher in the spectrum of the sample annealed at 900 °C than in the spectrum of the sample annealed at 1000 °C. The higher peak of the plate-like precipitates in sample annealed at 900 °C is in good agreement with the results of the STEM investigation where the estimated concentration of plate-like precipitates is higher in the sample annealed at 900 °C than in the sample annealed at 1000 °C. The two new peaks at about 1095 cm^{-1} and 1115 cm^{-1} observed in the spectrum of the sample annealed at 1000 °C probably belong to octahedral and truncated octahedral precipitates. According to STEM investigations the concentration of these precipitates is higher in this sample than in the sample annealed at 900 °C. Also the size of octahedral precipitates is about two times larger in the sample annealed at 1000 °C than in the sample annealed at 900 °C as it was shown in Fig. 51. A surprising fact is that the peak of the plate-like precipitates is larger in the sample annealed at 900 °C compared to the peak in the sample annealed at 1000 °C in spite, that the peaks

of spherical precipitates have the same intensity in the spectra of both samples and that the ΔO_i in both samples is almost the same. This anomalous behavior suggest that the peak of spherical precipitates is much less sensitive to the change of the concentration of oxygen in the precipitates than the peak of the plate-like precipitates or that only the sharp peaks at about 1095 cm^{-1} and 1115 cm^{-1} can be attributed to spherical precipitates (octahedral and truncated octahedral in this case) while the broad peak at 1085 cm^{-1} does not belong to spherical precipitates. This problem will be discussed in detail later.

A significant difference in the range of wave numbers of spherical precipitates between the spectra of the samples annealed at $900 \text{ }^\circ\text{C}$ or at $1000 \text{ }^\circ\text{C}$ and the sample annealed at $800 \text{ }^\circ\text{C}$ can be found. The absorption band of spherical precipitates in the sample annealed at $800 \text{ }^\circ\text{C}$ is much more flat than the absorption band in the samples annealed at $900 \text{ }^\circ\text{C}$ and at $1000 \text{ }^\circ\text{C}$. In addition, the absorption spectrum of the sample annealed at $800 \text{ }^\circ\text{C}$ has a shoulder at about 1050 cm^{-1} . Peaks at similar wave numbers are attributed to needle-like precipitates [Mis06, And10]. This would be in agreement with the STEM observations of 3D dendrites in the sample annealed at $800 \text{ }^\circ\text{C}$. The structure of these 3D dendrites is based on needle-like branches.

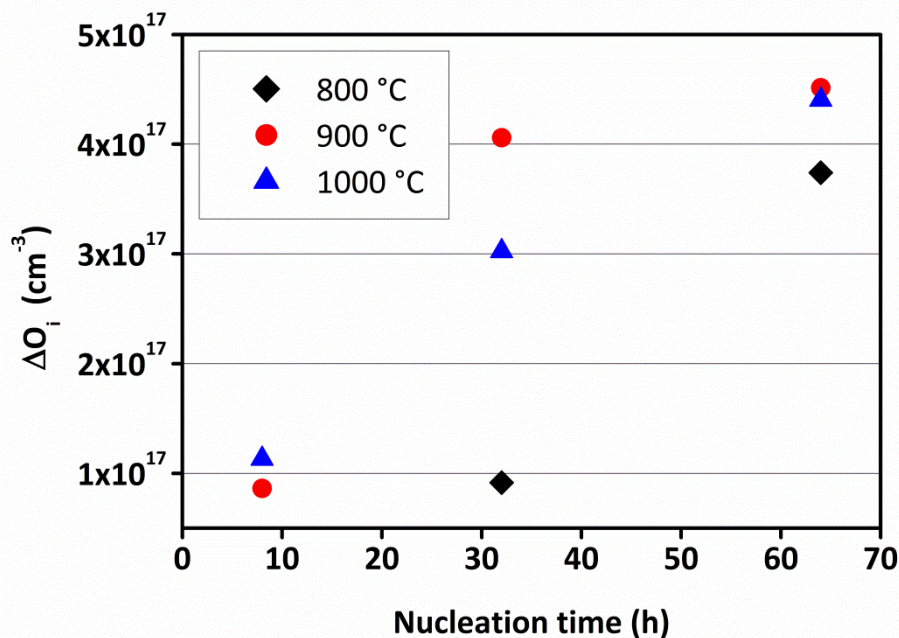


Figure 55: ΔO_i as a function of annealing time for different temperatures of annealing. These samples were pre-treated by RTA at $1250 \text{ }^\circ\text{C}$.

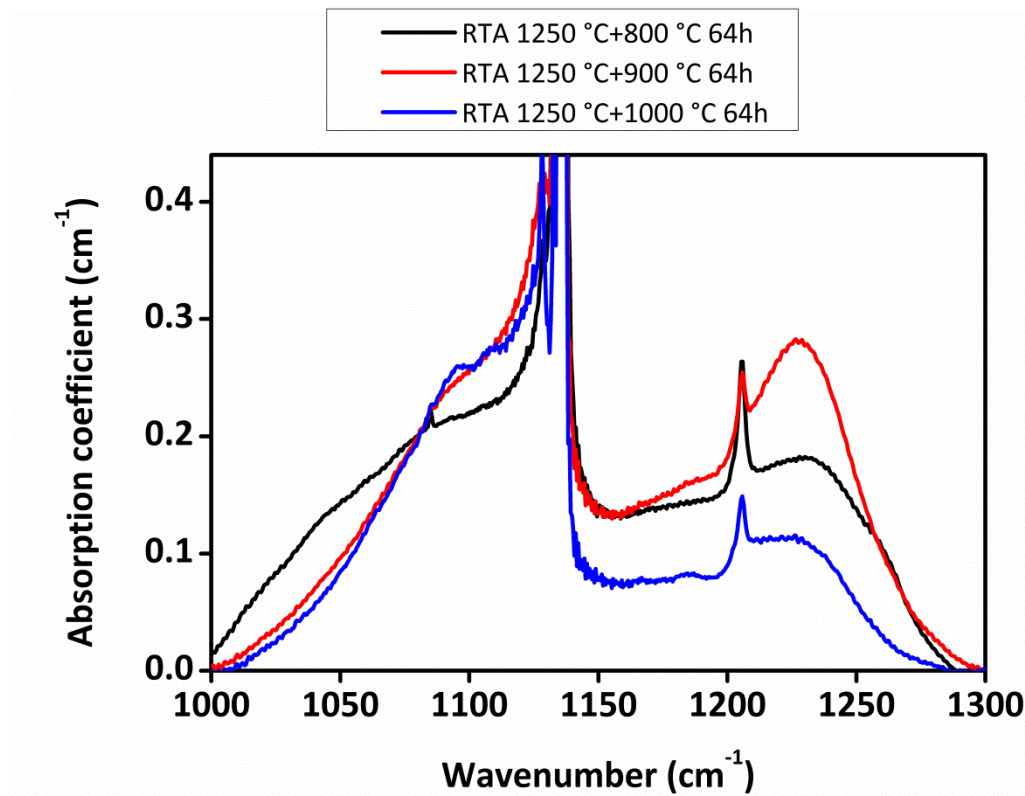


Figure 56: FTIR spectra of samples pre-treated by RTA at 1250 °C subsequently annealed at 800 °C, 900 °C, or 1000 °C for 64 h.

In order to find the contributions of the peaks of oxygen precipitates, the spectra were deconvoluted. This was carried out by means of the WiRE software for peak deconvolution. For the deconvolution of the spectra, twelve peaks were used. Five of them at 1128 cm⁻¹, 1132 cm⁻¹, 1134 cm⁻¹, 1136 cm⁻¹, and 1205 cm⁻¹ belong to the O_i peaks or their satellites. These peaks are only used to get the best fit and therefore they are not shown in Figs. 57 and 58. The rest of the peaks at 1060 cm⁻¹, 1080 cm⁻¹, 1095 cm⁻¹, 1116 cm⁻¹, 1124 cm⁻¹, 1175 cm⁻¹, and 1225 cm⁻¹ are the peaks of the oxygen precipitates. The results of the deconvolution of the spectra of the samples annealed at 800 °C and at 1000 °C both for 64 h are shown in Fig. 57 (top) and (bottom), respectively.

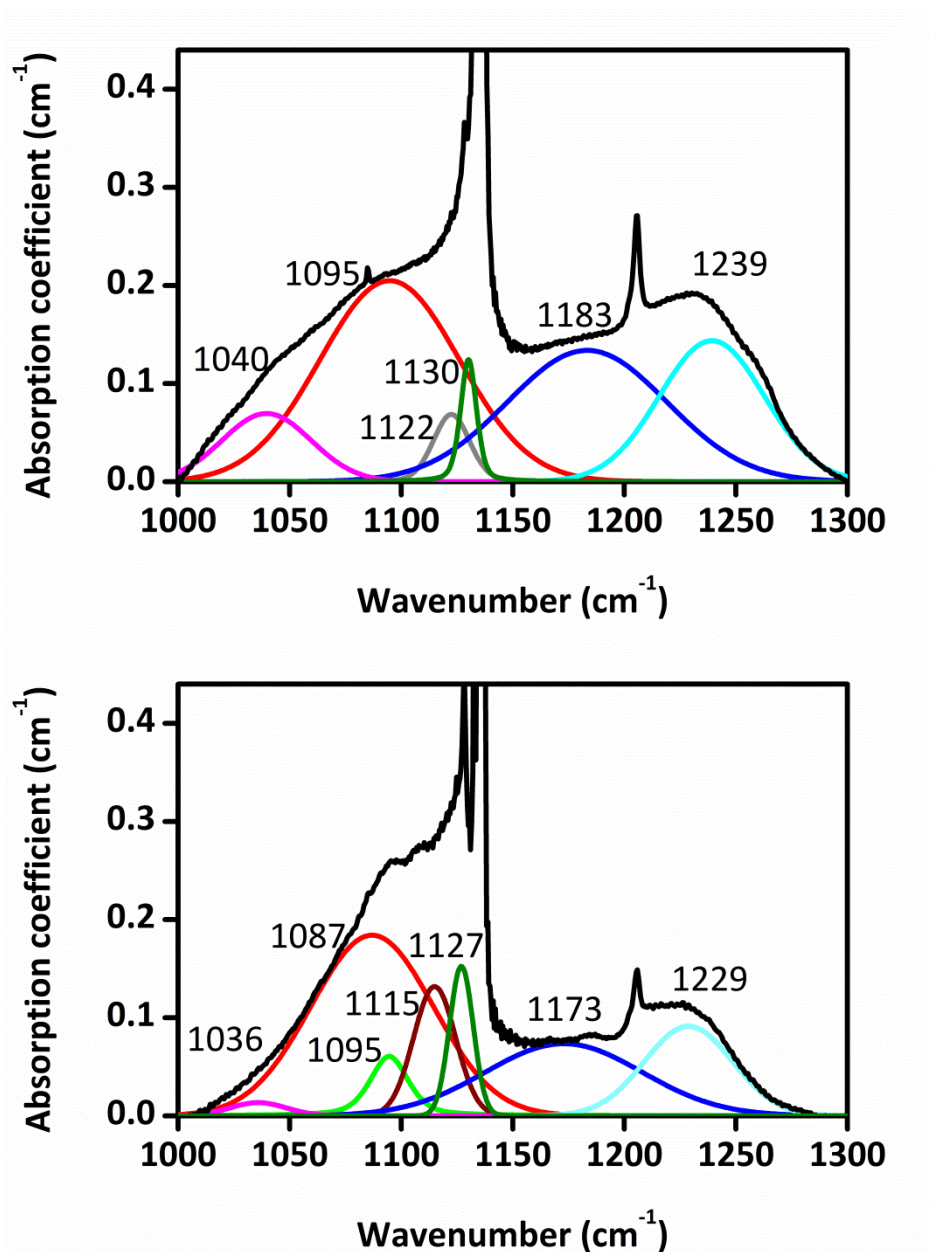


Figure 57: Deconvolution of the spectral range of oxygen precipitates for samples pre-treated by RTA at 1250 °C and annealed at 800 °C (top) and 1000 °C (bottom) both for 64 h.

After deconvolution, all 7 peaks of the precipitates assumed in the beginning remained in the spectrum of the sample annealed at 1000 °C. In the spectrum of the sample annealed at 800 °C, one of the peaks set at the beginning of deconvolution, the peak at 1095 cm^{-1} , was lost and some peaks had to be shifted with respect to their initial position. The peaks of the plate-like precipitates at 1225 cm^{-1} and 1175 cm^{-1} appear in the spectra of both samples but they are shifted with respect to their initial position. Now, they are located at 1239 cm^{-1} and at 1183 cm^{-1} in the spectrum of the sample annealed at 800 °C and at 1229 cm^{-1} and at 1173 cm^{-1} in the spectrum of the sample

annealed at 1000 °C. This difference in the peak positions could be related to different aspect ratios of the plate-like precipitates in these samples or to a different composition of the precipitated phase SiO_x [Deg02]. The presence of the peaks of plate-like precipitates in the spectrum of the sample annealed at 800 °C suggests that some 2D dendrites, which were found by STEM in this sample, are partially or fully transformed into plate-like precipitates due to the fulfillment of the space between branches by oxygen. The next peak set at 1124 cm^{-1} at the beginning of deconvolution shifted towards higher wave numbers compared to the initial value in the spectrum of both samples. Now it is located at 1130 cm^{-1} in the spectrum of the sample annealed at 800 °C and at 1127 cm^{-1} in the spectrum of the sample annealed at 1000 °C. This peak is very similar in the spectra of both samples what means that these samples have similar defects. It could be related to small spherical precipitate nuclei which exist at the beginning of the growth [Vor01, Sue03]. Such type of precipitates should be present at any time of annealing due to the fact that precipitates start to grow at different times of annealing. The next two peaks set at 1116 cm^{-1} and 1095 cm^{-1} at the beginning of deconvolution do not change their position in the spectrum of the sample annealed at 1000 °C where they are also clearly seen in the experimental spectrum. As it was mentioned at the beginning of this chapter these peaks can belong to octahedral and truncated octahedral precipitates. This thesis is supported by STEM investigations and the observation of other authors [Sas99, Bor00]. It is important to note that, these peaks are not present in the spectrum of the sample annealed at 800 °C where neither octahedral nor truncated octahedral precipitates were found. In this sample, the peak set at 1095 cm^{-1} at the beginning of deconvolution disappeared and the peak set at 1115 cm^{-1} was shifted to 1122 cm^{-1} being significantly decreased. The morphology of oxygen precipitates which give rise to this peak could be small spherical precipitates like in case of the peak at 1130 cm^{-1} . The next peaks in the set of deconvolution located at 1085 cm^{-1} is the highest peak in the spectra of both samples annealed at 800 °C and at 1000 °C. After deconvolution, it was shifted to 1095 cm^{-1} for the sample annealed at 800 °C. Although, the wave number is the same as for the peak of the octahedral or truncated octahedral precipitates in the spectrum of the sample annealed at 1000 °C the width is much higher. Thus, it cannot be associated with these defects. In the sample annealed at 1000 °C, the discussed peak appears at 1087 cm^{-1} that means, almost at the initially set position. In the literature, the origin of this peak is usually associated with spherical precipitates [Hu80, Hal92, Sas99, Bor00] but same authors [Gaw84] connect

it with plate-like precipitates. Hallberg et al. assume that the peak at 1085 cm^{-1} is attributed to spherical precipitates because its incubation time and the incubation time of the peak of plate-like precipitates at 1225 cm^{-1} are different [Hal92]. Gaworzewski et al. observed also a double-peaked type spectrum with bands at 1225 cm^{-1} and 1120 cm^{-1} . Because they have never seen spectra with a single peak at 1225 cm^{-1} they assumed that both peaks are attributed to the plate-like precipitates. Moreover, they considered total reflection from the plate-like precipitates. Using the optical constant of silica they get two transmittance minima at about 1240 cm^{-1} and 1080 cm^{-1} which they attributed to the longitudinal mode (LO) and transverse mode (TO). They also present an example of the optical behavior of silica with a splitting of the Si-O stretching vibrations of the layer silicates due to strong anisotropy between the lateral size and the thickness the Si-O stretching vibration mode which splits into perpendicular and parallel modes. However, the appearance of a broad symmetric band at 1100 cm^{-1} but without accompanying band at 1225 cm^{-1} , Gaworzewski et al. attributed to “globular” precipitates [Gaw84].

Since octahedral and truncated octahedral precipitates are not observed by STEM in the sample annealed at $800\text{ }^{\circ}\text{C}$ and the peak at 1095 cm^{-1} is the highest in the spectrum and very broad, it cannot be attributed to the octahedral or truncated octahedral precipitates. Because the 3D dendrites are the main defects which are detected in this kind of sample, the peak at 1095 cm^{-1} originates from this kind of defects or the needle-like precipitates which the 3D dendrites are made of. Additionally, the band at 1095 cm^{-1} could contain a contribution from the TO mode of plate-like precipitates, dendritic precipitates, and needle-like precipitates therefore its position could depend on the content of these modes and therefore the position of this peak is shifted to 1087 cm^{-1} in the spectrum of the sample annealed at $1000\text{ }^{\circ}\text{C}$.

The last peak initially set at 1060 cm^{-1} shifts to lower wave numbers. In the sample annealed at $800\text{ }^{\circ}\text{C}$, this peak is located at 1040 cm^{-1} in the spectrum. So significantly as it is visible here, it appears no more else. Thus, the 3D, and 2D dendrites precipitates are the defects which can be attributed to this peak because the STEM investigation did not show singular needle-like precipitates. They occur in the silicon bulk as branches of dendrites.

Fig. 58 shows the bands of the oxygen precipitates obtained after deconvolution of the spectrum of the sample annealed at $900\text{ }^{\circ}\text{C}$ for 64 h. The dominant peak at 1229 cm^{-1} belongs to plate-like precipitates as expected from the STEM results. The

peak of 3D dendrites at 1039 cm^{-1} has very low intensity as well as peak of octahedral/ truncated octahedral precipitates located at 1107 cm^{-1} in this sample. The peaks at 1123 cm^{-1} and 1130 cm^{-1} are similar to the peaks observed in the sample annealed at $800\text{ }^{\circ}\text{C}$ at 1122 cm^{-1} and 1130 cm^{-1} and probably they originate from the same types of oxygen precipitates. The peak set at 1080 cm^{-1} at the beginning of deconvolution, located now at 1101 cm^{-1} , is very high. Because the concentration of 3D dendrites and octahedral or truncated octahedral precipitates in this sample is very low, the plate-like precipitates must be an origin of this peak as suggested by Gaworzewski [Gaw84], mainly by the contribution of the TO mode as predicted from simulations in Ref. [Sas00].

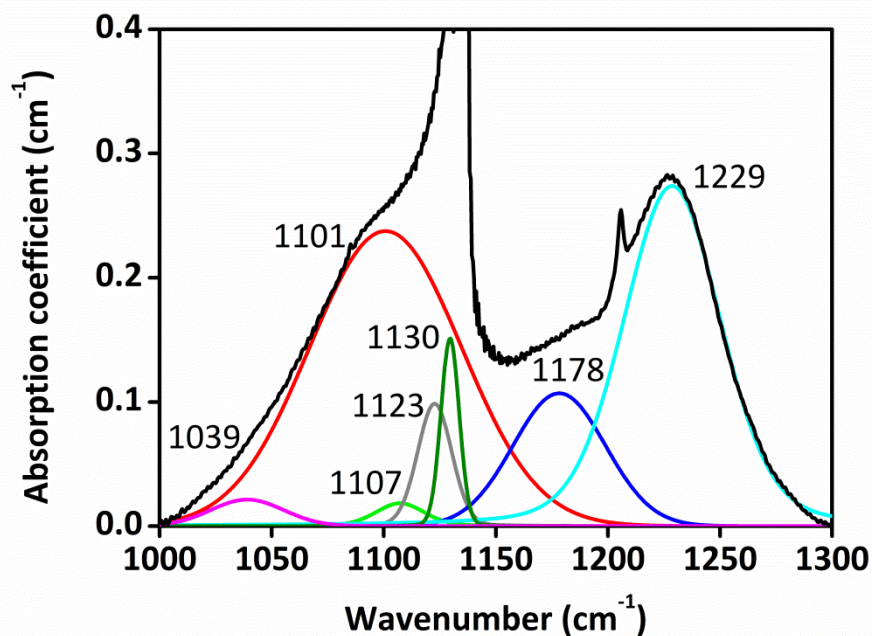


Figure 58: Deconvolution of the spectral range of oxygen precipitates for the sample pre-treated by RTA at $1250\text{ }^{\circ}\text{C}$ and annealed at $900\text{ }^{\circ}\text{C}$ for 64 h.

Fig. 59 compares the heights of the four peaks which were discussed with respect of their origin. The first peak with the position at about 1040 cm^{-1} was attributed to 3D dendrites or needle-like precipitates. Its intensity decreases with increasing temperature of annealing and the maximum appears for the sample annealed at $800\text{ }^{\circ}\text{C}$. The next peak in Fig. 59 with the waver number between 1087 cm^{-1} and 1101 cm^{-1} originally considered to be a peak of spherical precipitates, in this work is attributed to the TO mode of plate-like precipitates. It behaves like the LO mode of the plate-like precipitates at 1229 cm^{-1} , what proves its assignment to this kind of precipitates. The maximum of this peak occurs in the sample annealed at $900\text{ }^{\circ}\text{C}$ what is in good

agreement with the STEM results. The peak of octahedral/truncated octahedral precipitates at 1107 cm^{-1} has a maximum intensity in the sample annealed at $1000\text{ }^{\circ}\text{C}$ as expected from STEM. This peak was not detectable in the sample annealed at $800\text{ }^{\circ}\text{C}$.

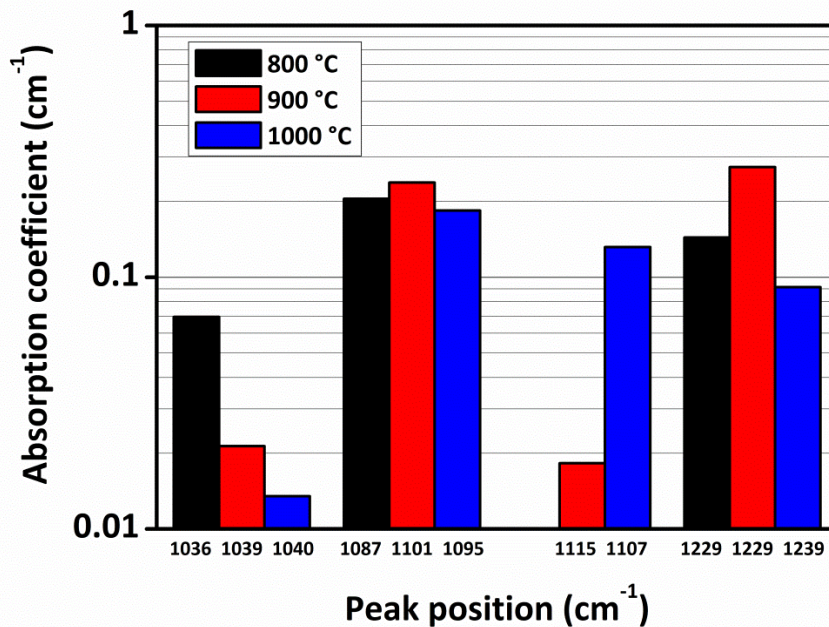


Figure 59: Absorption coefficient at peak maximum as a function of peak position for samples pre-treated by RTA at $1250\text{ }^{\circ}\text{C}$ and annealed at different temperatures.

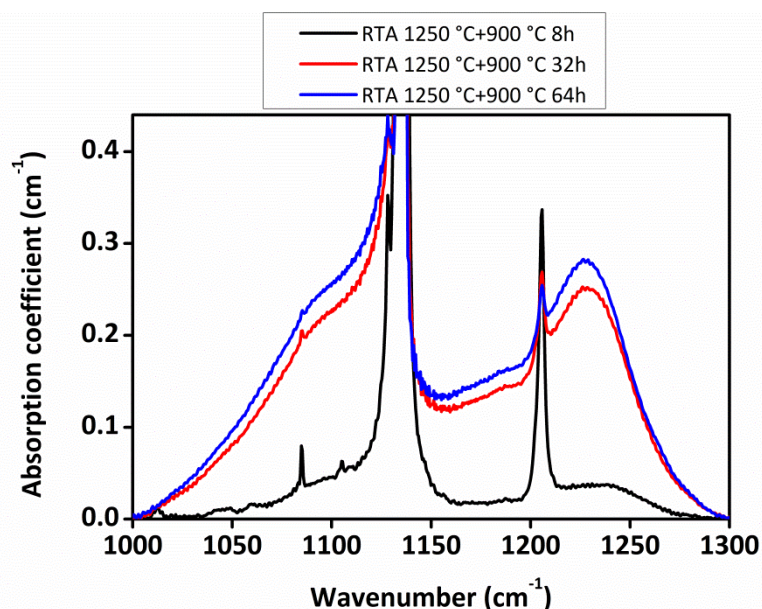


Figure 60: FTIR spectra for samples pre-treated by RTA at $1250\text{ }^{\circ}\text{C}$ and annealed at $900\text{ }^{\circ}\text{C}$ for 8 h, 32 h, and 64 h.

Figs. 60 and 61 show the evolution of the bands of the oxygen precipitates during annealing in the spectra of the samples annealed at $900\text{ }^{\circ}\text{C}$ and at $1000\text{ }^{\circ}\text{C}$, respectively. In both cases, the spectra of the samples annealed for 8 h exhibit weak intensity from

the precipitates as expected from their low ΔO_i . In the sample annealed at 900 °C for 32 h, the peaks of the precipitates have almost the same intensity like in the sample annealed for 64 h. The shape of the peaks of the oxygen precipitates is also the same what is consistent with the STEM results of these samples where the same types of precipitates were observed. In the samples annealed at 1000 °C for 32 h and 64 h, a significant difference between the intensity of the peaks of the oxygen precipitates is seen. After 32 h of annealing, the peaks of the octahedral and truncated octahedral precipitates located at 1095 cm^{-1} and 1115 cm^{-1} are significantly smaller than in the spectrum of the sample annealed for 64 h. However, the peak of the plate-like precipitates located at 1229 cm^{-1} is clearly higher compared to the sample annealed for 64 h. According to the STEM results, the difference between the samples annealed for 32 h and 64 h is the ratio between octahedral/truncated octahedral precipitates and plate-like precipitates. The concentration of octahedral/truncated octahedral precipitates increases with increasing annealing time while the concentration of plate-like precipitates decreases. These results show good agreement between results of STEM and FTIR. Such a behavior of oxygen precipitates can be explained by a transformation of the plate-like precipitates to octahedral or truncated octahedral precipitates as reported in Ref. [Has92].

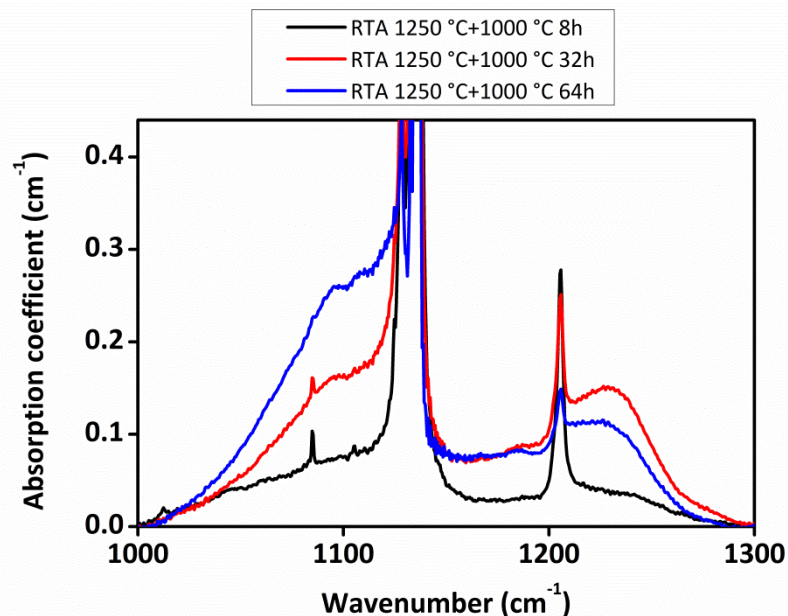


Figure 61: FTIR spectra of samples pre-treated by RTA at 1250 °C and annealed at 1000 °C for 8 h, 32 h, or 64 h.

6.3.4. Conclusions

In this chapter, samples pre-treated by RTA at 1250 °C and annealed at 800 °C, 900 °C, or 1000 °C were investigated by means of FTIR spectroscopy. The low temperature spectra recorded at liquid helium temperature were subjected to a deconvolution in order to separate the band of oxygen precipitates having different morphology. Afterwards, the bands were attributed to appropriate morphologies of oxygen precipitates based on the STEM results and bands assigned from literature. The analysis of the FTIR spectra showed that:

1. The sample annealed at 800 °C reveals a band of dendritic or needle-like precipitates which is located at 1040 cm^{-1} .
2. The peaks of octahedral and truncated octahedral precipitates are located at 1095 cm^{-1} and 1115 cm^{-1} in the spectrum of the sample annealed at 1000 °C.
3. The peak at 1130 cm^{-1} or 1127 cm^{-1} belongs to small spherical precipitates.
4. The peaks at 1101 cm^{-1} and 1229 cm^{-1} are the TO and LO modes of plate-like precipitates, respectively. The maximum intensity of these peaks appears in the sample annealed at 900 °C. The low wave number peak can contain a contribution of other precipitates like spherical 3D dendrites or needle-like precipitates including their TO modes.
5. The peak between 1173 cm^{-1} and 1183 cm^{-1} belongs to plate-like precipitates.
6. In the sample annealed at 1000 °C the plate-like precipitates transform to octahedral or truncated octahedral precipitates with increasing annealing time for times longer 32 h.

6.4.Haze getter test

6.4.1. Introduction

Although, vacancy supersaturation enhances oxygen precipitation in silicon, some authors reported that the oxygen precipitates formed after the RTA pre-treatments are characterized by a weaker getter efficiency than the precipitates grown without RTA pre-treatment [Mad96]. This weaker getter efficiency was accompanied by the change of the morphology of the oxygen precipitates from plate-like to spherical. The getter efficiency of the spherical precipitates is assumed to be lower because of the lower surface compared to plate-like precipitates [Sue05]. As it was shown in the previous section, the RTA pre-treatment has nearly no impact on the morphology of oxygen precipitates. A significant difference in the morphology of the oxygen precipitates for wafers with and without RTA pre-treatment can be only observed for nucleation annealing at 800 °C while at higher temperatures the morphology of the oxygen precipitates is the same as in the samples without RTA pre-treatment.

The aim of the getter experiments carried out in this work was to investigate the getter efficiency in the vacancy supersaturated wafers and the influence of vacancy supersaturation on the getter efficiency of singular precipitates. In this chapter, the results of Cu, Ni and Pd gettering in samples containing different concentrations and sizes of oxygen precipitates are presented.

Oxygen precipitates were formed in the RTA pre-treated samples annealed in the temperature range between 700 °C and 1000 °C. The getter efficiency was determined for the wafers with low and high concentration of O_i . The getter efficiency was determined by the haze getter test described in section 4.4. The concentration of metals in the contaminated samples is assumed to be equal to their solubility limit at the temperature of the drive-in step being 900 °C. The results of the getter tests were compared with the results of other authors.

6.4.2. Experimental details

Using the haze getter tests, two sets of experiments were carried out. In the first, low O_i wafers were used. The samples were pre-treated by RTA at 1175 °C, 1200 °C, 1225 °C, and 1250 °C for 30 s and annealed at 700 °C, 800 °C, 900 °C, and 1000 °C for 4 h or 8 h. In the second set of experiments, high O_i wafers were used. One part of the samples was pre-annealed at 1000 °C for 15 min and the second part was pre-treated by RTA at 1250 °C for 30 s. After that, the samples were annealed at 700 °C, 800 °C, 900 °C, and 1000 °C for 0.5 h, 1 h, 2 h, 4 h, or 8 h in N_2 . After annealing, the samples were contaminated with Cu, Ni or Pd and subjected to the haze getter test (see chapter 4.4).

6.4.3. Results and discussion

The results of the Cu and Ni getter efficiencies are very similar therefore the data expressing sufficient and insufficient gettering of these metals are shown in the same figure. Fig. 62 shows the getter efficiency of Cu and Ni in the low oxygen samples pre-treated by RTA at 1175 °C, 1200 °C, 1225 °C, or 1250 °C which were subjected to a nucleation anneal at temperatures between 700 °C and 1000 °C for 4 h (right) or 8 h (left). Sufficient gettering means that the getter efficiency is higher or equal 90% calculated according to Eq. 36. In the low O_i samples annealed for 8 h, sufficient gettering of metal impurities occurs already at 780 °C for wafers pre-treated by RTA at 1250 °C and at 900 °C for wafers pre-treated by RTA at 1200 °C and higher. In case of the samples annealed for 4 h, sufficient gettering appears at 850 °C for the wafer pre-treated by RTA at 1250 °C and at 900 °C for the wafers pre-treated by RTA at 1200 °C and higher. A sufficient gettering of Cu and Ni was never observed in the samples pre-treated by RTA below 1175 °C. Increasing the vacancy concentration in samples is always connected with an increase of the concentration of oxide precipitates after annealing. By increasing the vacancy concentration, it is possible to achieve sufficient gettering of metal impurities at decreased temperatures.

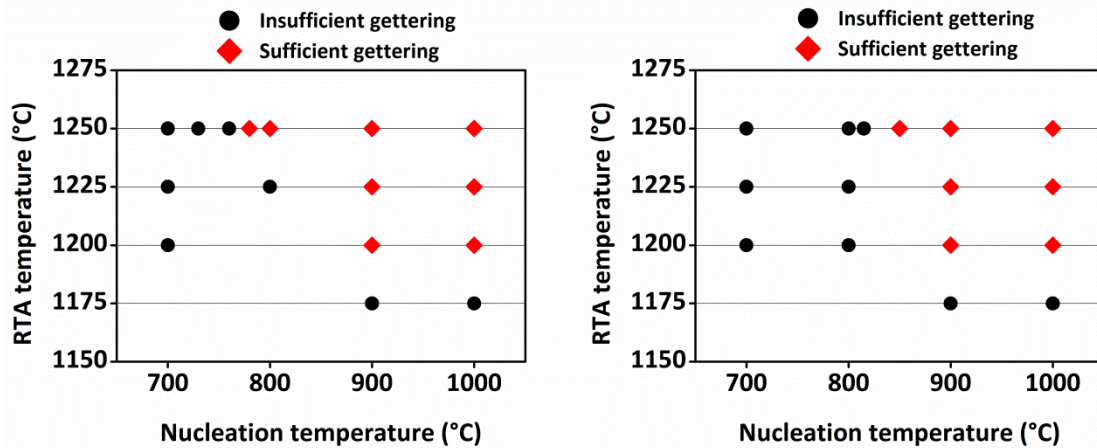


Figure 62: Cu and Ni gettering as a function of the nucleation temperature and temperature of the RTA pre-treatment for samples annealed for 8 h (left) or 4 h (right). Insufficient gettering is marked by black circles and sufficient gettering by red diamonds.

In Fig. 63, the getter efficiencies of Cu or Ni in the silicon wafers pre-treated by RTA at 1250 °C or pre-annealed at 1000 °C for 15 min both followed by annealing at 700 °C, 800 °C, 900 °C, and 1000 °C for 0.5 h, 1 h, 2 h, 4 h, or 8 h are shown. The concentration of interstitial oxygen in these wafers was high. For the samples pre-treated by RTA at 1250 °C, sufficient gettering appears after 4 h of nucleation anneal at 800 °C and already after 0.5 h for the samples annealed at a temperature of 900 °C and at higher temperatures. Samples with shorter time of nucleation than 0.5 h were not investigated. The samples annealed at 700 °C for 8 h do not getter sufficiently.

In the samples pre-annealed at 1000 °C for 15 min, sufficient gettering occurs in the samples after 8 h of nucleation anneal at 900 °C and in the samples after 1 h of nucleation anneal at 1000 °C and at higher temperatures. The samples annealed at temperatures lower than 900 °C are characterized by insufficient gettering. Compared to the pre-annealed samples, sufficient gettering in the vacancy-rich wafers can be obtained at much lower thermal budget.

For this set of samples, an additional palladium haze test was carried out. Although in case of Pd, the getter efficiency was determined by visual estimations, where the spot of the haze observed on the surface means insufficient gettering and its lack on the surface means sufficient gettering, the results are similar to Cu and Ni haze getter test. Sufficient gettering in the samples pre-treated by RTA appears at the same nucleation temperatures and for the same nucleation time as for Cu and Ni. This is shown in Fig. 64. Slightly different results were observed in the samples pre-annealed at 1000 °C

for 15 min where sufficient gettering occurs in the samples after the nucleation anneal for 8 h at 900 °C and in the samples after nucleation anneal equal or longer than for 4 h at 1000 °C as shown in Fig. 65. These results indicate that the Pd getter test can be a good reference test for the Cu and Ni getter efficiency in the samples contaminated with high concentration of Cu or Ni.

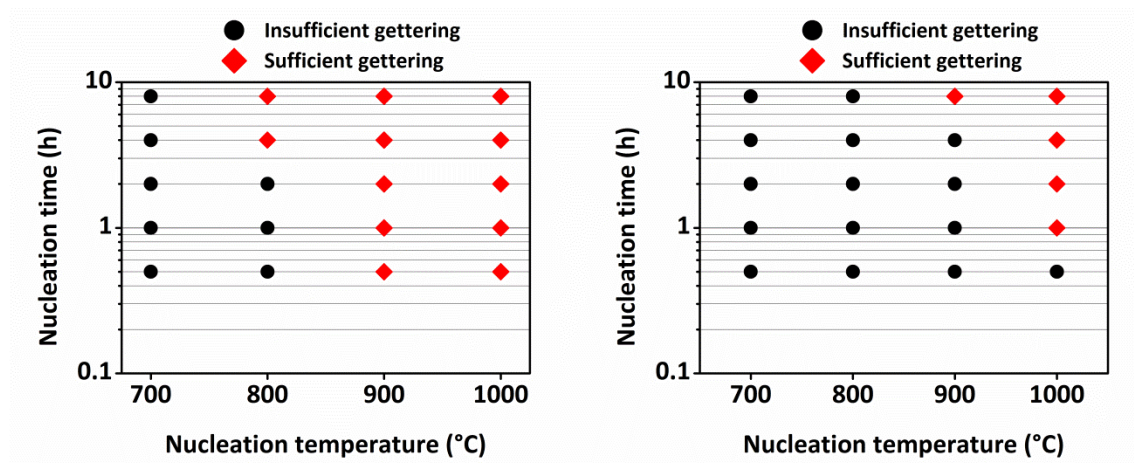


Figure 63: Cu and Ni gettering as a function of the nucleation time and nucleation temperature for samples pre-treated by RTA at 1250 °C (left) and samples pre-annealed at 1000 °C for 15 min (right). Insufficient gettering is marked by black circles and sufficient gettering by red diamonds. Samples were cut out from high O_i wafers.

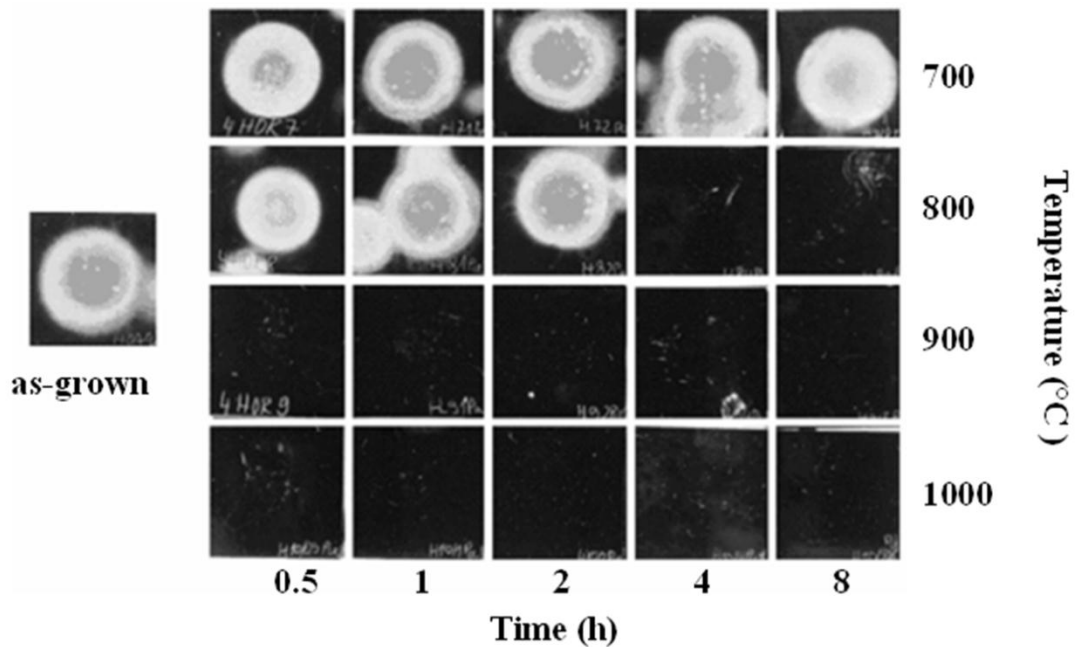


Figure 64: Palladium haze tests on samples pre-treated by RTA at 1250 °C.

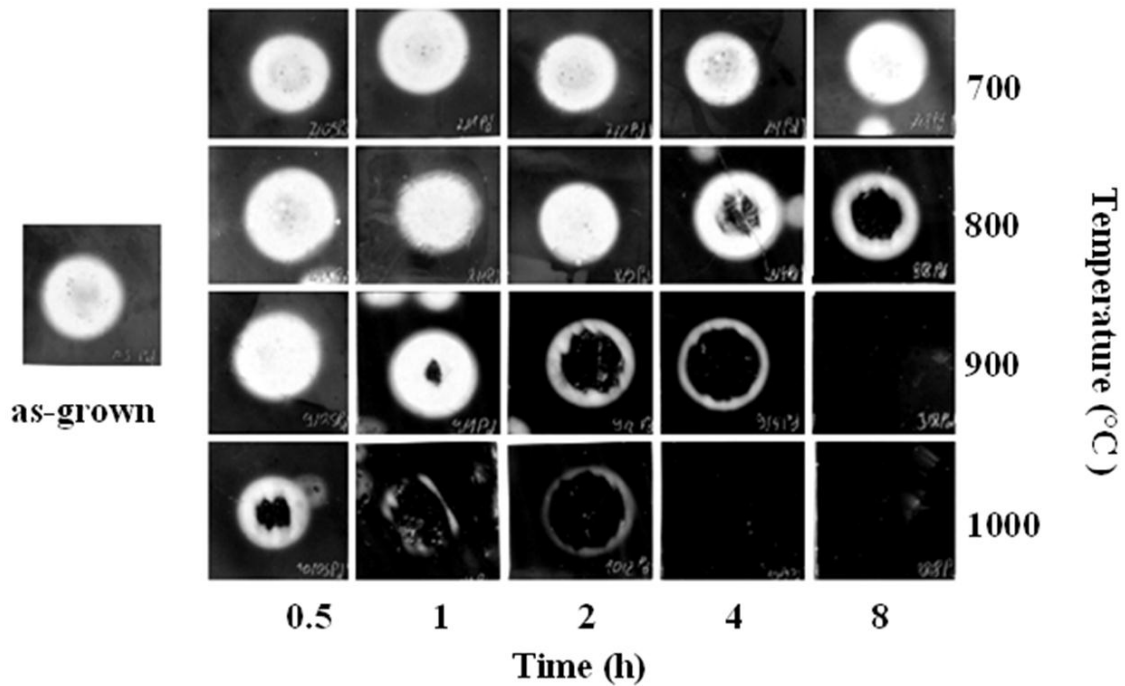


Figure 65: Palladium haze tests on samples pre-annealed at 1000 °C for 15 min.

Size and density of oxygen precipitates as a function of the getter efficiency

Fig. 66 shows the dependence of the Cu and Ni getter efficiency as a function of the density of the plate-like precipitates and their edge length calculated according to Eq. 28 with an aspect ratio of 0.03. The plot includes all data of the getter efficiency obtained by the haze getter test. Please note that not all precipitates are plate-like in reality according to the STEM results. The red dashed line in Fig. 66 indicates the threshold for sufficient getting of Ni as obtained by Sueoka et al. [Sue00] for samples contaminated with of $5 \times 10^{11} \text{ cm}^{-2}$ of Ni.

The results in this work are in a good agreement with Sueoka's threshold but only for the BMD densities up to about $1 \times 10^{10} \text{ cm}^{-3}$. For higher BMD densities, sufficient getting is limited by the edge length of plate-like precipitates. The efficient getting limited by the size of oxygen precipitates was already reported in Ref. [Sea02]. The break of the line separating data of sufficient getting from the insufficient getting would suggest that the getting mechanism is not directly related with the interface of oxygen precipitates but rather with some indirect process like generation of a certain tensile strain at the edge of plate-like precipitates or by emission of a certain amount of silicon interstitials from the precipitates. It should be mentioned that for large precipitates the getter effect of oxygen precipitates is enhanced if they are accompanied by punched-out dislocations which are also getter sites for Ni and Cu. According to Ref.

[Sue00] about 140 nm is a critical plate-like edge length for the generation of punched-out dislocations.

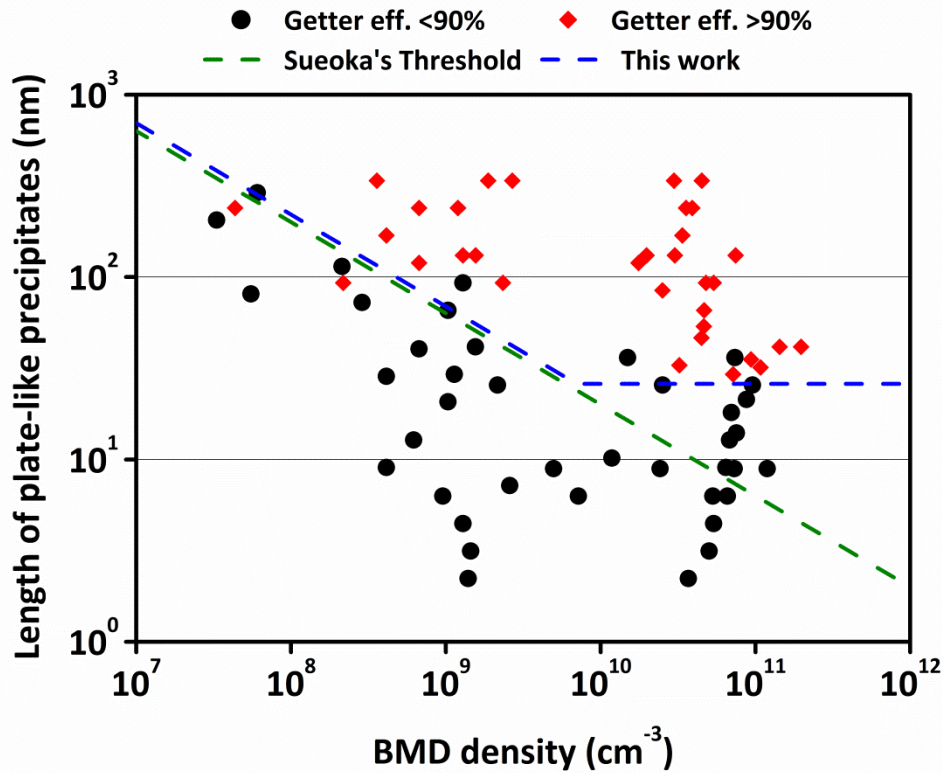


Figure 66: Ni and Cu getter efficiency shown for the length of plate-like precipitates and the BMD density.

Normalized inner surface of precipitates

In order to further investigate the gettering mechanisms, the data of Cu and Ni getter efficiencies were plotted as a function of the normalized inner surface of precipitates. According to Hölzl et al. [Höl02], the oxygen precipitates in silicon wafers after annealing at certain temperatures for certain time reach a point at which the total surface area of all precipitates is large enough for efficient gettering of metal impurities. This area of all precipitates was defined by Hölzl as the total inner surface. The normalized inner surface according to Hölzl's work which assumes spherical precipitates is determined as follows:

$$S_{BMD} = 4\pi \cdot r(t)^2 \cdot N_{BMD}(t) \cdot d_w \quad [42]$$

In the above equation, d_w is the thickness of the wafer, $N_{BMD}(t)$ is the density of BMDs which are mainly oxygen precipitates, $r(t)$ the radius of oxygen precipitates after a

certain time of annealing t according Eq. (26). The threshold value of the normalized inner surface S_{crit} is archived if the getter efficiency exceeds 90%.

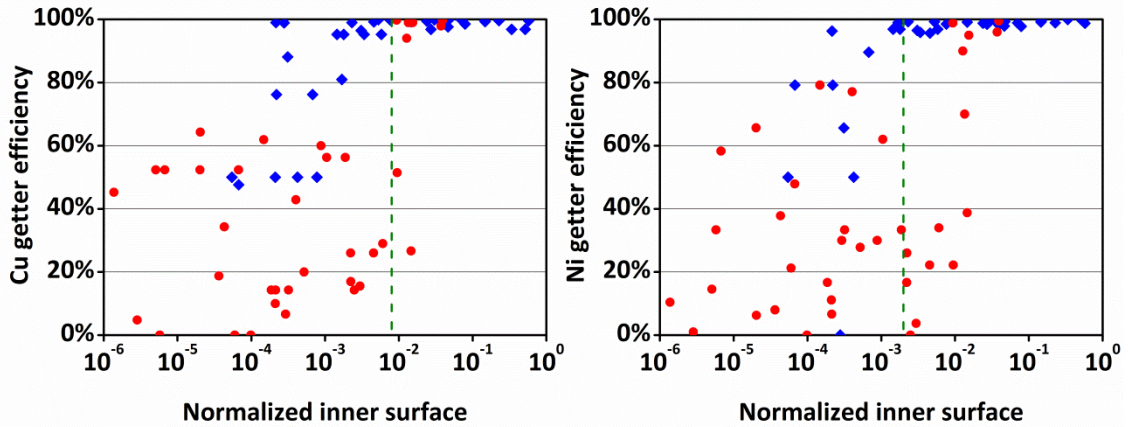


Figure 67: Cu (left) and Ni (right) getter efficiency as a function of the normalized inner surface: samples with precipitates free of dislocation (red circles), samples with precipitates associated with dislocations (blue diamonds), Hölzl's threshold (dashed green line).

Fig. 67 shows the Cu and Ni getter efficiency both as a function of the normalized inner surface. The plotted data belong to all samples subjected to the haze getter test. The values of the samples annealed at a temperature lower than 900 °C were plotted in a red color and all other values in a blue color. The dashed lines indicate the threshold values determined by Hölzl for contamination in the 10^{11} - 10^{12} cm⁻² range. In case of the Cu getter efficiency, indeed all gettering samples have higher values of the total inner surface than the threshold determined by Hölzl. However, there are also samples with lower total inner surface than Hölzl's threshold and still they getter very well. The reason of this phenomenon could be explained by different gettering mechanisms which accompany the oxygen precipitates. In order to explain this, the data of the samples annealed below 900 °C were separated from the rest. It was assumed that in the samples annealed below 900 °C the oxygen precipitates are free of dislocations, which is in the agreement with the STEM results, while in the rest of samples the oxygen precipitates are often accompanied by dislocations. As it can be seen in the figure, in the samples where the oxygen precipitates occur without dislocations the threshold value is in very well in agreement with the threshold of Hölzl. The shift of the threshold towards lower values of the normalized inner surface in the samples having oxygen precipitates with dislocations can be explained by a higher Cu getter efficiency of the dislocations

than of the oxygen precipitates. The same effect can be observed in the samples contaminated with Ni. In this case however, the results are not in agreement with Hölzl's threshold. This shows that the getter mechanism of Cu and Ni depends on the concentration of these impurities.

The reason why Hölzl et al. did not observe the shift of the threshold value of the normalized inner surface in their results could be the initial concentration of impurities. As it was mentioned above, they used a low concentration level while in this work the samples were contaminated with a very high concentration of impurities. Already STEM results for highly contaminated samples with Cu have shown that the metal precipitates at dislocations while in the case of a low initial Cu contamination Cu agglomerates at the edge of plate-like precipitates. This means that in the case of high contamination with Cu, Cu can be gettered by dislocations or by oxygen precipitates but in the case of oxygen precipitates the getter mechanism is weaker. Because, in the experiment carried out in this work the precipitates in the samples were accompanied with and without dislocations such shift of the threshold values of the normalized inner surface could be possible. For samples contaminated with a low concentration of Cu, only the getter mechanism based on the Cu aggregation at the edge of plate-like precipitates is active therefore in the results of Hölzl et al. only one value of the threshold of the normalized inner surface is observed.

The shift of S_{crit} was first reported in Refs. [Kot08, Kot09, Kis09]. In our next works, we tried to explain the shift of the S_{crit} considering the influence of vacancy supersaturation on the morphology of oxygen precipitates. In the first model, we considered different aspect ratios of oblate spheroids as possible morphologies of oxygen precipitates for samples pre-treated by RTA at different temperatures [Kis09, Kot09]. The different aspect ratios of a spheroid mean a different area of the oxygen precipitates and thus different getter efficiency of singular precipitates. Varying the aspect ratio of oblate spheroids, we were able to fit all the data in Fig. 67 to one threshold. However, oblate spheroids can be treated only as a simple model. In the reality mainly plate-like and octahedral precipitates can be found. Therefore, in the new model we assumed that the ratio between concentrations of plate-like precipitates and octahedral precipitates has an influence on the getter efficiency and on S_{crit} [Kot12]. Unfortunately not all results obtained in that model could be confirmed by STEM as it is in the model presented in this work, where the different getter efficiencies of oxygen precipitates and dislocations is considered.

6.4.4. Conclusions

We have generated different vacancy concentrations in Si wafers by RTA pre-treatment at different temperatures in order to investigate the influence of the vacancies on the getter efficiency of metallic impurities. The gettering efficiency of Cu, Ni and Pd for silicon wafers with different concentration of vacancies and interstitial oxygen atoms annealed at different temperatures and times was determined by haze getter test. In summary, the results demonstrated that:

1. By increasing the vacancy concentration, it is possible to achieve sufficient gettering of metal impurities at decreased temperatures. Wafers with a high concentration of vacancies induced by an RTA pre-treatment at 1250 °C can achieve significant getter efficiency already at lower temperature and shorter annealing time than wafers which were only pre-annealed at 1000 °C for 15 min.
2. The getter efficiency of Cu and Ni for samples contaminated with the metals up to their solubility limit at 900 °C is the same.
3. A Pd getter test can be a good reference test for the Cu and Ni getter efficiency in highly contaminated samples because the results of the getter efficiency are similar.
4. The value of S_{crit} is different for wafers annealed above and below 900 °C. This can be explained by two different getter mechanisms. Gettering by oxygen precipitates in samples without dislocations is weaker and S_{crit} is higher and gettering by dislocations is stronger leading to lower S_{crit} .

6.5. ToF-SIMS getter test

6.5.1. Introduction

Until now many getter tests for the investigation of the getter efficiency of Cu and Ni in samples contaminated with low concentration of the metals were developed. Most of them are based on contamination by spin coating. The concentration of metals is measured by ICP-MS or GF-AAS after dissolution of the silicon layers containing metal atoms by chemical etching [Sha96, Höl02, Sha03]. Although, the sensitivity of these getter tests is very high, they require a whole wafers for the tests and deliver the average the getter efficiency for the whole wafer. In this work, a getter test based on measurement of the surface concentration of the contaminant by ToF-SIMS is developed. The advantage of this test is the possibility to investigate many small samples of about 1 cm^2 from certain locations of the wafer simultaneously and the measurement time is very short.

So far, the SIMS method was mainly used for the investigation of the getter efficiency in the implanted samples. The aim of such investigations was to measure the concentration depth profile and to observe the site of metal aggregation in the implanted projection range [Won88, Gue00, Pee00]. The application of ToF-SIMS for the investigation of the metal concentration on the surface is much more difficult because of undesired surface effects which can influence the value of the measured concentration. This chapter first describes the development of a ToF-SIMS getter test, the problems which are associated with the measurement of the surface concentration and its limitations. In the second part of this chapter, the getter efficiency of oxygen precipitates is investigated by a 7 day storage getter test. The results will be compared with the literature and with the results of the haze getter test.

The principle of this test is based on a series of steps. The first step is the contamination of the samples with Cu in the range from $1 \times 10^{12} \text{ cm}^{-2}$ to $1 \times 10^{13} \text{ cm}^{-2}$ in a simple and quick way. The next step is the measurement of this concentration by means of ToF-SIMS in order to approve the initial concentration. Then, Cu is in-diffused into the silicon samples at $1000 \text{ }^\circ\text{C}$ for 10 min. This is the so-called drive-in step after which the Cu surface concentration is measured again in order to check if all Cu is diffused into the silicon bulk. After 7 day storage at room temperature, the Cu which is not getterred by bulk defects diffuses back to the surface. Comparing the Cu

concentration after 7 days with the initial surface concentration of Cu, the Cu getter efficiency can be determined. Annealing of the silicon sample contaminated with Cu at a temperature of 400 °C or lower would be a way to accelerate the out-diffusion of Cu from the silicon bulk and to save the days of storage. Such a treatment was also investigated. The process flow of the ToF-SIMS getter test is shown in Fig. 68.

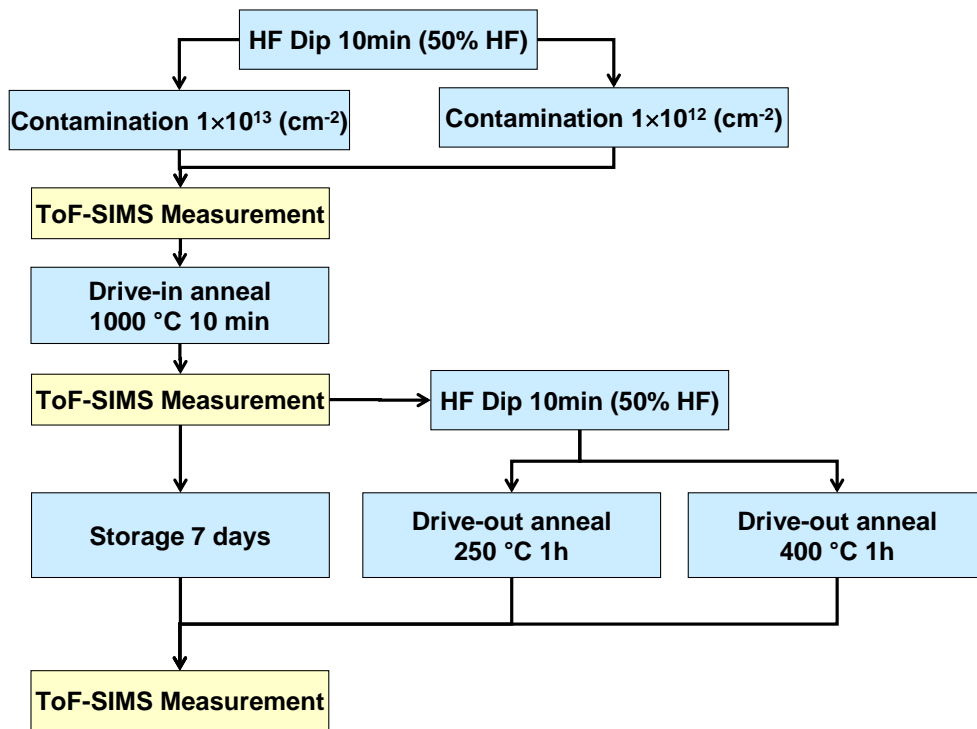


Figure 68: Process flow of the ToF-SIMS getter test.

6.5.2. Experimental details

For the development of ToF-SIMS 7 day storage getter test four types of samples were used. The first sample was cut out from a low O_i wafer. This sample was pre-treated by RTA at 1250 °C for 30 s and annealed at 800 °C for 32 h in N_2 . The second sample was cut out from a high O_i wafer. The third sample was cut out from an FZ wafer and the fourth from an n-type CZ wafer.

For the investigation of the getter efficiency in the samples contaminated with low concentration of Cu, both the low and the high O_i wafers were used. The samples were pre-treated by RTA at 1175 °C, 1200 °C, 1225 °C, and 1250 °C for 30 s and annealed at 800 °C for 1 h, 2 h, 4 h, 8 h, 16 h, or 32 h in N_2 . After that, the samples of the low O_i and the high O_i wafers were contaminated with Cu in the range of $1.0 \times 10^{13} \text{ cm}^{-2}$ and $5.0 \times 10^{12} \text{ cm}^{-2}$, respectively, and subjected to the ToF-SIMS 7 day storage getter test.

In order to investigate the influence of large oxygen precipitates on the BMD density some samples were subjected to an additional growth anneal and then investigated by the ToF-SIMS 7 day storage getter test.

6.5.3. Results and discussion

Development of the ToF-SIMS getter test

Contamination procedure

The first step of the getter test is the contamination of the silicon sample with a well defined concentration of impurities and the confirmation of this concentration by an analyzing technique like ToF-SIMS. In this getter test, pieces of Si wafers with an area of 1 cm × 1.3 cm were contaminated by dipping them in the contamination solution for 5 min. In order to contaminate the surface with $1 \times 10^{13} \text{ cm}^{-2}$ of Cu atoms, 70 μl of Cu standard solution (Cu 1000 ppm) were mixed with 1 l of H₂O. The pre-treatment of the sample surface plays a very important role for the measurement of the Cu concentration by ToF-SIMS. The measurement of the Cu concentration on the silicon surface is very sensitive to a native oxide therefore it is important to dip the sample in an HF solution before contamination. The relative sensitivity factor (RSF) of Cu which is used to calibrate the concentration measured is different for different materials [Har11]. This means that the amount of ejected ions can be different for silicon surfaces with oxide and without oxide layer. Fig. 69 shows the results of three samples contaminated with Cu by dipping the samples in the same Cu contamination solution. The first sample was annealed in oxygen atmosphere at 1000 °C to generate an oxide layer. The second sample was first dipped in an HF (5%) solution for 10 min and then subjected to a hydrophilization treatment in a NH₄OH:H₂O₂:H₂O (1:1:5) solution for 5 min. The third sample was hydrophobized in HF (50%) solution for 10 min. The concentrations determined by ToF-SIMS differ by orders of magnitude as demonstrated in Fig. 69. In the sample with an oxide, the very low concentration of Cu is caused by the matrix effect. This means that the RSF factor of Cu in silicon is no more valid in this kind of sample. In the sample subjected to a hydrophilization, some matrix effect can also take place therefore the concentration is smaller than in the third hydrophobized sample where the concentration is reliable.

In many getter tests, the contamination is based on hydrophilization solutions which can be helpful in the homogenous distribution of metals on the silicon surface especially for spin-on contamination [Iso02]. However, as it was just demonstrated the hydrophilization pre-treatment can be of negative influence on the concentration measurement by ToF-SIMS.

An initial Cu concentration of $1 \times 10^{12} \text{ cm}^{-2}$ can be obtained if 35 μl of Cu standard solution is mixed with 1 l of H_2O is twice diluted in H_2O with a ratio of 0.1 : 0.9. The concentration measurement by ToF-SIMS is carried out according to chapter 4.5. The detection limit of the measurement of the Cu concentration on the silicon surface by this detection technique was about $1 \times 10^{10} \text{ cm}^{-2}$.

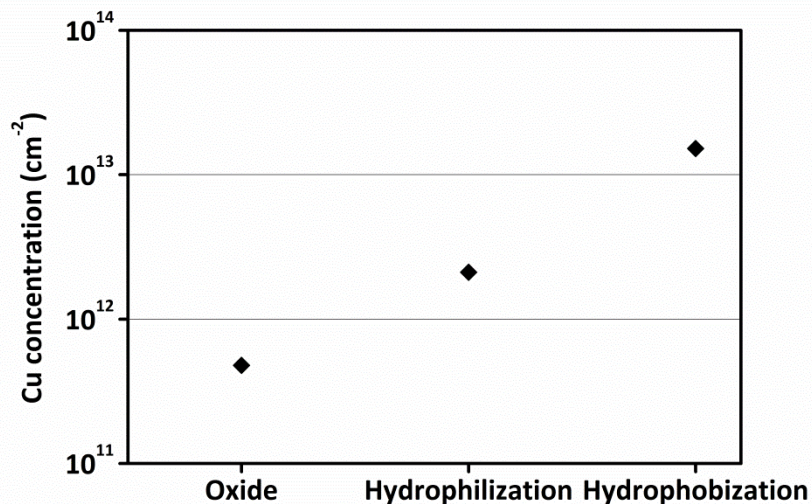


Figure 69: Cu concentration measured on three different pre-treated samples for samples contaminated with $1 \times 10^{13} \text{ cm}^{-2}$ of Cu atoms.

Drive-in anneal and storage

After contamination, the samples are annealed at 1000 °C for 10 min in N_2 in order to in-diffuse the Cu into the Si bulk. As the result of this drive-in anneal, the concentration of Cu on the surface of the sample decreases and the Cu getter efficiency was found to be above 90% in any kind of sample. It is impossible to measure a correct getter efficiency at this point, because after 7 days of storage at RT most of the ungettered Cu diffuses out of the bulk and returns to the samples surface. A similar effect was observed by [Sha96]. If most of the Cu is gettered by defects the getter efficiency

remains above 90% even after 1 month. In this case Cu is permanently trapped at getter sites.

Drive-out

In order to accelerate the out-diffusion of ungettered Cu from the Si bulk and to make the getter test faster, an annealing step at temperatures higher than RT can be applied as reported by [Sha96]. Oxide layers at the samples, exceeding 3 nm must be removed before out-diffusion because otherwise Cu will not out-diffuse [Sha96, Hoz02]. One hour of annealing at 400 °C should be long enough to remove more than 90% of Cu from p-type wafers [Sha96]. However, the results obtained in this work are opposite as shown in Fig. 70. The getter efficiencies of as-grown samples (p-type CZ, FZ, and n-type CZ) subjected to a 7 day storage test are much lower than in the similar samples subjected to a drive-out anneal at 400 °C and 250 °C for 1 h. Even after 7 days, Cu atoms did not diffuse out of the samples subjected to the drive-out step. This means that the Cu remains in the bulk of the samples subjected to a drive-out anneal while in the samples subjected to a 7 seven day storage test a large part of the Cu diffuses-out of the bulk. Pleas note that before the drive-out anneals the oxide layer was removed (Fig. 68). The sample indicated by R is a referential sample which exhibits high gettering efficiency.

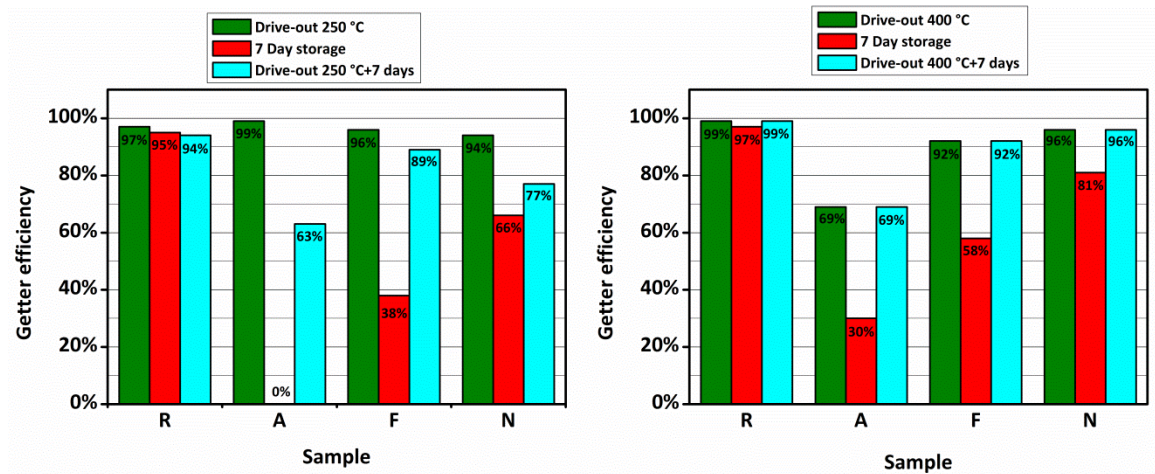


Figure 70: Comparison of the results from a 250 °C or 400 °C drive-out tests and from a 7 day storage test. The initial Cu concentration was $\approx 1 \times 10^{12} \text{ cm}^{-2}$. R – CZ samples with high BMD density, A - CZ as-grown p-type, F - FZ p-type, N - CZ as-grown n-type.

The reason why Cu does not diffuse out of the Si bulk is illustrated in Fig. 71 where the images of preferentially etched as-grown samples are shown after drive-out anneal. On all the samples subjected to a drive-out anneal, characteristic etch pits of Cu precipitates were detected no matter if the initial concentration of Cu was $1 \times 10^{12} \text{ cm}^{-2}$ or $1 \times 10^{13} \text{ cm}^{-2}$. In case of the sample subjected to 7 day storage test, no etch pits were found. These results mean that the drive-out anneals cannot be used to accelerate the out diffusion of Cu because the Cu precipitates during the drive-out anneal. However, if the sample is stored at RT the Cu atoms can easily diffuse out. Therefore only the 7 day storage test can be used for the determination of the getter efficiency.

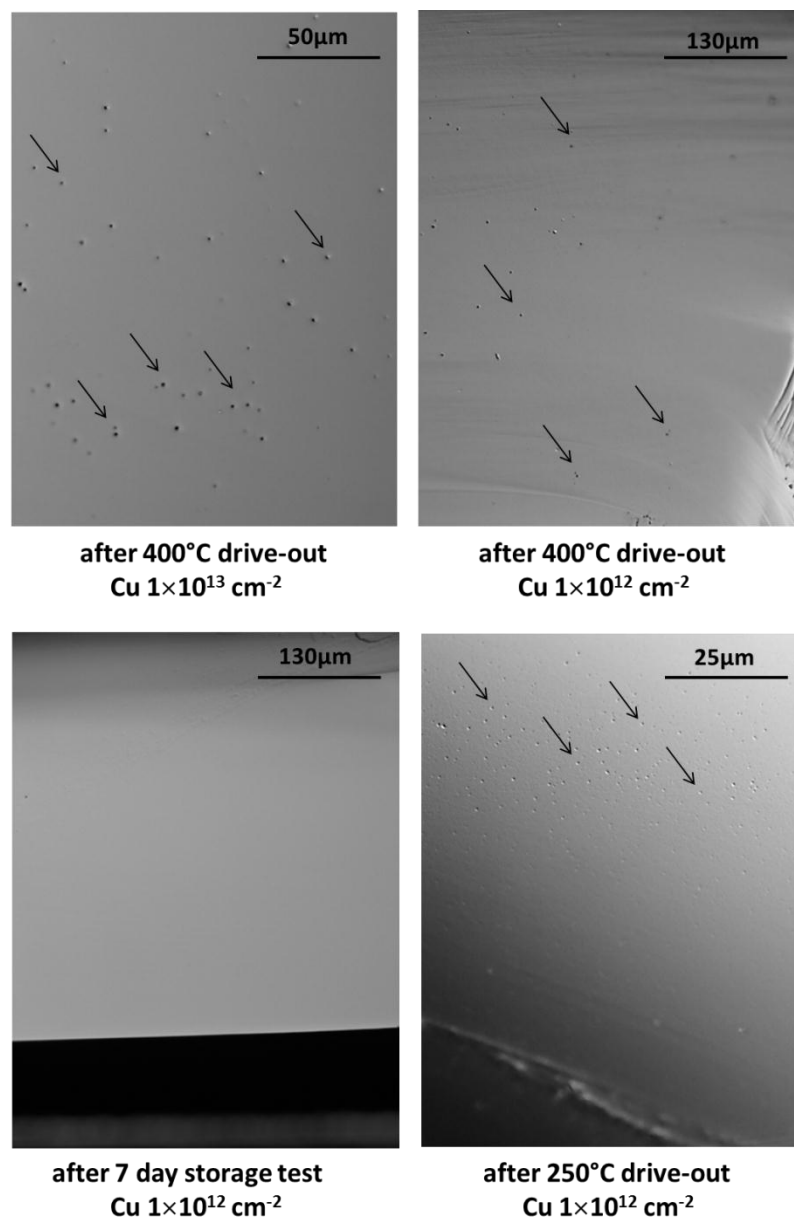


Figure 71: CZ as-grown sample subjected to a drive-out anneal or a 7 day storage test etched by the Secco etchant. Arrows indicate some of the etch pits of Cu precipitates.

Cu getter efficiency

Now, the 7 day storage test was used for the investigation of the getter efficiency. The getter efficiency was determined according to equation

$$\eta_{7day} = \left(1 - \frac{Cu_{In}}{Cu_{Ref}}\right) \cdot 100\% \quad (43)$$

where, Cu_{In} is the concentration of Cu measured on the surface of the sample after 7 day storage at RT and Cu_{Ref} is the concentration of Cu measured on the surface of the sample after the contamination.

The results of the 7 day storage getter test are shown in Fig. 72. In the samples annealed for 8 h sufficient gettering of metal impurities occurs already at 800 °C for wafers pre-treated by RTA at 1225 °C. In case of samples annealed for 4 h, sufficient gettering appears only at 1000 °C for the wafer pre-treatment by RTA at 1250 °C. It is clear that the samples contaminated with low Cu concentration require an RTA pre-treatment at a higher temperature compared to the samples contaminated with a high Cu concentration. These results show that the getter efficiency depends on the initial Cu concentration. Such an effect was already observed in the past [Iso02, Web02]. These results also mean that for Cu gettering in the samples contaminated with low Cu concentration the density of precipitates is a very important factor.

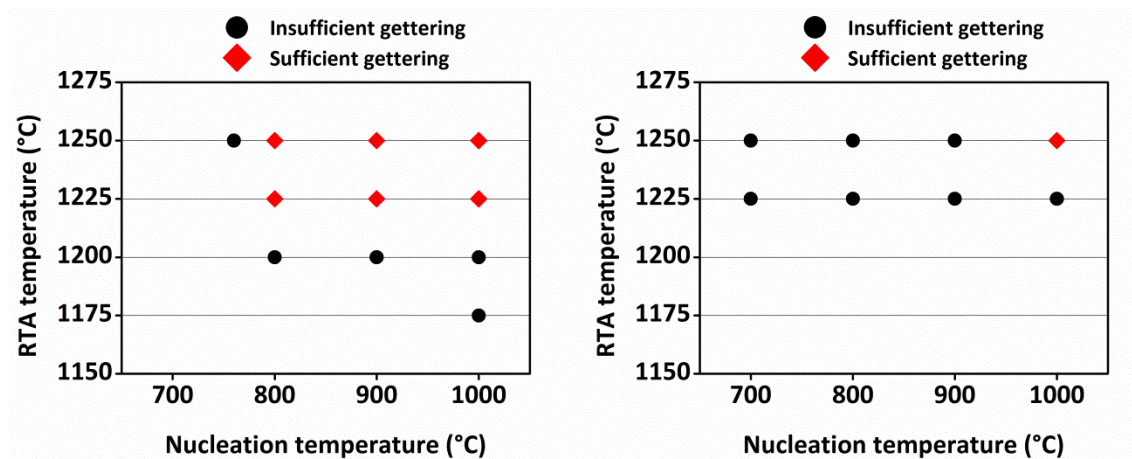


Figure 72: Cu gettering determined by the 7 day storage getter test shown for different nucleation temperatures and different temperatures of the RTA pre-treatment. The samples were annealed for 8 h (left) or 4 h (right) at the nucleation temperatures. Insufficient gettering is marked by black circles and sufficient gettering by red diamonds. The initial Cu concentration was $\approx 1 \times 10^{13} \text{ cm}^{-2}$.

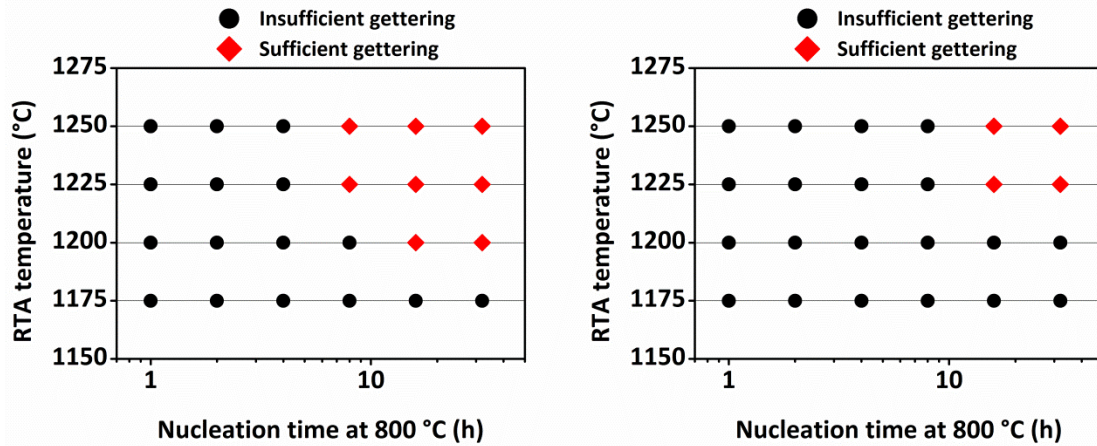


Figure 73: Cu gettering determined by the 7 day storage getter test shown for different nucleation times at 800 °C and different temperatures of the RTA pre-treatment for samples with low O_i (left) or high O_i (right). Insufficient gettering is marked by black circles and sufficient gettering by red diamonds. The initial Cu concentration was $\approx 1 \times 10^{13} \text{ cm}^{-2}$ and $\approx 5.0 \times 10^{12} \text{ cm}^{-2}$ for low O_i and high O_i wafers, respectively.

Fig. 73 shows a comparison of the results between the samples containing low and high concentration of interstitial oxygen. It is clearly seen that in the samples with low O_i concentration a getter efficiency of $\geq 90\%$ can be achieved in most cases after shorter nucleation time than in the samples with a high concentration of interstitial oxygen. However, the initial concentration of Cu contamination was twice smaller in the samples with high O_i compared to the samples with low O_i where the initial Cu concentration was $1 \times 10^{13} \text{ cm}^{-2}$. The density of oxygen precipitates in the samples with high O_i was lower compared to the samples with low O_i . This could have influenced the results of the getter efficiency. The reason for the different initial Cu concentrations is unknown and was unintended. The different concentrations of the BMDs for the corresponding sets of heat-treatment for the low and high O_i samples was assumed to be caused by the different B concentration (see chapter 6.1.2). This is an additional factor that could have influenced the getter efficiency. In spite of the slightly different results of the getter efficiency in terms of the sample treatment, the getter efficiency of the singular precipitates does not differ at all as shown in the plots in Fig. 74. The threshold values of the normalized inner surface are the same for samples with low and high O_i and they are in a good agreement with Hölzl's threshold for Cu. In this figure, the data of the samples subjected to a two step anneal (nucleation and growth followed by RTA) are also included. The oxygen precipitates in these samples are very large exceeding 200 nm. They are associated with many punched-out dislocations and stacking faults which are very good getter sites in case of high Cu contamination [She94]. Nevertheless,

if the Cu concentration is lower than $\sim 1 \times 10^{13} \text{ cm}^{-2}$, the S_{crit} of the total inner surface is not higher than Hölzl's threshold for Cu what means that the dislocations and stacking faults do not play a significant role in the gettering of Cu atoms as it was in the case of a high initial concentration of Cu.

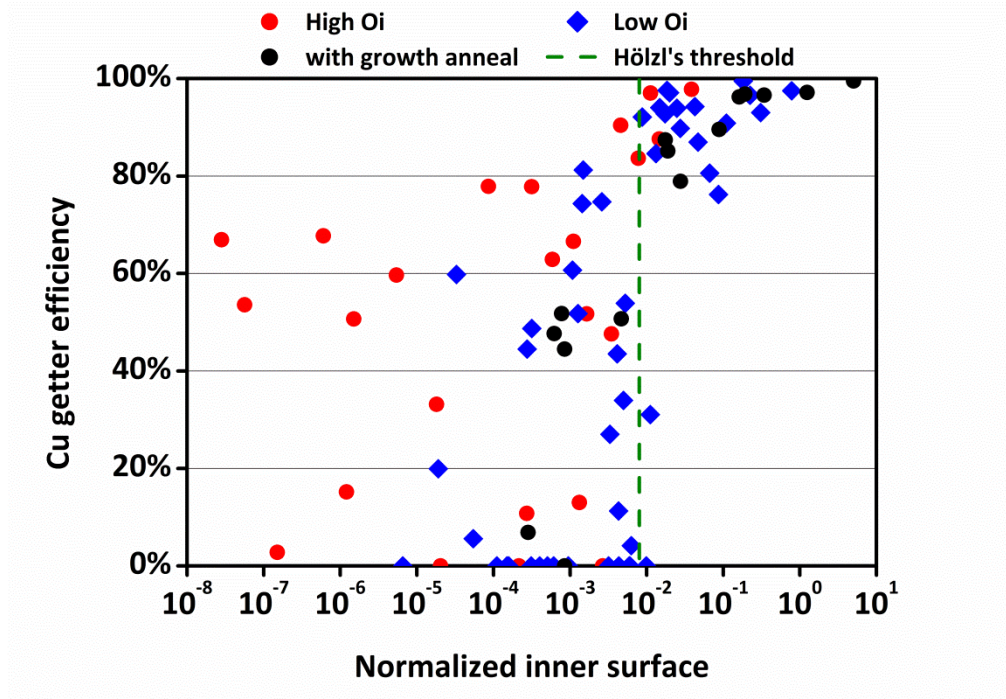


Figure 74: Cu getter efficiency as a function of the normalized inner surface. All samples were pre-treated by RTA in the temperature range between 1250 °C and 1175 °C.

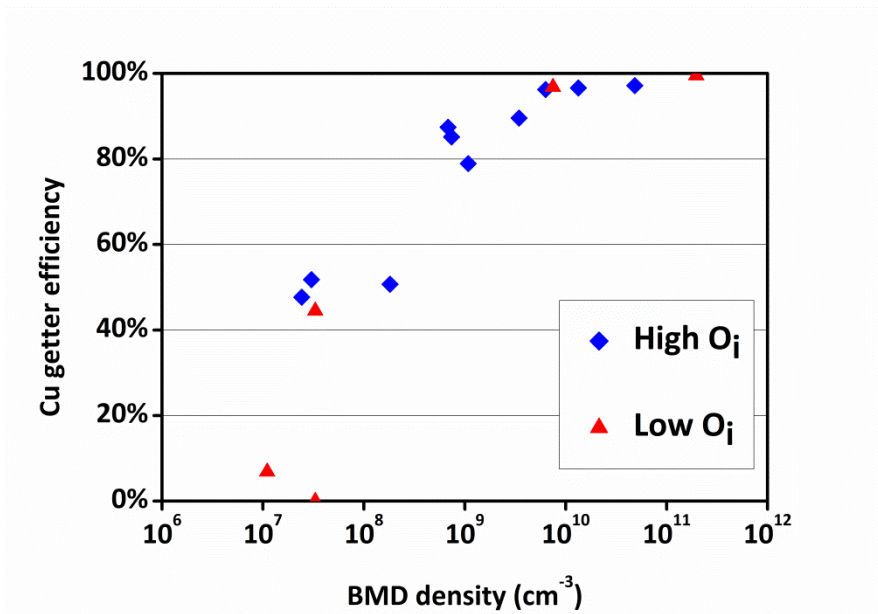


Figure 75: Cu getter efficiency as a function of the BMD density for oxygen precipitates of nearly equal size. The initial concentration of Cu was $\approx 1 \times 10^{13} \text{ cm}^{-2}$.

Fig. 75 shows the Cu getter efficiency as a function of the BMD density for samples subjected to a growth anneal at 1000 °C for 16 h. Such samples are characterized by large oxygen precipitates with comparable size accompanied by secondary defects like punched-out dislocations and stacking faults. The different density of the defects was achieved by an RTA pre-treatment of the samples at various temperatures which were subsequently annealed at various nucleation temperatures. The getter efficiency increases with an increasing density of defects and saturates at a value of $6 \times 10^9 \text{ cm}^{-3}$. This value is in a good agreement with the values obtained in Ref. [Web02] and about one order of magnitude higher than the value obtained by Isomae et al. [Iso02]. The reason why Isomae et al. observed efficient Cu gettering by a BMD density of $5 \times 10^8 \text{ cm}^{-3}$ could be that it was a different type of getter test. They contaminated the back surface of the samples and after an in-diffusion step at 1000 °C for 5 min by using RTA, they measured the Cu concentration on the front surface. By comparing the concentration of Cu on the surface with the referential concentration they determined getter efficiency. The high getter efficiency achieved for a low BMD density could be the results of the Cu measurement carried out directly after in-diffusion step. As it was observed in this work Cu needs much more time to diffuse out from the Si bulk. A high getter efficiency of about 90 % in the samples directly after the drive-in step was always observed but after 7 day storage it decreased far below 90%.

Going back to the work of Weber et al., they have shown that Cu gettering at the surface of the oxygen precipitates can be explained by Ham's law assuming that only 10% of the surface of oxygen precipitates can getter copper. This would be in good agreement with the hypothesis that the getter site is located at the edge of plate-like precipitates because of tensile strain of the Si matrix located there. If the plat-like precipitates grow with an aspect ratio of 0.06, the site area calculated according to Eqs. (28) and (29) equals about 10% of the total area.

Fig. 76 shows the dependence of the getter efficiency on the length and density of oxygen precipitates. The dashed lines in the figure represent the threshold of efficient gettering of Ni from Sueoka [Sue00]. This threshold was in good agreement with the results obtained for the samples contaminated with high concentration of Cu but only for BMD densities up to about $1 \times 10^{10} \text{ cm}^{-3}$ (Fig. 66). However, here the getter efficiencies of the samples with BMD densities below $1 \times 10^{10} \text{ cm}^{-3}$ do not agree with Sueoka's threshold. The samples having a BMD density higher than $1 \times 10^{10} \text{ cm}^{-3}$ getter sufficiently but only if a certain length of plate-like precipitates is achieved. This is a

similar effect which can be observed in the samples contaminated with high concentration of Cu as it is shown in Fig. 66. The differences between the results of the Cu getter efficiency in the samples contaminated with high and low concentration of Cu mean that the length of the oxygen precipitates is only important for samples contaminated with high Cu concentration. Additionally, in both cases, in the samples contaminated with low and high concentrations of Cu, the precipitates must achieve a certain size to be able to getter Cu atoms. These results are another prove of the assumption that in the samples contaminated with a high concentration of Cu, punched-out dislocations, stacking faults and oxygen precipitates serve as getter sites for Cu while in the samples contaminated with low concentration of Cu only oxygen precipitates act as getter centers for Cu atoms.

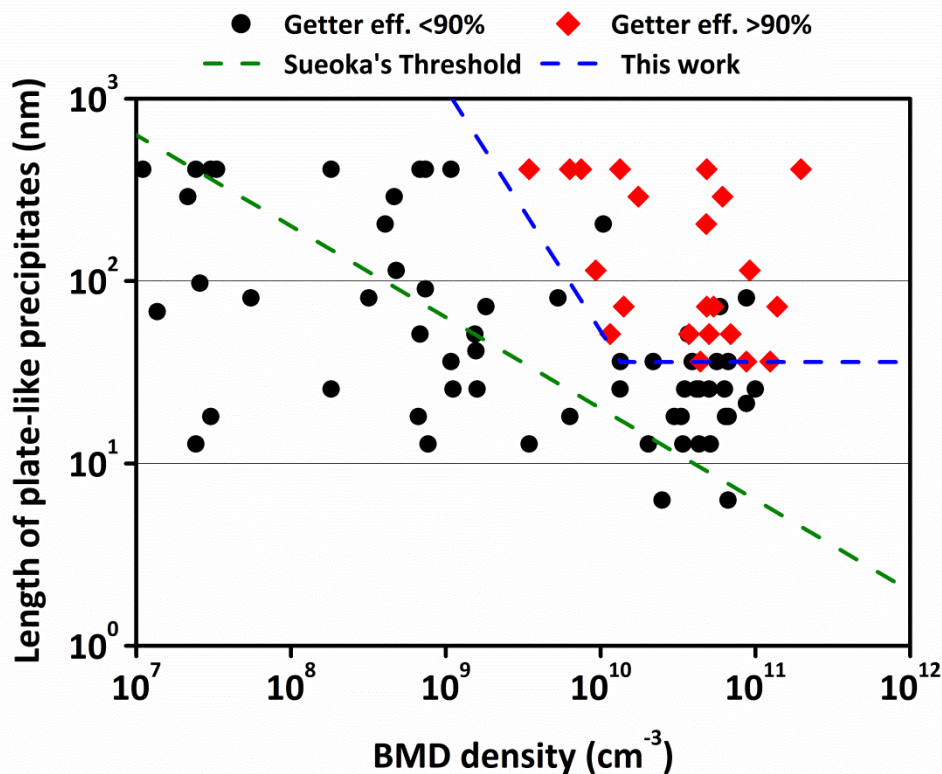


Figure 76: Cu getter efficiency shown for different lengths of plate-like precipitates and the corresponding BMD densities.

6.5.4. Conclusions

In this chapter the development of a 7 day storage getter test was presented. By means of the 7 day getter test, the getter efficiency in the samples contaminated with low concentration of Cu was determined. The results were compared to the results of other

authors and the results of the haze getter test. The development of the getter test and the results of the getter test carried out on the samples contaminated with low concentration of Cu have shown that:

1. The contamination step requires pre-treatment in HF (50%) solution for reliable Cu concentration measurements by ToF-SIMS.
2. The detection limit of the Cu concentration measurement by ToF-SIMS on Si substrates equals $1 \times 10^{10} \text{ cm}^{-2}$.
3. Directly after the drive-in step, most of the Cu remains in the Si bulk.
4. After 7 day storage at RT most of the ungettered Cu atoms diffuses out of the bulk. After this step it is possible to distinguish the samples with sufficient gettering from samples with insufficient gettering.
5. Cu out-diffusion cannot be accelerate by an out-diffusion anneal at 250 °C or 400 °C for Cu contamination levels of $1 \times 10^{12} \text{ cm}^{-2}$ and $1 \times 10^{13} \text{ cm}^{-2}$ because Cu precipitates during these anneals.
6. The Cu getter efficiency depends on the initial contamination level. In samples contaminated with higher Cu concentration, Cu is gettered better than in samples contaminated with lower contamination of Cu.
7. By increasing the vacancy concentration by RTA pre-treatments, it is possible to achieve sufficient gettering of metal impurities at lower temperatures.
8. The critical values of the normalized inner surface in the samples with the low and high O_i agree with Hölzl's threshold. The critical values of the normalized inner surface in the samples with large precipitates accompanied with punched-out dislocations and stacking faults also agree with Hölzl's threshold.
9. The getter site of Cu in samples contaminated with low Cu concentration is located at the edge of plate-like precipitates. The punched-out dislocations and stacking faults do not play significant role in the gettering of Cu in case of low initial Cu concentration.
10. The BMD density of about $6 \times 10^9 \text{ cm}^{-3}$ corresponds to a critical concentration of large oxygen precipitates required for efficient gettering of Cu. Decreasing the size of the precipitates this concentration increases to about $1 \times 10^{10} \text{ cm}^{-3}$. For very small oxygen precipitates even a BMD density of about $1 \times 10^{11} \text{ cm}^{-3}$ does not ensure sufficient gettering of Cu.

7. Summary and conclusions

RTA pre-treatment is one of the methods allowing control of the point defect formation in the silicon wafers which are important in terms of oxygen precipitation and gettering of metal impurities.

This work provides new information about the influence of vacancies introduced by RTA on the precipitation of oxygen in silicon and the morphology, size, and getter ability of oxygen precipitates. In order to obtain this information, techniques like preferential etching, STEM, FTIR, and ToF-SIMS were used.

Investigations of the nucleation of oxygen precipitates in vacancy-rich samples have shown that the concentration of vacancies has an influence on the concentration of oxygen precipitates. For increasing concentration of vacancies, the concentration of the oxygen precipitates is increasing. This influence of the vacancies on the oxygen precipitation can be explained by considering the total free energy of formation of a nucleus where the increase of the concentration of vacancies causes a decrease of the critical radius of nuclei whereby more precipitates can grow at higher temperatures. Annealing of vacancy-rich samples leads to the appearance of three peaks in the nucleation curves. The two low temperature peaks located at 450 °C and 650 °C are also observed in homogenized samples while the peak at 800 °C can be seen only in RTA pre-treated samples. Based on the classical nucleation theory combined with ab initio calculations, the origin of the maxima can be explained by three types of nuclei. The peaks at 450 °C and 650 °C can be simulated using the coherent oxygen mono-layers $(O_i)_2-p1$ and the oxygen double-layers $(O_i)_2-p2$ both belonging to the so-called seed oxides which were obtained by ab initio calculation and do not exist as independent oxide phases. These nuclei are vacancy independent nuclei therefore the best fit can be obtained for the samples containing low concentration of vacancies. The peak at 800 °C can be well simulated using the coherent mono-layered VO_2 agglomerates as nucleation centers of the oxygen precipitates. This kind of nuclei is vacancy dependent.

Extended investigations carried out on the morphology and size of the oxygen precipitates by STEM have shown that the supersaturation of vacancies in the samples annealed at 800 °C leads to the formation of 3 dimensional or 2 dimensional dendrites. The driving force for the formation of dendrites at this temperature is the high supersaturation of the interstitial oxygen and the supersaturation of vacancies having

influence on the morphology of oxygen precipitates at the beginning of the growth. Although, dendritic the precipitates were already observed in the past in samples annealed at 1000 °C it is clear that the dendrites observed in this work are very different. The main difference is their ability to form three dimensional dendrites.

The size of the dendrites is independent of the vacancy supersaturation and their growth rate is a linear function of the growth. Some 3D dendrites were found also in the samples annealed at 900 °C but at this temperature the plate-like precipitates are the dominant morphology of the oxygen precipitates. Moreover, at 900 °C the octahedral precipitates and after sufficiently long annealing time also large 2D dendrites can be found. For extending the time of annealing at 1000 °C, the octahedral precipitates become the main morphology. This temperature promotes also the plate like-precipitates and the large dendritic plate-like precipitates but their densities are lower than the density of the octahedral precipitates. The size of the plate-like and octahedral precipitates can be fitted by diffusion limited equations taking into account the impact of the density of the oxygen precipitates which has an influence on the rate of consumption of the interstitial oxygen.

In samples contaminated with low concentration of Cu, it was found that Cu agglomerates at the edges of plate-like or dendritic precipitates. At the edge of plate-like or dendritic precipitates, the silicon lattice is tensile strained what can explain this gettering phenomenon. In the samples with high concentration of Cu, further growth of Cu precipitates occurs by a repeated nucleation process on climbing edge dislocations.

The STEM investigation provided important information became a basis for the correct deconvolution of the low temperature FTIR spectra measured on the samples containing oxygen precipitates. It was found that the peak at 1040 cm^{-1} belongs to dendritic precipitates or needle-like precipitates. Moreover, the peaks at 1101 cm^{-1} and 1229 cm^{-1} are the TO and LO modes of plate-like precipitates, respectively. These are important findings because the broad peak at 1101 cm^{-1} was often wrongly considered to be originated from spherical precipitates. Indeed, the peaks of octahedral and truncated octahedral precipitates are located at the position of the TO mode of the plate-like precipitates but they are sharp and precisely located at 1095 cm^{-1} and 1115 cm^{-1} , respectively.

Finally, gettering of metal impurities was investigated for high concentrations of Cu, Ni or Pd and for low concentrations of Cu. For the experiments with high concentration of impurities, the well known haze getter test was used. In order to investigate the

gettering of Cu in samples contaminated with low concentration, the ToF-SIMS getter test based on the unconstrained out-diffusion of Cu was developed. The results have shown that the getter efficiency can be improved by increasing the concentration of vacancies before annealing for both the highly and the lowly contaminated samples. Moreover, efficient gettering is limited by the size of the oxygen precipitates. On the one hand, below a certain size, even for a high density of oxygen precipitates, efficient gettering cannot be achieved. On the other hand, if the density of the oxygen precipitates is too low, independent on the size of precipitates, efficient gettering will not occur. Additionally, it was found that two sinks for gettering of metals exist in our samples, oxygen precipitates and dislocations. The gettering of metal impurities at the dislocations is stronger in samples contaminated with high concentration of metals. In case of low concentration of Cu, gettering at dislocations is less important and oxygen precipitates become the main getter sink for Cu.

8. Scientific visibility

8.1. Publications list

1. The Role of Vacancies and Oxygen for Setting up an Efficient Getter for Cu and Ni in Silicon Wafers
D. Kot, G. Kissinger, W. Häckl, A. Sattler, W. von Ammon
ECS Transactions 16, 207 (2008)
2. Comparison of Evaluation Criteria for Efficient Gettering of Cu and Ni in Silicon Wafers
D. Kot, G. Kissinger, A. Sattler, W. von Ammon
ECS Transactions 25, 67 (2009)
3. Impact of RTA on the Morphology of Oxygen Precipitates Investigated by FTIR Spectroscopy and TEM and on the Getter Efficiency for Cu and Ni in Silicon Wafers Investigated by Haze Tests
D. Kot, G. Kissinger, M.A. Schubert, T. Müller, A. Sattler, Materials Science Forum Vol. 725, 239 (2012)
4. Characterization of Deep Levels Introduced by RTA and by Subsequent Anneals in n-Type Silicon
D. Kot, T. Mchedlidze, G. Kissinger, W. von Ammon,
ECS Transactions 50, 269 (2012)
5. Characterization of Deep Levels Introduced by RTA and by Subsequent Anneals in n-Type Silicon
D. Kot, T. Mchedlidze, G. Kissinger, W. von Ammon,
ECS J. Solid State Sci. Technol., 2(1) , P9-P12 (2013)
6. Analysis of the Nucleation Kinetics of Oxide Precipitates in Czochralski Silicon
G. Kissinger, **D. Kot**, J. Dabrowski, V.D. Akhmetov, A. Sattler, W. von Ammon
Proc. 5th International Symposium on Advanced Science and Technology of Silicon Materials, JSPS (2008), p.39
7. Analysis of the Nucleation Kinetics of Oxide Precipitates in Czochralski Silicon
G. Kissinger, **D. Kot**, J. Dabrowski, V.D. Akhmetov, A. Sattler, W. von Ammon
ECS Transactions 16, 97 (2008)
8. Advances in the Understanding of Oxide Precipitate Nucleation in Silicon
G. Kissinger, **D. Kot**, V. Akhmetov, A. Sattler, T. Müller, W. von Ammon
ECS Transactions 18, 995 (2009)
9. Getter effects in low oxygen and high oxygen Czochralski silicon wafers
G. Kissinger, **D. Kot**, W. Häckl
ECS Transactions 33(11), 113 (2010)

10. Modeling the early stages of oxygen agglomeration
G. Kissinger, J. Dabrowski, **D. Kot**, V.D. Akhmetov, A. Sattler, W. von Ammon
ECS Transactions 27(1), 1021 (2010)
11. Rate equation modeling, ab initio calculation, and high sensitive FTIR investigations of the early stages of oxide precipitation in vacancy-rich CZ silicon
G. Kissinger, J. Dabrowski, V.D. Akhmetov, A. Sattler, **D. Kot**, W. von Ammon
Solid State Phenomena 156-158, 211 (2010)
12. Delineation of microdefects in silicon substrates by chromium-free preferential etching solutions and laser scattering tomography
M. Pellowska, D. Possner, **D. Kot**, G. Kissinger, B.O. Kolbesen
Solid State Phenomena 156-158, 443 (2010)
13. Initial stages of oxygen and vacancy agglomeration: kinetic and getter effects
G. Kissinger, **D. Kot**, J. Dabrowski, W. Häckl, V.D. Akhmetov, A. Sattler
Proc. 6th Forum of the Science and Technology of Si Materials, 36 (2010)
14. Modeling the early stages of oxygen agglomeration in silicon
G. Kissinger, J. Dabrowski, **D. Kot**, V.D. Akhmetov, A. Sattler, W. von Ammon
J. Electrochem. Soc. (c) 158, H343 (2011)
15. Comparison of the impact of thermal treatments on the second and on the millisecond scales on the precipitation of interstitial oxygen
G. Kissinger, **D. Kot** and W. von Ammon,
ECS J. Solid State Sci. Technol, 1 (6), P269-P275 (2012)

8.2. Own presentations at conferences

1. The Role of Vacancies and Oxygen for Setting up an Efficient Getter for Cu and Ni in Silicon Wafers
D. Kot, G. Kissinger, W. Häckl, A. Sattler, W. von Ammon
High Purity Silicon X at PRiME 2008, October 12-17, 2008, Honolulu, Hawaii, USA
2. Comparison of Evaluation Criteria for Efficient Gettering of Cu and Ni in Silicon Wafers
D. Kot, G. Kissinger, A. Sattler, W. von Ammon
216th ESC Meeting, Oct. 4-9, 2009, Vienna, Austria
3. Advances in the Understanding of Oxide Precipitate Nucleation in Silicon
G. Kissinger, **D. Kot**, V. Akhmetov, A. Sattler, T. Müller, W. von Ammon
E-MRS Spring Meeting 2009, Symposium I, Strasbourg, France, June 08-12, 2009- Poster presentation
4. Evaluation criteria for efficient gettering applied for Cu and Ni impurities in Si wafers
D. Kot, G. Kissinger M. A. Schubert, A. Sattler, W. von Ammon

GADEST 2009, Sept. 26 - Oct. 2, 2009, Doellnsee-Schorfheide, Germany –
Poster presentation

5. Advances in the understanding of oxide precipitate nucleation in silicon
D. Kot, G. Kissinger, V. Akhmetov, A. Sattler, T. Müller, W. von Ammon
Punktdefekttreffen, March 27, 2009, Dresden, Germany
6. Comparison of Cu getter efficiency for silicon wafers contaminated with low and high concentrations of Cu atoms
D. Kot, G. Kissinger, I. Costina, A. Sattler, T. Müller
218th Electrochemical Society Meeting, High Purity Silicon XI, Las Vegas, October 10 - 15, 2010, USA
7. Impact of RTA on the Morphology of Oxygen Precipitates Investigated by FTIR Spectroscopy and TEM and on the Getter Efficiency for Cu and Ni in Silicon Wafers Investigated by Haze Tests
D. Kot, G. Kissinger, M.A. Schubert, T. Müller, A. Sattler
14th Intern. Conference on Defects - Recognition, Imaging and Physics in Semiconductors (DRIP-14), Sept. 25-29, 2011, Miyazaki, Japan
8. Impact of RTA on the morphology of oxygen precipitates investigated by FTIR spectroscopy and TEM and on the getter efficiency for Cu and Ni in silicon wafers investigated by haze tests
D. Kot, G. Kissinger, M.A. Schubert, T. Müller, A. Sattler
48. Punktdefekttreffen, Oct. 13-14, 2011, Dresden, Germany
9. Characterization of Deep Levels Introduced by RTA and by Subsequent Anneals in n-Type Silicon
D. Kot, T. Mchedlidze, G. Kissinger, W. von Ammon
222th Electrochemical Society Meeting, High Purity Silicon XII, Honolulu, October 7 - 12, 2012, USA

Bibliography

- [Aka02] M. Akatsuka, M. Okui, K. Sueoka, *Nucl. Instr. and Meth. In Phys. Res. B*, **189**, 46 (2002).
- [Akh09] V. Akhmetov, G. Kissinger, and W. von Ammon, *Appl. Phys. Lett.*, **94**, 092105 (2009).
- [And10] A. Andrianakis, C. A. Londos, A. Misiuk, V. V. Emtsev, G. A. Oganessian, H. Ohyama, *Solid State Phenom.*, **156-158**, 123 (2010).
- [Aok93] S. Aoki, *Materials Transactions*, **34**, 746 (1993).
- [Bea71] A. R. Bean and R. C. Newman, *J. Phys. Chem. Solids*, **32**, 1211 (1971).
- [Ber89] W. Bergholz, M. J. Binns, G. R. Booker, J. C. Hutchison, S. H. Kinders, S. Messoloras, R. C. Newman, R. J. Stewart, J. G. Wilkes, *Phil. Mag. B*, **59**, 499 (1989).
- [Ber94] W. Bergholz, *Semiconductors and Semimetals*, **42**, 513 (1994).
- [Bin96] M. J. Binns, C. A. Londos, S. A. McQuaid, R. C. Newman, N. G. Semaltianos, J. H. Tucker, *J. Mater. Sci. Mater. Electron.*, **7**, 347 (1996).
- [Bor00] A. Borghesi, A. Sassella, P. Geranzani, M. Porrini, B. Pivac, *Mater. Sci. Eng. B*, **73**, 145 (2000).
- [Bor92] A. Borghesi, A. Piaggi, A. Sassella, A. Stella, and B. Pivac, *Phys. Rev. B*, **46**, 4123 (1992).
- [Bre06] D. A. Brett, D. J. Llewellyn, M. C. Ridgway, *Nucl. Instrum. Methods Phys. Res. B*, **242**, 576 (2006).
- [Bro87] S. D. Brotherton, J. R. Ayres, A. Gill, H. W. van Kesteren, F. J. A. M. Greidanus, *J. Appl. Phys.*, **62**, 1826 (1987).
- [Bro94] R. A. Brown, D. Maroudas, and T. Sinno, *J. Cryst. Growth*, **137**, 12 (1994).
- [Cla87] M. Claybourn and R. C. Newman, *Appl. Phys. Lett.*, **51**, 2198 (1987).
- [Cor64] J. W. Corbett, R. S. McDonald, and G. D. Watkins, *J. Phys. Chem. Solids*, **25**, 873 (1964).
- [Cra81] R. A. Craven, in *Semiconductor Silicon 1981*, edited by H. R. Huff and R. J. Kriegler (The Electrochemical Society, Pennington, NJ, 1981), p. 254.
- [Cui08] C. Cui, D. Yang, X. Ma, M. Li, *J. Appl. Phys.*, **103**, 064911 (2008).
- [Deg02] O. De Gryse, P. Clauws, J. Van Landuyt, O. Lebedev, C. Claeys, E. Simoen, and J. Vanhellefont, *J. Appl. Phys.*, **91**, 2493 (2002).

- [Deg03] O. De Gryse, J. Vanhellefont, P. Clauws, O. Lebedev, J. Van Landuyt, E. Simoen, C. Claeys, *Physica B*, **340-342**, 1013 (2003).
- [Deg04] O. De Gryse, P. Clauws, J. Vanhellefont, O. I. Lebedev, J. Van Landuyt, E. Simoen, C. Claeys, *J. Electrochem. Soc.*, **151**, G598 (2004).
- [Fal04] R. J. Falster, V. V. Voronkov, V. Y. Resnick, M. G. Milvidskii, *Electrochem. Soc. Proc.*, **5**, 188 (2004).
- [Fal05] R. J. Falster, V. V. Voronkov, V. Y. Resnick, M. G. Milvidskii, *Solid State Phenom.*, **108**, 97 (2005).
- [Fal91] R. J. Falster, G. R. Fisher, and G. Ferrero, *Appl. Phys. Lett.*, **59**, 809 (1991).
- [Fal97] R. Falster, M. Pagani, D. Gambaro, M. Cornara, M. Olmo, G. Ferrero, P. Pichler, M. Jacob, *Solid State Phenom.*, **57-58**, 129 (1997).
- [Fal97a] R. Falster, M. Cornara, D. Gambaro, M. Olmo and M. Pagani, *Solid State Phenom.*, **57-58**, 123 (1997).
- [Fre06] T. A. Frewen, T. Sinno, *Appl. Phys. Lett.*, **89**, 191903 (2006).
- [Fu07] L. Fu, D. Yang, X. Ma, H. Jiang, D. Que, *Semicond. Sci. Technol.*, **22**, 1302 (2007).
- [Fuj97] H. Fujimori, *J. Electrochem. Soc.*, **144**, 3180 (1997).
- [Gas80] J. Gass, H. H. Müller, H. Stüssi, and S. Schweitzer, *J. Appl. Phys.*, **51**, 2030 (1980).
- [Gaw84] P. Gaworzewski, E. Hild, F. G. Kirscht, and L. Vacsernyes, *Phys. Status Sol. A*, **85**, 133 (1984).
- [Goe60] A. Goetzberger, W. Shockley, *J. Appl. Phys.*, **31**, 1821 (1960).
- [Gös82] U. Gösele and T. Y. Tan, *Appl. Phys. A*, **28**, 79 (1982).
- [Gra85] K. Graff, H. A. Heffner, H. Pieper, *Mater. Res. Soc. Proc.*, **36**, 19 (1985).
- [Gra95] K. Graff, *Metal Impurities in Silicon-Device Fabrication* in: Springer Ser. Mater. Sci., 24 (1995).
- [Gue00] Y.M. Guerguiev, R. Kögler, A. Peeva, A. Mücklich, D. Panknin, R.A. Yankov, W. Skorupa, *J. Appl. Phys.*, **88**, 5645 (2000).
- [Hal92] T. Hallberg and J. L. Lindström, *J. Appl. Phys.*, **72**, 5130 (1992).
- [Hal99] T. Hallberg, L. I. Murin, J. L. Lindström, V. P. Markevich, *J. Appl. Phys.*, **84**, 2466 (1999).
- [Ham58] F. S. Ham, *J. Phys. Chem. Solids*, **6**, 335 (1957).
- [Har11] B. R. Hart, S. S. Dimov, and R. St. C. Smart, *Surf. Interface Anal.*, **43**, 449–451(2011).

- [Has92] M. Hasebe, J. W. Corbett, K. Kawakami, *Mater. Sci. Forum*, **83-87**, 1475 (1992).
- [Höl02] R. Hölzl, M. Blietz, L. Fabry, R. Schmolke, Proc. Semiconductor Silicon 2002, ed. by H. R. Huff, L. Fabry, S. Kishino, in: *Electrochem. Soc. Proc.*, 2002-2, 608 (2002).
- [Hoz02] K. Hozawa, S. Isomae, J. Yugami, *Jpn. J. Appl. Phys.*, **41**, 5887 (2002).
- [Hro57] H. J. Hrostowski and R. H. Kaiser, *Phys. Rev.*, **107**, 966 (1957).
- [Hro91] H. J. Hrostowski and R. H. Kaiser, *J. Phys. Chem. Solids*, **9**, 214 (1959).
- [Hu80] S. M. Hu, *J. Appl. Phys.*, **51**, 5945 (1980).
- [Hu86] S. M. Hu, *Materials Research Society Symp.* **59**, 249 (1986).
- [Hu86a] S. M. Hu, *Appl. Phys. Lett.*, **48**, 115 (1986).
- [Ino87] N. Inoue, K. Watanabe, K. Wada, and J. Osaka, *J. Cryst. Growth*, **84**, 21 (1987).
- [Iso02] S. Isomae, H. Ishida, T. Itoga, K. Hozawa, *J. Electrochem. Soc.*, **194**, G343 (2002).
- [Ist00] A. A. Istratov, C. Flink, S. Balasubramanian, E. R. Weber, H. Hieslmair, S. A. McHugo, H. Hedemann, M. Seibt, W. Schröter, in High Purity Silicon VI, C. Claeys, P. Rai-Choudhury, M. Watanabe, P. Stallhofer, and H. J. Dawson, Editors, PV 2000-17, p. 258, The Electrochemical Society Proceedings Series, Pennington, NJ (2000).
- [Ist02] A. A. Istratov, R. Sachdeva, C. Flink, S. Balasubramanian, E. R. Weber, *Solid State Phenom.*, 82-84, 323 (2002).
- [Ist98] A. A. Istratov, C. Flink, H. Hieslmair, E. R. Weber, T. Heiser, *Phys. Rev. Lett.*, **81**, 1243 (1998).
- [Itoh85] Y. Itoh and T. Nozaki, *Jpn. J. Appl. Phys.*, **24**, 279 (1985).
- [ITR11] ITRS, <http://public.itrs.net/>.
- [Kai56] W. Kaiser, P. H. Keck, and C. F. Lange, *Phys. Rev.*, **101**, 1264 (1956).
- [Kai57] W. Kaiser, *Phys. Rev.*, **105**, 1751 (1957).
- [Kan89] J. S. Kang, D. K. Schroder, *J. Appl. Phys.*, **65**, 2974 (1989).
- [Kas00] D. Kashchiev, *Nucleation: Basic Theory with Applications* (Butterworth-Heinemann, Oxford, 2000).
- [Kel03] K. F. Kelton, *Phil. Trans. R. Soc. Lond. A*, **361**, 429-446 (2003).
- [Kel99] K. F. Kelton, R. Falster, D. Gambaro, M. Olmo, M. Cornara, P. F. Wei, *J. Appl. Phys.*, **85**, 8097 (1999).

- [Kis00] G. Kissinger, J. Vanhellemont, G. Obermeier, J. Esfandyari, *Mater. Sci. Eng. B*, **73**, 106 (2000).
- [Kis06] G. Kissinger and J. Dabrowski, *ECS Transactions*, **3**, 97 (2006).
- [Kis06a] G. Kissinger, T. Müller, A. Sattler, W. Häckl, P. Krottenthalerc, T. Grabolla, H. Richter, W. von Ammon, *Mat. Sci. Process.*, **9**, 236 (2006).
- [Kis07] G. Kissinger, J. Dabrowski, A. Sattler, C. Seuring, T. Müller, H. Richter, W. von Ammon, *J. Electrochem. Soc.*, **154**, H454 (2007).
- [Kis08] G. Kissinger, D. Kot, J. Dabrowski, V. Akhmetov, A. Sattler, and W. von Ammon, *ECS Transactions*, **16** (6), 97 (2008).
- [Kis08a] G. Kissinger and J. Dabrowski, *J. Electrochem. Soc.*, **155** (6), H448-H454 (2008).
- [Kis08b] G. Kissinger, J. Dabrowski, A. Sattler, T. Müller, and W. von Ammon, *Sol. St. Phenom.*, **131-133**, 293 (2008).
- [Kis09] G. Kissinger, D. Kot, V. Akhmetov, A. Sattler, T. Müller, W. von Ammon, *ECS Trans.*, **18**, 995 (2009)
- [Kis10] G. Kissinger, D. Kot, W. Häckl, *ECS Transactions*, **33(11)**, 113 (2010).
- [Kis10a] G. Kissinger, D. Kot, J. Dabrowski, W. Häckl, V.D. Akhmetov, A. Sattler, Proc. 6th Forum of the Science and Technology of Si Materials, 36 (2010).
- [Kis11] G. Kissinger, J. Dabrowski, D. Kot, V.D. Akhmetov, A. Sattler, W. von Ammon, *J. Electrochem. Soc.*, **158**, H343 (2011).
- [Kis96] G. Kissinger, J. Vanhellemont, E. Simoen, C. Claeys, H. Richter, *Mater. Sci. Eng. B*, **36**, 225 (1996).
- [Kol10] B. O. Kolbesen, J. Mähliß, D. Possner, *Phys. Stat. Sol. B*, **208**, 584 (2010).
- [Kot08] D. Kot, G. Kissinger, W. Häckl, A. Sattler, W. von Ammon, *ECS Trans.*, **16(6)**, 207 (2008).
- [Kot09] D. Kot, G. Kissinger, A. Sattler, W. von Ammon, *ECS Trans.*, **25(3)**, 67 (2009).
- [Kot12] D. Kot, G. Kissinger, M.A. Schubert, T. Müller, A. Sattler, *Materials Science Forum*, Vol. **725**, 239 (2012).
- [Kre05] D. Krekar, M. Fuchs, R. Kögler, H. Hutter, *Anal. Bioanal. Chem.*, **381**, 1526 (2005).
- [Lee04] G. S. Lee, J. G. Park, *J. Ceram. Process. Res.*, **5** (3), 251 (2004).
- [Lee85] S. T. Lee and D. Nichols, *Appl. Phys. Lett.*, **47**, 1001 (1985).

- [Lee86] S. T. Lee and D. Nichols, in *Oxygen, Carbon, Hydrogen, and Nitrogen in Silicon*, edited by J. C. Mikkelsen, Jr., S. J. Pearton, J. W. Corbett, and S. J. Pennycook (Materials Research Society, Princeton, NJ, 1986), p. 31.
- [Lee88] S. T. Lee, P. Fellingner, S. Chen, *J. Appl. Phys.*, **63**, 1924 (1988).
- [Lin94] W. Lin, *Semiconductors and Semimetals*, **42**, 9 (1994).
- [Liv84] P. M. Livingston, S. Messoloras, R. C. Newman, B. C. Pike, R. J. Stewart, N. J. Binns, W. P. Brown, and J. G. Wilkes, *J. Phys. C: Solid State Phys.*, **17**, 6253 (1984).
- [Log59] R. A. Logan and A. J. Peters, *J. Appl. Phys.*, **30**, 1627 (1959).
- [Lu09] J. Lu, X. Yu, Y. Park, and G. Rozgonyi, *J. Appl. Phys.*, **105**, 073712 (2009).
- [Ma05] Q. Ma, Y. Li, S. Yang, H. Liu, Q. Hao, *Mater. Sci. Eng. B*, **122**, 218 (2005).
- [Mad96] C. Maddalon-Vinante, E. Ehret, and D. Barbier, *J. Appl. Phys.*, **79**, 2707 (1996).
- [Mäh09] J. Mähliß, A. Abbadie, B. O. Kolbesen, *Mater. Sci. Eng. B*, **159-160**, 309 (2009).
- [Mik82] J. C. Mikkelsen, *Appl. Phys. Lett.*, **40**, 336 (1982).
- [Mik86] J. C. Mikkelsen, Jr., in *Oxygen, Carbon, Hydrogen, and Nitrogen in Silicon*, edited by I. C. Mikkelsen, Jr., S. J. Pearton, J. W. Corbett, and S. J. Pennycook (Materials Research Society, Princeton, NJ, 1986), p. 19.
- [Mis06] A. Misiuk, C. A. Londos, J. Bak-Misiuk, D. Yang, W. Yang, M. Prujarczyk, *Nucl. Instr. and Meth. Phys. Res. B*, **253**, 205 (2006).
- [Mye00] S. M. Myers, M. Seibt, W. Schröter, *J. Appl. Phys.*, **88**, 3795 (2000).
- [Mye96] S. M. Myers, D. M. Follstaedt, *J. Appl. Phys.*, **79**, 1337 (1996).
- [Nak00] K. Nakai, M. Hasebe, K. Ohta, W. Ohashi, *J. Crystal Growth*, **210**, 20 (2000).
- [Nes71] E. Nes and J. Washburn, *J. Appl. Phys.*, **42**, 3562 (1971).
- [Nes72] E. Nes and G. Lunde, *J. Appl. Phys.*, **43**, 1835 (1972).
- [Nes73] E. Nes and J. Washburn, *J. Appl. Phys.*, **44**, 3682 (1973).
- [New00] R. C. Newman, *J. Phys. Condens. Matter.*, **12**, R335 (2000).
- [New83] R. C. Newman, A. S. Oates, and F. M. Livingston, *J. Phys. C*, **16**, L667 (1983).
- [New85] R. C. Newman, *J. Phys. C*, **18**, L967 (1985).

- [New90] M. R. C. Newman, A. R. Brown, R. Murray, A. Tipping, and J. H. Tucker, in *Semiconductor Silicon 1990*, edited by H. R. Huff, K. G. Barraclough, and J. Chikawa (The Electrochemical Society, Pennington, NJ, 1990), p. 734.
- [New94] R. C. Newman and R. Jones, *Semiconductors and Semimetals*, **42**, 289 (1994).
- [Oh00] H. J. Oh, J. H. Wang, K-M. Kim, H-D. Yoo, in *High Purity Silicon VI*, C. Claeys, P. Rai-Choudhury, M. Watanabe, P. Stallhofer, and H. J. Dawson, Editors, PV 2000-17, p. 44, The Electrochemical Society Proceedings Series, Pennington, NJ (2000).
- [Our84] A. Ourmazd, W. Schröter, *Appl. Phys. Lett.*, **30**, 781 (1984).
- [Pag97] M. Pagani, R. Falster, G. R. Fisher, G. C. Ferrero, M. Olmo, *Appl. Phys. Lett.*, **70** (12), 1572 (1997).
- [Par01] J. Park and K. Kwack, *J. Korean Phys. Soc.*, **38**, 356 (2001).
- [Par06] J. G. Park, G. S. Lee, J-S. Lee, K. Kurita, H. Furuya, *Mater. Sci. Eng. B*, **134**, 249 (2006).
- [Pee00] A. Peeva, R. Kögler, G. Brauer, P. Werner, W. Skorupa, *Mater. Sci. Semicond. Processing*, **3**, 297 (2000).
- [Pel10] M. Pellowska, D. Possner, D. Kot, G. Kissinger, B. O. Kolbesen, *Sol. St. Phenom.*, **156-158**, 443 (2010).
- [Pér01] I. Périhaud, E. Yakimov, S. Martinuzzi, C. Dubois, *J. Appl. Phys.*, **90**, 2806 (2001).
- [Pon89] F. A. Ponce, S. Hahn, *Mater. Sci. Eng. B*, **4**, 11 (1989).
- [Ram98] M. Ramamootrthy and S. T. Pantelides, *Solid State Commun.*, **106**, 243 (1998).
- [Rud09] P. Rudolph and K. Kakimoto, *MRS Bulletin*, **34**, 251 (2009).
- [Sak97] K. Sakai, T. Ogawa, *Meas. Sci. Technol.*, **8**, 1090 (1997).
- [San07] K. Sangwal, *Additives and Crystallization Processes : From Fundamentals to Applications* (Chichester 2007), p. 26.
- [Sas00] A. Sassella, A. Borghesi, G. Borionetti, P. Geranzami, *Mater. Sci. Eng. B*, **75**, 224 (2000).
- [Sas99] A. Sassella, A. Borghesi, P. Garanzani, G. Borionetti, *Appl. Phys. Lett.*, **75**, 1131 (1999).
- [Sch02] W. Schröter, V. Kveder, M. Seibt, A. Sattler, E. Spiecker, *Sol. Energy Mater. Sol. Cells*, **72**, 299 (2002).

- [Sch91] W. Schröter, M. Seibt, D. Gilles: High-temperature properties of 3d transition elements in silicon in *Electronic Structure and Properties of Semiconductors*, ed. by W. Schröter (VHC, Weinheim 1991) p. 539.
- [Sch99] D. C. Schmidt, B. G. Svensson, J. F. Barbot, C. Blanchard, *J. Appl. Phys.*, **75**, 364 (1999).
- [Sea02] M. Seacrist, M. Stinson, J. Libbert, R. Standley, and J. Bins, in *Semiconductor Silicon/2002*, H. R. Huff, L. Fabry and S. Kishino, Editors, PV 2002-2, p. 638, The Electrochemical Proceedings Series, Pennington, NJ (2002).
- [Sec72] F. Secco d'Aragona, *J. Electrochem. Soc.*, **119**, 948 (1972).
- [Sei09] M. Seibt, R. Khalil, V. Kveder, W. Schröter, *Appl. Phys. A*, **96**, 235 (2009).
- [Sei99] M. Seibt, H. Hedemann, A.A. Istratov, F. Riedel, A. Sattler, W. Schröter, *Phys. Status Solidi A*, **171**, 301 (1999).
- [Sha03] M. B. Shabani, Y. Shiina, F. G. Kirscht, Y. Shimanuki, *Mat. Sci. Eng. B*, **102**, 313 (2003).
- [Sha96] M. B. Shabani, T. Yoshimi, H. Abe, *J. Electrochem. Soc.*, **143**, 2025 (1996).
- [She94] B. Shen, T. Sekiguchi, J. Jablonski, K. Sumino, *J. Appl. Phys.*, **76**, 4540 (1994).
- [Shi01] Y. Shiraishi, K. Takano, J. Matsubara, T. Iida, N. Takase, N. Machida, M. Kuramoto, H. Yamagishi, *J. Cryst. Growth*, **229**, 17 (2001).
- [Shi89] F. Shimura, *Semiconductor Silicon Crystal Technology*, Academic Press, Inc., San Diego, 1989.
- [Shi94] F. Shimura, *Semiconductors and Semimetals*, **42**, 577 (1994).
- [Shk92] B. L. Shklyar, Yu. V. Trubitsyn and A. M. Zasyad'vovk, *J. Appl. Spectrosc.*, **57**, 636 (1992).
- [Sin97] T. Sinno, R. Brown, W. von Ammon, and E. Dornberger, *Appl. Phys. Lett.*, **70**, 2250 (1997).
- [Sir61] E. Sirtl and Annemarie Adler, *Z. Metallkunde*, **52**, 529 (1961).
- [Sko95] W. Skorupa, N. Hatzopoulos, and R. A. Yankov, *Appl. Phys. Lett.*, **67**, 2992 (1995).
- [Sta83] M. Stavola, J. R. Patel, L. C. Kimerling, and P. E. Freeland, *Appl. Phys. Lett.*, **42**, 73 (1983).
- [Sue00] K. Sueoka, M. Akatsuka, T. Ono, E. Asayama, Y. Koike, N. Adachi, S. Sadamitsu, and H. Katahama, in *High Purity Silicon VI*, C. L. Claeys, P. Rai-

- Choudhury, M. Watanabe, P. Stallhofer and H. J. Dawson, Editors, PV 2000-17, p. 164, The Electrochemical Proceedings Series, Pennington, NJ (2000).
- [Sue03] K. Sueoka, M. Akatsuka, M. Okui, and H. Katahama, *J. Electrochem. Soc.*, **150**, G469 (2003).
- [Sue05] K. Sueoka, *J. Electrochem. Soc.*, **152** (10), G731-G735 (2005).
- [Sue06] K. Sueoka, S. Ohara, S. Shiba, S. Fukatani, *ECS Transactions*, **2**, 261 (2006).
- [Sue93] K. Sueoka, N. Ikeda, T. Yamamoto, and S. Kobayashi, *J. Appl. Phys.*, **74**, 5437 (1993).
- [Sum99] K. Sumio, *Phys. Stat. Sol.*, **171**, 111 (1999).
- [Tak73] Y. Takano and M. Maki, in *Semiconductor Silicon 1973*, edited by H. R. Huff and R. R. Burgers (The Electrochemical Society, Princeton, NJ, 1973), p. 469.
- [Tak98] H. Takeno, Y. Hayamizu, and K. Miki, *J. Appl. Phys.*, **84**, 3113 (1998).
- [Tan94] T. Y. Tan, W. J. Taylor, *Semiconductors and Semimetals*, **42**, 353 (1994).
- [Tay92] W. J. Taylor, U. Gösele, and T. Y. Tan, *J. Appl. Phys.*, **72**, 2192 (1992).
- [Til86] W. A. Tiller, S. Hahn, F. A. Ponce, *J. Appl. Phys.*, **59**, 3255 (1986).
- [Tol03] V. P. Tolstoy, I. V. Chernyshova, V. A. Skryshevsky, *Handbook of infrared spectroscopy of ultra thin films*, (Hoboken, New Jersey 2003), p 60.
- [Tom99] J. Tomeczek, *Termodynamika*, Wydawnictwo Politechniki Slaskiej, 255 (1999).
- [Tsu04] H. Tsuya, *Jpn. J. Appl. Phys.*, **43**, 4055 (2004).
- [Van05] J. Vanhellefont, O. De Gryse, P. Clauws, *Appl. Phys. Lett.*, **86**, 221903 (2005).
- [Van87/92] J. Vanhellefont, C. Claeys, *J. Appl. Phys.*, **62**, 3960 (1987); J. Vanhellefont and C. Claeys, *ibid.* **71**, 1073 (1992)..
- [Van95] J. Vanhellefont, *J. Appl. Phys.*, **78**, 4297 (1995).
- [Van96] J. Vanhellefont, *Appl. Phys. Lett.*, **68**, 3413 (1996).
- [Veh07] H. Vehkamäki, A. Määttänen, A. Lauri, I. Napari, and M. Kulmala, *Atoms. Chem. Phys.*, **7**, 309 (2007).
- [Von99] W. von Ammon, *Properties of Crystalline Silicon* (EMIS Datareviews Series No. 20) ed R. Hull (New York: INSPEC IEE), p. 39 (1999).
- [Vor01] V. V. Voronkov and R. Falster, *J. Appl. Phys.*, **89**, 5969 (2001).
- [Vor02] V. V. Voronkov, R. Falster, *J. Appl. Phys.*, **91**, 5802 (2002).
- [Vor82] V. V. Voronkov, *J. Crystal Growth*, **59**, 625 (1982).

- [Vor98] V. V. Voronkov, F. Falster, *J. Crystal Growth*, **194**, 76 (1998).
- [Wag91] P. Wagner, *Appl. Phys. A*, **53**, 20 (1991).
- [Wan02] Z. Wang and R. A. Brown, ECS Proceedings, **20**, 49 (2002).
- [Wan04] H. Wang, X. Ma, J. Xu, X. Yu, *Semicond. Sci. Technol.*, **19**, 715 (2004).
- [Wat82] G. D. Watkins, J. W. Corbett, and R. S. McDonald, *J. Appl. Phys.*, **53**, 7097 (1982).
- [Web02] E. R. Weber, Impurity Precipitation, Dissolution, Gettering, and Passivation in PV Silicon, Final Technical Report, February 2002, NREL/SR-520-31528.
- [Web83] E. R. Weber, *Appl Phys. A*, **30**, 1 (1983).
- [Wij91] W. Wijaranakula, *Appl. Phys. Lett.*, **59**, 1185 (1991).
- [Won88] H. Wong, N. W. Cheung, P. K. Chu, J. Liu, J. W. Mayer, *Appl. Phys. Lett.*, **52**, 1023 (1988).
- [Woo73] D. P. Woodruff, *The Solid-Liquid Interface*. Cambridge University Press 1973 p.77.
- [Wri77] Margarete Wright Jenkins, *J. Electrochem. Soc.*, **124** (1977) 757.
- [Yam90] H. Yamada-Kaneta, C. Kaneta, T. Ogawa, *Phys. Rev. B*, **42**, 9650 (1990).
- [Yon00] M. Yonemura, K. Sueoka, K. Kamei, *J. Appl. Phys.*, **88**, 503 (2000).
- [Yu09] X. Yu, J. Lu, K. Youssef, G. Rozgonyi, *Appl. Phys. Lett.*, **94**, 221909 (2009).
- [Zio11] B. Ziolkowski, [http://www.immt.pwr.wroc.pl/~ziolek/Pliki/TW8 przemiany fazowe 29.03.2011.pdf](http://www.immt.pwr.wroc.pl/~ziolek/Pliki/TW8_przemiany_fazowe_29.03.2011.pdf)